Sensors for seismic isolation in gravitational wave detectors

Author:
Amit Singh Ubhi

Supervisor:
Dr. Denis Martynov

A thesis submitted to the University of Birmingham for the degree of
Doctor of Philosophy

School of Physics & Astronomy
Institute for Gravitational Wave Astronomy
College of Engineering and Physical Sciences
University of Birmingham

June 15, 2022

UNIVERSITY OF
BIRMINGHAM

University of Birmingham Research Archive

e-theses repository

This unpublished thesis/dissertation is copyright of the author and/or third parties. The intellectual property rights of the author or third parties in respect of this work are as defined by The Copyright Designs and Patents Act 1988 or as modified by any successor legislation.

Any use made of information contained in this thesis/dissertation must be in accordance with that legislation and must be properly acknowledged. Further distribution or reproduction in any format is prohibited without the permission of the copyright holder.

Declaration of Authorship

I, Amit Singh UBHI, declare that this thesis titled, “Sensors for seismic isolation in gravitational wave detectors” and the work presented in it are my own. I confirm that:

- This work was done wholly while in candidature for a research degree at this University.
- Where any part of this thesis has previously been submitted for a degree or any other qualification at this University or any other institution, this has been clearly stated.
- Where I have consulted the published work of others, this is always clearly attributed.
- Where I have quoted from the work of others, the source is always given. With the exception of such quotations, this thesis is entirely my own work.
- I have acknowledged all main sources of help.
- Where the thesis is based on work done by myself jointly with others, I have made clear exactly what was done by others and what I have contributed myself.

Signed:

Date: June 15, 2022

UNIVERSITY OF BIRMINGHAM

Abstract

College of Engineering and Physical Sciences
School of Physics & Astronomy

Doctor of Philosophy

Sensors for seismic isolation in gravitational wave detectors

by Amit Singh UBHI

A new window of astronomy was opened via the direct detection of gravitational waves in 2015. Since then, dozens of detections from compact binary sources have been confirmed via the Laser Interferometer Gravitational-Wave Observatory (LIGO) and Virgo observatories; both having peak sensitivities at approximately 100 Hz. Improvement of the low frequency sensitivity of detectors would enable detections of more massive binaries, and provide insight into the evolution of these systems.

Operation of these detectors require sophisticated seismic isolation strategies. Despite the variations in their isolation schemes, passive filtering of the motion is achieved via the use of multistage suspensions of the core optics. In the case of LIGO, the suspension chains hang from state of the art passive-active platforms, requiring inertial sensing to stabilise their motion. The control scheme required degrades the sensitivity to gravitational waves below 30 Hz.

In this thesis, the principles of detection for ground based observatories are discussed, focusing on a new novel inertial sensor for improving the sensing scheme of the isolated platforms. Analysis of the design and dynamics of this device are described, and predictions of its sensitivity are determined.

A derivative of the seismometer was constructed to test the necessary data handling required for successful operation of the device before further investigations of the original design were pursued. The key results of this study were that the device had similar translational sensitivity to that of LIGO's commercial seismometers such as the T240. Control of a LIGO-inspired six-axis platform was achieved using the original inertial sensor, obtaining over an order of magnitude improved isolation for 5 of 6 degrees of freedom at 1 Hz. Further work was performed on a separate optical shadow sensor to assess their implementation in cryogenic upgrades to the LIGO observatories. Operation of the device below 123 K resulted in a 25% improvement of its shot noise sensitivity, from $6 \times 10^{-11}\mathrm{m}/\sqrt{\mathrm{Hz}}$ to $4.5 \times 10^{-11}\mathrm{m}/\sqrt{\mathrm{Hz}}$.

The findings of these investigations are presented and conclusions are made on the viability of these sensors for use in future upgrades.

Acknowledgements

My sincere thanks to my supervisor, Dr. Denis Martynov, for showing me what true passion and dedication to work is, and for guiding me throughout our time together.

Prof. Giles Hammond and Prof. Kostas Nikolopoulos, for the thorough analysis of my thesis, and for making my viva an enjoyable experience.

Prof. Alberto Vecchio, for his welcoming nature no matter how busy he is.

Mr. David Stops, for our continuous conversations, emails, and most importantly, his patience.

Sam and Chiara, for discussions on work.

Farrah, for making the office feel a little more like home.

Jiri, thank you for our constant conversations which always sparked my curiosity.

And Riccardo, for the food, company, and for being my confidant.

To Matt and Janki, friends like family.

To Hamzah and Fatima, friends who came out the blue.

To Hardev, Boora, and Kam, friends, brothers, men who keep me grounded.

To my brother, for believing I can always achieve more.

To my parents, for supporting me, always.

To the countless family and friends, past and present, who have shaped me into who I am.

Finally, to my wife, for the motivation and encouragement, for pushing me when I didn’t want to be. For all of the things you do, thank you.

Contents

Declaration of Authorship **iii**

Abstract **v**

Acknowledgements **vii**

1 Introduction **1**

1.1 Gravitational waves (GWs) and their sources 1

1.1.1 Binary systems 5

1.1.2 Bursts 6

1.1.3 Continuous waves 6

1.1.4 Stochastic Background 7

1.2 Detection Method 7

1.2.1 Future Upgrades and Detectors 9

1.3 Noise Sources 11

1.3.1 Quantum Noise 12

1.3.2 Thermal Noise 13

Suspensions 13

Coatings 14

1.3.3 Seismic Noise 15

1.4 Thesis Overview 15

2 Seismic Noise, Sensing, and Isolation **17**

2.1 Seismic Noise 17

2.2 Inertial Sensors 19

2.2.1 Tilt Coupling 24

2.2.2 Sensor Responses 25

2.3 Passive Isolation 26

2.4 Active Isolation 29

2.5 Control Theory 30

2.5.1 Feedback and Stability 31

2.5.2 Feedforward 33

2.5.3 Sensor Blending 34

2.6 Summary 36

3 The six degree of freedom (6D) inertial sensor **39**

3.1 Background 39

3.2 Design Parameters 42

3.3 Coordinate system 45

3.4 The Lagrangian Model 47

3.4.1 Full Lagrangian 49

3.4.2 Vertical Degree of Freedom 52

3.4.3 Torsional Degree of Freedom 53

3.4.4 The Coupled Degrees of Freedom 55

3.4.5 Model Predictions 64

3.5 *Internal Seismic Isolation* (ISI) model 69

3.6 Summary 73

4 The Compact 6D sensor **75**

4.1 Abstract . . . 75

4.2 Introduction . . . 76

4.3 Metallic prototype . . . 78

  4.3.1 Mechanical design . . . 78

  4.3.2 Plastic deformations . . . 80

  4.3.3 Optical readout . . . 81

  4.3.4 Mechanical cross-couplings . . . 82

  4.3.5 Sensitivity . . . 84

4.4 Fused silica seismometer . . . 87

  4.4.1 Low frequency drifts . . . 89

  4.4.2 Projected motion of the aLIGO platforms . . . 90

  4.4.3 Projected motion of the aLIGO test masses . . . 93

4.5 Conclusion . . . 95

4.6 Fused Silica Mass . . . 95

5 Demonstration of the control system for the 6D seismometer **99**

5.1 Abstract . . . 99

5.2 Introduction . . . 100

5.3 Experimental design . . . 102

5.4 Control strategy . . . 105

  5.4.1 ISI stabilisation . . . 106

  5.4.2 Control problems from the ISI cross-couplings . . . 107

5.5 Performance . . . 109

5.6 Conclusions . . . 113

6 Cryogenic BOSEMs **115**

6.1 Abstract 115

6.2 Introduction 116

6.3 Finite-element analysis 117

6.4 Experimental results 120

6.5 Conclusion 126

7 Conclusions and Prospects **127**

7.1 Conclusions 127

List of Figures

1.1 Schematic of mass m orbiting mass M separated at a distance a. 4

1.2 An example of a Michelson interferometer. The highlighted magenta mirrors are the nominal position when no contraction or expansion has occurred. The ellipses are an example of a *gravitational wave* (GW) passing by, causing stretching and squeezing of the space-time perpendicular to the direction of travel. The highlighted mirrors illustrate an exaggerated view of the change in length of the interferometer's arms. This in turn would create interference in the antisymmetric port of the interferometer which is measured by the photodiode. 9

1.3 *Laser Interferometer Gravitational-Wave Observatory* (LIGO) noise curve produced using the GWINC software [1] with the standard parameters. 11

2.1 A mass on spring system with spring constant k, showing the input ground displacement x_g, the mass m, an external force acting on the mass F_{ext} and the position of the mass x_m. The distance Δx is the difference in position between the ground and the mass. 21

2.2 Transfer function responses for a mass on a spring. The blue curve describes the response of the mass to ground motion. The dashed black line at 20 Hz shows where the response of the mass motion changes from $1/f^2$ to $1/f$. Red indicates the reaction with respect to an external force . The yellow curve shows the differential position of the mass and ground due to input ground motion (the output of the inertial sensor). The purple curve shows the inverted response of the sensor which shows how the sensor response relates to the measured ground motion. The green curve is the inverted displacement response for a seismometer which uses a relative velocity readout scheme. 23

2.3 Schematic of tilt induced translation for a mass on a spring system. . . 24

2.4 **Left:** Responses of the various seismic sensors to velocity normalised to the short period seismometer at 100 Hz. **Right:** Acceleration response of the sensors according to the normalisation of the short period seismometer with respect to velocity. 26

2.5 A schematic of the BSC-ISI illustrating the instruments used to actively control the platform. The figure has been adapted from reference [2]. . 28

2.6 A block diagram of the signal flow from an input signal c to the measured output y through an actuator A, plant P, and sensor S. 31

2.7 A block diagram indicating the closed loop operation of a system. . . . 32

2.8 A block diagram illustrating the implementation of a feedforward signal to minimise the input noise n. 33

3.1 CAD drawings designed by Dr. Leonid Prokhorov, Dr. Samuel Cooper, and I, of the final *six degree of freedom inertial sensor* (6D) experimental setup inside the vacuum chamber. The highlighted magenta region focuses on the readout scheme using *Homodyne Quadrature Interferometers* (HoQIs) and the damping control with *Birmingham Optical Sensor and Electromagnetic Motors* (BOSEMs). 41

3.2 CAD drawing designed by Dr. Leonid Prokhorov of the 6D test mass. . 43

3.3 Visualisation of the coordinate system used throughout this thesis. . . . 45

3.4 A simplified schematic of the 6D system showing the main coordinates of interest for the coupled case discussed in Section 3.4.4. Note that the angles have been exaggerated for clarity. 49

3.5 Transfer functions for the Z degree of freedom showing the sensor response (yellow) and the response to an arbitrary force through the centre of mass (black). 54

3.6 Transfer functions for the RZ degree of freedom showing the sensor response (cyan) and the response to an arbitrary torque acting on the mass (black). Note that the magnitude at DC for the torque transfer function is large, meaning that the mass is more susceptible to motion from small inputs such as noise sources. 55

3.7 Plot of the tilt resonant frequency against the centre of mass offset, d. The left vertical line indicates the centre of mass position above the apparent bending point of the wire, creating an inverted pendulum resulting in a lower tilt resonance of 5 mHz. The vertical line on the right hand side shows the natural tilt resonance if no tuning is present. . . . 58

3.8 Transfer functions of the translational and tilt motion into the translational readout. For the input ground translation, we recover the inertial sensor response as expected. The tilt input tilt motion. β_s results in a flat transfer function in the readout scheme due to the geometry of the system, with a magnitude equal to the fibre length. 61
3.9 Transfer functions for the tilt degree of freedom. The tilt to tilt transfer function does not recover the inertial sensor response. The translational induced tilt motion is minimal due to the large separation of the translational and tilt resonances. 63
3.10 Block diagram showing the damping scheme for the test mass and the points of noise injection. Thermal noise injection has been omitted. . . 65
3.11 Readout and actuation noises. 67
3.12 Estimation of the noise sources for each degree of freedom after plant inversion. 68
3.13 Comparison of the tilt sensitivity of various rotation sensors [3, 4, 5, 6, 7, 8] and the 6D seismometer. 70
3.14 Comparison of the tilt decoupled translational sensitivity of commercial seismometers and the 6D sensor. 71
3.15 Illustration of the model used for determining the actuation matrix. . . 72

4.1 Picture of the isolated metallic prototype with an interferometric sensor. 78
4.2 Example of nonlinearities witnessed in the interferometric readout during the experiment. The nonlinearities are strongly suppressed by fitting the Lissajous figures of the compact interferometers with ellipses. The black curve shows the self noise of the sensor measured with stationary mirrors. 81

4.3 Transfer functions illustrating the coupling between the horizontal and vertical readouts due to the input platform translation x, and platform tilt θ. 83

4.4 Comparison of measured motion between the compact 6D seismometer and commercial L4C geophones. The translational readout of the seismometer (blue) is similar to the L4C signal (light blue) above 100 mHz. The vertical readout (red) measures tilt motion of the inertial mass up to 10 Hz and vertical motion of the platform above this frequency. The vertical L4C (orange) measures the same motion as the vertical HoQI above the bounce mode resonance at 25 Hz. 85

4.5 The figure shows the difference between the plant inversions of the translational and tilt modes with and without taking into account the X and RY cross-couplings. The orange curve shows the translation motion decoupled from the tilt mode such that the microseismic motion is removed. From the current sensitivity of the prototype, we see that the decoupled translational motion has the same noise floor as the tilt coupled T240 noise (green), and has better sensitivity than the L4C (dark green). 86

4.6 Model of the proposed fused silica compact 6D seismometer for the aLIGO active isolation platforms. 88

4.7 Estimated motion of the aLIGO platforms with the 6D seismometers (left). The right panel shows the comparison between the own noises of the 6D seismometers with the tilt eigenmode at 50 mHz and 100 mHz, and with the own noise of the T240 seismometers. 91

4.8 Comparison of the estimated pitch motion of the aLIGO test masses when the aLIGO platforms are stabilised with the proposed 6D seismometers with a tilt eigenmode of 50 mHz (left panel), 100 mHz (right panel) and the T240 seismometers. 93
4.9 Drawing provided to Heraeus for manufacturing the fused silica compact 6D test mass. 96
4.10 Photograph of one of the manufactured fused silica test masses. 98
4.11 Estimated noise floors of the fused silica compact 6D mass and the prototype discussed in Chapter 4. 98

5.1 (a) Image of the experimental setup and (b) an example of the measured signals with the corresponding noises. 105
5.2 Feedforward scheme for decoupling tilt translation from tilt. 107
5.3 Control scheme illustrating the actuation cross couplings and its effects. 108
5.4 Performance of the platform stabilisation using the 6D seismometer for simultaneous control of all six degrees of freedom. 112
5.5 Long term drift of the RZ degree of freedom. The stress relaxations in the fibre tend to stabilise after chamber venting and pump down leading to the mass returning to its nominal position. 113

6.1 Exploded view of the BOSEM setup. 117
6.2 Temperature (K) map of the BOSEM during the cool down simulation. This time step was chosen as it corresponded to maximum stresses in the BOSEM due to temperature variations. 119

6.3 Stress (MPa) map from temperature map in Fig. 6.2. The highlighted and zoomed section in magenta focuses on a cross section of the LED carrier and its components. 120

6.4 **Top left**: Photo of the BOSEM attached inside the vacuum chamber. Above the BOSEM is the thermal restrictor with power resistors connected. Thermocouples are attached to measure its temperature. **Top right**: Image of the BOSEM setup inside the chamber. The set up is encased in mylar to reduce radiative heating from the tank. **Bottom** The Schematic of the experimental set up. The BOSEM satellite amplifier output was converted to a single ended signal, AC coupled at 30 mHz, and high passed at 1 kHz using an SR560 low-noise preamplifier [9]- its output was measured using the Agilent 35670a dynamic signal analyser [10]. Multiple thermocouples were used to measure the BOSEM's temperature, and power resistors were used for temperature stabilisation. 122

6.5 Temperatures of BOSEM during cool down. the blue curve represents the thermal restrictor plate, and red and yellow were the power resistors. Purple was the side of the BOSEM housing. The PD outer casing is green, and the bottom of the BOSEM is in cyan. The inital cool down during the first 20 minutes sees the BOSEM change in temperature by over 100° C. 123

6.6 Comparison of the PD current during cool down. The 61.9 kΩ transimpedance amplifier did not cause saturation of the satellite amplifier output unlike the 121 kΩ transimpedance amplifier which saturated below 205 K. 123

6.7 Comparisons of the measurements made in vacuum and below 123 K. The high frequency shot noise improvements come from the increased PD current. The measurements contain low frequency peaks which occur due to the temperature stabilisation controller. The 61.9 kΩ transimpenance at room temperature coincided with the blue curve at room temperature. 124

List of Tables

3.1 A list of parameters and nominal values for the final idealised 6D design. 44

4.1 A list of parameters and nominal values 89
4.2 Properties of the fused silica test mass manufactured by Heraeus. . . . 97

5.1 A list of parameters and nominal values 104

"It is better to be a warrior in a garden,
than a gardener in a war."

Chapter 1

Introduction

Chapter 1 is a review chapter, and no original work is presented.

1.1 Gravitational waves (GWs) and their sources

GWs are ripples in space-time which result in the distance between freely falling objects to be altered. These waves were first predicted by Albert Einstein in his theory of general relativity in 1916 [11], and were first directly detected on the 14th September 2015 by LIGO [12]. However, this was not the first detection of GWs, they were indirectly observed by Hulse and Taylor when monitoring the orbital period of the Hulse–Taylor binary system (1993 Nobel Prize in Physics) [13]. The decreasing orbital period was indirect evidence that energy was emitted from the binary system in the form of GWs.

The first *binary black hole* (BBH) detection event, GW150914 [12] was the first observation of stellar mass black hole binary systems which previously had not been observed. Since that detection a number of BBH events have been confirmed with a host of further potential candidates [14, 15, 16]. In 2017, both the LIGO and Virgo detectors observed the inspiral of a *binary neutron star* (BNS) system dubbed

GW170817 [17], with individual masses of $1.46^{+0.12}_{-0.10}\,\mathrm{M}_\odot$ and $1.27^{+0.09}_{-0.09}\,\mathrm{M}_\odot$ which was the first multi-messenger event where a short gamma-ray burst, GRB170817A, followed the initial GW detection [18] by less than 2 seconds. The detection of the event from two different observation methods not only solidified the probability of the GW detection, but drastically improved the sky localisation of the source. A key astrophysical result from GW170817 was a constraint on the speed of GWs. Theory dictates that GWs propagate at the speed of light, and the observation in both GW detectors and in the electromagnetic spectrum improved the constraint between the difference of the speed of light and the speed of gravitational waves by approximately 14 orders of magnitude.

The merger frequency of events can be approximated as it is inversely proportional to the total mass of the binary system, therefore, the detection of intermediate mass black hole systems are less likely to be observed due to the low frequency detector noise as shown in Figure 1.3. Despite this, one observation of a BBH system, GW190521, has been made with a total mass of $150\,\mathrm{M}_\odot$ [19]. Detection of intermediate mass black holes enables us to understand the evolution of black holes from stellar masses up to supermassive black holes at the centres of galaxies.

Previous detections had all occurred from BBH and BNS systems, however in 2020, two *neutron star black hole* (NSBH) events (GW200105 and GW200115) were detected by the LIGO and Virgo observatories [20], the first of their kind. The consecutive detections of a NSBH event was not out of the ordinary in terms of the probability of detections. Observations of NSBH events enable us to investigate the origins of binary systems. Currently there are three predominant ideas of the formation of these systems: dense stellar environments such as young star clusters, galactic centres, and binary star systems.

The Universe is littered with binary systems that radiate GWs due to the energy losses from their orbits over time. We can use conservation laws to rule out particular causes for GW production within an isolated system located suitably far away. First we consider the conservation of mass within a closed system, resulting in no time variation of the monopole moment. Expanding to higher orders, the conservation of momentum prevents a time variation in the dipole moment, which is the distribution of mass within the system. The conservation of angular momentum also prevents the emission of GWs. Higher order moments are not linked with conservation laws, and hence the quadrupole moment of the system can be time variant, which is the dominant mechanism for GW production [21, 22]. A few simple examples of time variation in the quadrupole moment of a system are: asymmetric supernovae collapse, and spherically asymmetric rotating bodies [23, 24], as discussed in Section 1.1.3, and binary orbits, due to the lack of cylindrical symmetry about their orbital axis.

A simplified derivation of a binary system will be constructed to understand the properties of these waves. Consider a binary system containing two masses, M and m separated by distance a, where $M \gg m$ such that it appears as if body m orbits the stationary mass, M, as illustrated in Figure 1.1.

The lack of spherical symmetry of the system results in time variation of the quadrupole moment, Q, of the binary resulting in GW emission. For simplicity we assume the objects appear as point masses with M at the origin, hence the non-zero components of the quadrupole moment can be approximated to have amplitude

$$Q \sim ma^2. \tag{1.1}$$

The amplitude of the waves are represented by the dimensionless gravitational strain, h,

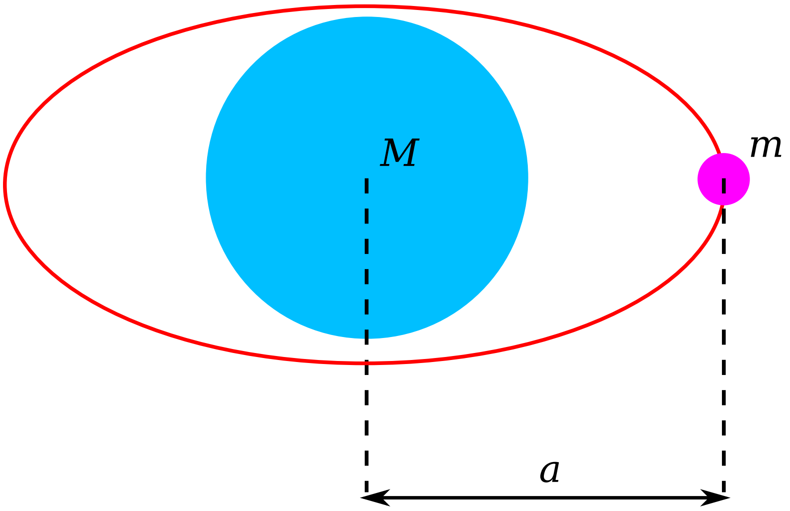

FIGURE 1.1: Schematic of mass m orbiting mass M separated at a distance a.

$$h = \frac{\Delta L}{L}, \tag{1.2}$$

where ΔL is the change in distance between two objects separated by a distance L.

The strain amplitude is inversely proportional to the distance from the source, r [25]. Using dimensional analysis, it can be concluded that the strain must include the gravitational constant G and the speed of light c such that

$$h \approx \frac{G}{c^4} \frac{\mathrm{d}^2 Q}{\mathrm{d}t^2} \frac{1}{r}. \tag{1.3}$$

To obtain an order of magnitude approximation, the time derivative can be simplified from $\frac{\mathrm{d}^2 Q}{\mathrm{d}t^2} \rightarrow Q/T^2$, where T is the orbital period of the system defined using Kepler's laws. The resultant strain amplitude becomes

$$h \sim \left(\frac{GM}{c^2}\right)\left(\frac{Gm}{c^2}\right)\frac{1}{a}\frac{1}{r}. \tag{1.4}$$

Current detections have occurred from sources which are at a distances of the order $r \sim 1$GPc [14, 15, 16] with the majority being BBH systems. The mass range of these black holes are approximately tens of solar masses. Consider two $50\,M_\odot$ black holes with a separation similar to their inner most stable orbit of $a_{\rm imso} = 6GM/c^2$, this would result in a strain amplitudes of $h \sim 10^{-21} - 10^{-22}$ at GW frequencies of $\sim 100\,$Hz. GWs produced at twice the orbital frequency are the dominant mode due to the symmetry within the system.

1.1.1 Binary systems

The example provided would represent a binary source where two massive objects orbit a common centre. As these masses orbit one another, rotational energy is lost in the form of gravitational waves. Loss of energy from the system causes the bodies to move closer to one another, increasing their orbital frequency until the point of merger [26]. The BBH example used showed that the GWs frequencies towards the end of life of the binary system can be approximated as $f \approx 12000/(M + m)$ where the masses M, m, are in terms of solar masses, $M_\odot$. For compact binaries with total mass $\sim 100M_\odot$, this would result in merger frequencies which are at the peak sensitivity of the LIGO detectors. Other binary sources are also present, such as BNSs, NSBHs that are candidates for detection.

1.1.2 Bursts

The most likely candidate for a burst signal is a supernova. Burst signals are spontaneous occurrences and hence, unpredictable. Detection of a burst signal would be a difficult feat for single detectors as the accompanying GW would be a momentary signal. Confirmation of a burst signal detection would require multiple simultaneous detections and potentially coincident multi-messenger observations. It is imperative that the collapse of a massive star during supernova is asymmetric, this is usually the case. [27, 28]

1.1.3 Continuous waves

As previously discussed, a single body must have asymmetry about its rotational axis in order to produce GWs. Pulsars - the remnant from a rotating massive star which has undergone supernova are such candidates. Initially a rotating massive star would have a mass above $8M_{\odot}$, and the remnant left behind after the supernova would be in the range of $(1.4-3)\,M_{\odot}$ [29]. More importantly the radius of the remnant would reduce by orders of magnitude as neutron stars are only $\sim 20\,\mathrm{km}$ in diameter. As a result, even if a fraction of the angular momentum is conserved after supernova, the star would rotate rapidly. Although being massive and compact, rotating neutron stars are not symmetric about their rotation axis and usually contain a "mountain" or bump. The origins of such bumps are not understood but could be a result of the original collapse of the star. Another suggestion is the rapidly rotating charges within the neutron star can generate a huge magnetic field which is usually misaligned from the rotation axis and create these "mountains". Due to this asymmetry, rotating neutron stars can emit GWs [30, 31].

1.1.4 Stochastic Background

In the electromagnetic spectrum we have observed the cosmic microwave background which is a relic of the earliest detectable radiation after the recombination epoch, where the hot dense plasma was now cool enough to photons to travel freely throughout the universe. After such a discovery, a stochastic background has been hypothesised. A number of sources could produce or contribute to the GW background varying from early events which occurred before the cosmic microwave background such as theorised primordial black holes - this would provide us with our earliest understanding of the universe. Another source could be the miniscule background radiation from all sources in the universe [32].

1.2 Detection Method

GW strain amplitudes are extremely small as previously discussed. For context, detectors would need to be able to detect length changes on the order of the thickness of a human hair on a distance scale from the Earth to our closest star, Proxima Centauri, which is 4.25 ly away. Therefore detectors must be extremely sensitive to minute length changes. In 1887, the Michelson-Morley experiment was conducted using the Michelson interferometer in an attempt to measure the "aether".

The device was an optical instrument used for detecting small displacement changes with respect to a reference (the other arm of the interferometer). The setup uses a beam of light which is split equally into two perpendicular arms. The light propagates the length of the arms and is reflected back by the end mirrors. At the beam splitter, the light recombines and the differential arm length can be induced from the measured signal [33]. For a more detailed understanding of the workings of interferometers, refer to reference [34]. An example of a Michelson interferometer is depicted in Figure 1.2.

The basis of gravitational wave detectors is the Michelson interferometer, however, some adaptions have been made to further increase its sensitivity to displacement changes. The arms of gravitational wave detectors have been converted into Fabry-Perot arm cavities which increases the effective laser power within the arms. The Fabry-Perot cavity also recycles the physical length of the arms, resulting in the apparent length of the arms to be multiplied by the finesse of the cavities. As a result the phase shift difference between the arms to accumulate, amplifying the signal to be measured due to the increased light storage time. For the 4 km long arms of the LIGO detectors, the round trip time is given by $t_{RT} = 2L/c \approx 27\,\mu\text{s}$, where L is the arm length, and c is the speed of light. The light storage time is defined as $t_{stor} = t_{RT}\mathcal{F}/2\pi$, where $\mathcal{F}$ is the finesse of the cavity. Further increasing the arm power has been accomplished via a power recycling cavity at the symmetric port of the detector. A signal recycling cavity at the antisymmetric port enables frequency shaping of the detectors response to increase its sensitivity [35]. For LIGO, the resultant arm cavity finesse is improved due to power and signal recycling cavities, such that $\mathcal{F} = 41000$, therefore $t_{stor} \approx 0.18\,\text{s}$. A number of further auxiliary optics are also used and additional upgrades are continually investigated worldwide. For the current LIGO detectors the detection band sweeps a frequency range from 10 Hz-10 kHz with its most sensitive region near the cavity pole at $\sim 100\,\text{Hz}$ [36].

The propagation of GWs results in expansion and contraction of space-time perpendicular to the waves direction of travel. As a GW passes the detector, it causes the arm lengths to vary differentially as indicated in Figure 1.2, causing a change in the propagation time within the arm. The arms of the detectors are tuned to be of equal length $L = L_x = L_y$, as the wave passes, the measured arm length difference becomes

$$\Delta L(t) = \Delta L_x - \Delta L_y = Lh(t), \tag{1.5}$$

where $h(t)$ is the time dependent gravitational strain.

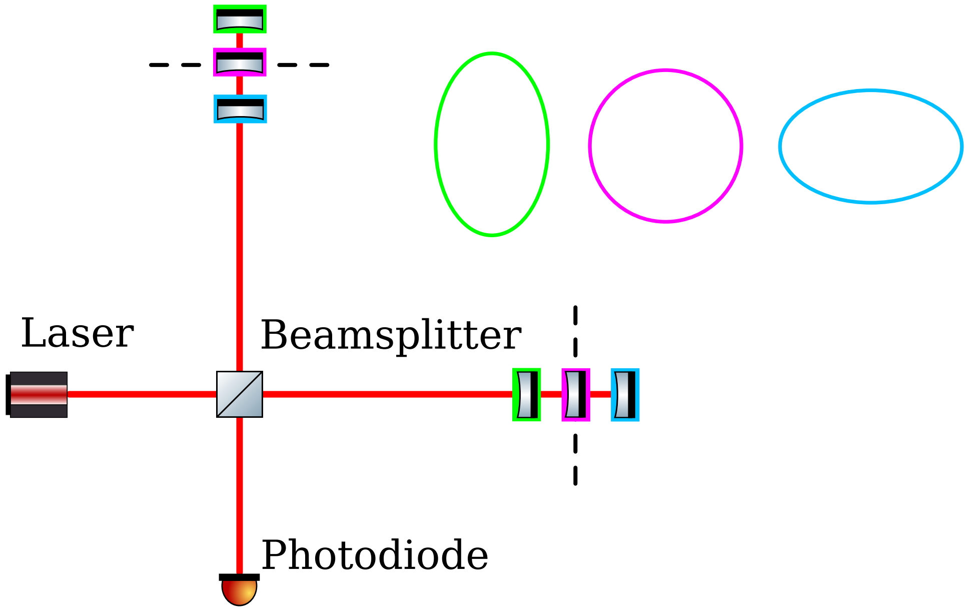

Figure 1.2: An example of a Michelson interferometer. The highlighted magenta mirrors are the nominal position when no contraction or expansion has occurred. The ellipses are an example of a GW passing by, causing stretching and squeezing of the space-time perpendicular to the direction of travel. The highlighted mirrors illustrate an exaggerated view of the change in length of the interferometer's arms. This in turn would create interference in the antisymmetric port of the interferometer which is measured by the photodiode.

1.2.1 Future Upgrades and Detectors

Future detectors such as Einstein Telescope and Cosmic Explorer aim to improve low frequency detection by increasing the arm lengths to 10 km and 40 km respectively.

The increased length also increases the measured length changes in the arms as shown in Equation (1.5), amplifying the GW signal.

LIGO is currently in its *Advanced LIGO* (aLIGO) stage and has been observing since 2015. Updates to the detector have been commissioned over time for its next upgrade known as A+, which is expected to be operational during 2024. Beyond this the next major upgrade is known as A#, which focuses on low frequency detection (which is the focus of this thesis) and is expected to happen in the late 2020s. Cryogenic updates to the detector are planned for the LIGO Voyager update, which is targeted in the 2030s. This looks to use more massive test mass mirrors made of silicon, operating at 123 K using longer wavelength lasers.

Two terrestrial future detectors are also planned to be commissioned. Cosmic Explorer is a LIGO style two arm detector which is based off of the technologies to be employed for LIGO Voyager. The facility will host two 40 km arms, 10 times the length of the LIGO detectors to improve the sensitivity to GWs. The goal is to be operational by 2035. [37, 38]

The second detector, dubbed the Einstein Telescope, has a *Laser Interferometer Space Antenna* (LISA) like configuration, using three arms in an equilateral triangle, of length 10 km. The sensitivity of this detector will be less sensitive above 10 Hz compared to Cosmic Explorer, but will be the most sensitive low frequency terrestrial detector to date below 10 Hz. As with Cosmic Explorer, the Einstein Telescope is planned to be operational by 2035. [39, 40]

1.3 Noise Sources

Using the example of LIGO, a detector with 4 km long arms [41], measuring GWs with strain amplitudes on the order of $h \sim 10^{-21} - 10^{-22}$ would result in arm length changes of $\Delta L \sim 10^{-18} - 10^{-19}$ m. This implies that the test masses of the detector must move with amplitudes smaller than ΔL in order for GWs to be distinguished from noise noise in the detector. There are a variety of different types of noise sources which plague detectors, ranging from quantum noise, thermal noise, seismic noise etc [42]. In this section a brief overview of these three major noise sources will be discussed. Figure 1.3 shows the predicted LIGO sensitivity curve which is dominated by seismic noise below 10 Hz, and quantum and thermal noises above this.

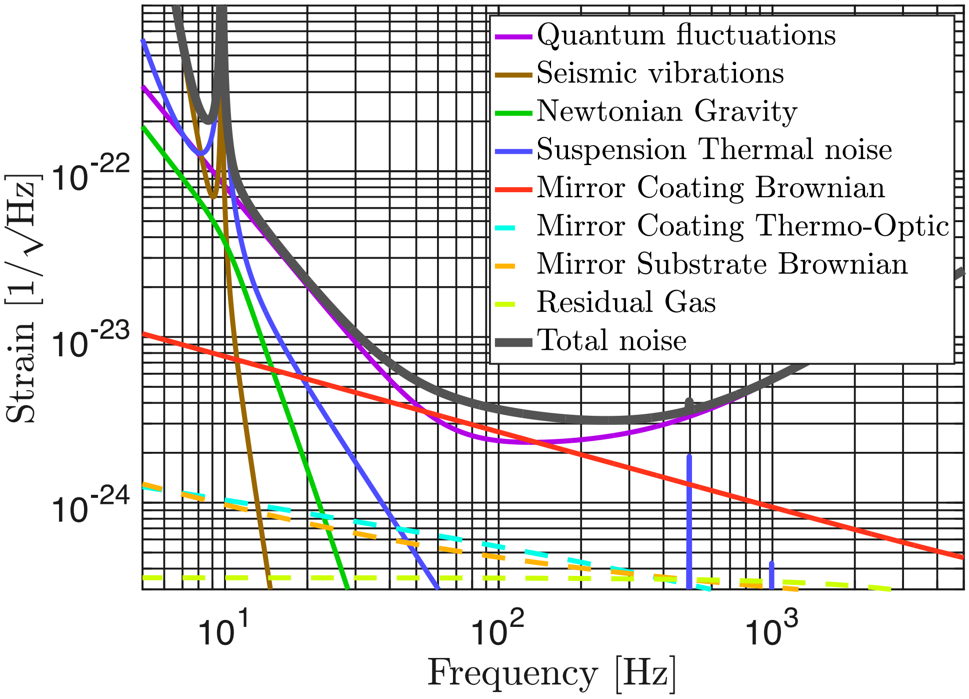

FIGURE 1.3: LIGO noise curve produced using the GWINC software [1] with the standard parameters.

1.3.1 Quantum Noise

Quantum noise can be separated into quantum radiation pressure and quantum shot noise. Both phenomena are a consequence of Poisson statistics. Radiation pressure occurs due to the fluctuation in the emission of photons from a laser source. For a fixed laser power, the average number of photons that are emitted per unit time, N, will fluctuate by $\sqrt{N}$. The ramification of this effect results in the number of photons incident on the test mass mirrors to vary over time, and due to the conservation of momentum, a force is imparted on the mirrors causing uncertainty in their position [43]. A force acting on a mass spring system has a frequency response of $1/f^2$ above its resonant frequency, therefore radiation pressure dominates at lower frequencies. Methods have been imposed to reduce the radiation pressure effect. Using heavier test masses increases their inertia, hence the test masses are less susceptible to the induced forces.

Shot noise occurs at the detection side. For an average of N photons that are incident at the photodetector, the uncertainty in the number of photons detected is $\sqrt{N}$. The fractional change in the number of detected photons is $\sqrt{N}/N = 1/\sqrt{N}$ [44], shot noise is thus frequency independent. Reduction of shot noise is achieved via increased laser power as this reduces the uncertainty in the number of photons detected. It is crucial to resonate a stable amount of power in the arm cavities such that the average number of photons remains constant so that the shot noise can be accurately modelled.

A range of quantum noise suppression techniques are also used such as squeezing [45] to improve the sensitivity beyond the *standard quantum limit* (SQL). In interferometry, the SQL is defined as the minimum level of quantum noise in the system, comprising of the shot noise and radiation pressure, also described as phase and amplitude noise respectively, when coherent states of light are used. The SQL is a boundary which the noise can not be below if only using classical techniques. As previously discussed increasing the laser power would reduce shot noise, but result in an increase in the radiation pressure noise.

1.3.2 Thermal Noise

Thermal noise is a broad term which covers many contributions of the random motion of particles throughout the system that are associated with their temperature. Passive velocity damping mechanisms such as air resistance and eddy current damping, and active damping schemes using electrostatic or electromagnetic drive contribute to the thermal noise in the system. In the case of active damping, the driving voltage/current fluctuates due to the thermal energy in the circuit. This imparts some noise on the drive when controlling the masses.

Depending on the materials used in the suspensions and substrates, cooling the detector can also reduce the thermal noise, the next generation of GW detectors aim to use silicon suspensions such that cooling would be beneficial [46, 39, 40]. The Japanese detector *Kamioka Gravitaional Wave Detector* (KAGRA) is a current cryogenic based detector which joined the network of detectors used for observation in 2020 [47].

Suspensions

The masses are susceptible to displacements due to the thermally induced motion of their suspensions [48]. Deformation of the fibres during bending has an associated loss angle, or phase lag between the stress and strain. These losses from the material properties are known as structural damping, and the associated loss angle is frequency dependent, comprising of the bulk, surface, and thermoelastic losses. By careful selection of the material and its dimensions, the thermal noise in the detection band can be minimised [49]. LIGO employs a monolithic suspension stage for the test masses, using fused silica for its mechanical and thermal properties [50]. The interface between materials can result in excessive stresses due to the different material properties between the components. Reducing the number of interfaces of different materials results in a higher quality suspension system and hence lower noise.

Coatings

Coating thermal noise appears due to a number of factors. The mirrors are heated due to the incident laser power in the cavities. This heating effect can lead to temperature gradients across the mirror surface due to its low thermal conductivity. A lensing effect is created due to the temperature dependence on the index of refraction causing instability of the cavity.

Brownian motion due to the mirror coatings results in displacement changes in the cavity length [51, 52]. Brownian noise also occurs in the mass substrate however its coupling to the differential arm motion, which is the measurement channel of GW detectors, is smaller than that of the coatings. Using larger beam sizes can reduce the thermally induced displacement noise from the coatings. The thermal induced Brownian motion of the atoms are incoherent, therefore an increase of the beam size results in averaging more surface atoms, resulting in a lower contribution in the overall noise. Imperfections in the coatings or on the surface can greatly increase the noise in the detector. Issues such as point absorbers can give rise to a large temperature spot on the mirror surface, leading to thermally induced deformations causing lensing and scattering of the laser beam.

1.3.3 Seismic Noise

The focus of this thesis is to improve the seismic isolation of GW detectors. Ground motion occurs due to a variety of factors ranging from human activities both in the local vicinity and further afield, wind, ocean waves and more. Detectors employ complex passive and active isolation methods to inhibit excess motion into the core optics of the detectors; such as inertial isolation and sensing, control techniques i.e. feedback and feedforward, active damping, and more. The large motion due to ground vibrations must be controlled below the GW detection bandwidth in order to maintain stability of the detector, which is a vital aspect for low frequency improvements of terrestrial detectors. Chapter 2 is dedicated to an overview on the causes of seismic noise, how we sense such motion, and isolate the detectors from it.

1.4 Thesis Overview

The structure of this thesis begins with an introduction to seismic noise and measurement methods used to detect residual input motion to the core optics of the LIGO detectors. Chapter 2 discusses the basis of inertial sensors and the basic isolation scheme employed within LIGO. An introduction into control theory is also provided with simple examples.

Chapter 3 introduces the 6D seismometer, a novel inertial sensor which aims to reduce the low frequency motion of the isolation platforms. A discussion on the needs for such a device are provided, and derivations of its dynamics, and predicted noises.

The second half of this thesis is devoted to experimental results on the tests of sensors for use in seismic isolation schemes in LIGO and its future upgrades. Chapter 4 is a published paper focusing on a prototype compact 6D seismometer, and in Chapter 5, a mature draft of a paper demonstrating the viability of a 6D seismometer for stabilisation of a six-axis platform is presented.

Chapter 6 moves away from 6D seismometers, and presents a mature draft of a paper investigating the cryogenic implementation of optical shadow sensors. These sensors are currently operational at room temperature in suspension chains of the LIGO detectors.

Chapter 2

Seismic Noise, Sensing, and Isolation

Chapter 2 is a review chapter, and no original work is presented.

2.1 Seismic Noise

Terrestrial motion such as seismic waves and wind are inherent noise sources in ground-based gravitational wave detectors. Examples of the seismic noise range from local human activity such as walking, transportation, anthropogenic motion etc. Disturbance of the ground is also caused by natural environmental phenomena.

Wind can cause tilt motion of buildings [53], which manifests as ground-induced platform motion from which the optics are suspended. The rotation also couples into the readout of translational seismometers which induces extra tilt into the isolation tables and suspensions in feedback if not accounted for.

Oceans waves that beat against the shores cause the majority of ground motion, this is known as the microseism [54]. Microseismic motion has a period ranging from 3 seconds to 30 seconds, where the largest contribution comes from the secondary microseism at 0.1 and 0.3 Hz. Earthquakes can severely increase the input motion to the optics and are primarily predominant in the $50 - 60\,\mathrm{mHz}$ band [55], however this source is not continuous like the others presented. Although the microseismic motion is outside of the band of detection, the large motion requires active feedback to keep the detector within its working regime. The active control causes excessive noise into the low frequency detection band up to 30 Hz, due to the stability constraints of the required control scheme.

It is necessary to isolate the components of the detector from such motion in order to minimise the differential movement between the main optics of the interferometer. In the low frequency regime below 10 Hz seismic motion dominates, this is inherent in ground-based detectors and limits the bandwidth of detection at $\sim 30\,\text{Hz}$ and below due to control noise [56]. Minimisation of this differential motion is required for multiple reasons.

As discussed in Chapter 1, detectors such as aLIGO must be sensitive to differential length changes of the arms on the order of $\Delta L \sim 10^{-18} - 10^{-19}\,\text{m}$ [57]. The input ground spectrum causes motion of the ground on the order of $x_g \sim 1\,\mu\text{m}$, requiring isolation of more than 10 orders of magnitude at frequencies in the detection band. Seismic isolation is necessary for a number of reasons:

(i) lock acquisition of the detectors. When undergoing the lock acquisition process, there is an upper limit on the velocity of the cavities as they sweep the locking regime. Reduction of the test mass motion would in turn increase the time period in which the cavities are within the locking regime [58], increasing the likelihood of lock acquisition.

(ii) The ground induced test mass motion would swamp the GW signals and due to differential ground motion in the detector arms, can potentially appear as false detections [59]. It is imperative to attenuate this motion below the displacement sensitivity of potential GW signals to increase the signal-to-noise ratio of detections.

(iii) The false alarm rate of detections is vastly improved with coincident measurements in detectors [60]. The combined uptime of GW detectors is increasing, resulting in advancement of real detection rate. Coincident detections hugely increases the likelihood of a real detection. Ground induced motion can result in the detector losing range and potentially lock, ergo, decreasing the coincident detection rate.

(iv) Simultaneous detections substantially enhance the localisation of sources. Low frequency controls noise clouds the inspiral signals of compact stellar mass objects, improvements below 30 Hz can provide early warning signs of mergers. This opens the opportunity for multi-messenger astronomy as was the case for GW170817 [17]. GW170817 was a special event due to it being a BNS system which is observable using electromagnetic detectors. The inspiral and merger frequencies were higher than that for BBH systems such that the signal was in the detection band sooner, enabling early warning signals for the electromagnetic detectors.

Isolation of the optics from the ground is achieved using a combination of passive and active isolation techniques. These techniques are dependent on the mechanical designs, sensors, and controls applied to the system in order to maximise shielding from external disturbances.

In this chapter, the principle behind seismic sensing using inertial sensors is discussed, and an overview of LIGOs passive and active isolation scheme is discussed using their *Basic Symmetric Chamber* (BSC) ISI as an example.

2.2 Inertial Sensors

Inertial sensors are simply a mass on a spring which utilise the inertial properties of a harmonic oscillator such that they act as an absolute sensor above their resonant frequency. This is different to displacement sensors that measure the relative distance between two points e.g. an interferometer or a *capacitive position sensor* (CPS).

The mass on a spring system illustrated in Figure 2.1 can be driven by the ground or an external force, and the position or velocity of the mass (known as a proof or reference mass) can be measured relative to the ground. Above the resonant frequency, the mass is inertial and therefore the measurement observed is purely that of the input ground motion. However below their resonant frequency, the signal measured is a combination of ground motion and the motion of the proof mass. Therefore inertial sensors are primarily used in the bandwidth above their resonant frequencies. Below their resonance, the noise of the device is still low enough that the signal-to-noise ratio of the ground motion is ample up to a decade in frequency lower for geophones such as the GS13 [61]. Conventionally, seismometers use a magnet-coil readout, therefore the output signal is proportional to the relative velocity between the mass and its surrounding housing, where the devices have a flat response to velocity above its resonance. Seismometers can be categorised as short period and broadband and are discussed in more detail in Section 2.2.2

Consider a driven mass on a spring, where the input is translational ground motion, x_g, and the position of the mass is denoted by x_m. From the system's equation of motion,

$$\begin{aligned} m\ddot{x}_m &= -b(\dot{x}_m - \dot{x}_g) - k(x_m - x_g) + F_{ext} \\ \implies m\ddot{\Delta x} &= -m\ddot{x}_g - b\dot{\Delta x} - k\Delta x + F_{ext}, \end{aligned} \tag{2.1}$$

where m is the mass, b is the viscous damping coefficient, k is the spring constant, F_{ext} is the external force acting on the mass, and $\Delta x = x_g - x_m$ is the differential

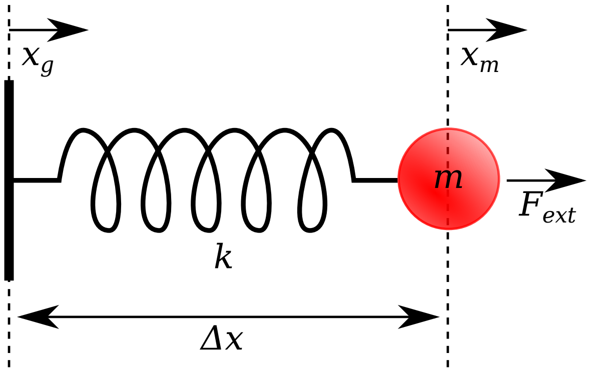

FIGURE 2.1: A mass on spring system with spring constant k, showing the input ground displacement x_g, the mass m, an external force acting on the mass F_{ext} and the position of the mass x_m. The distance Δx is the difference in position between the ground and the mass.

position between the ground and mass positions, the frequency domain transfer function of the system can be determined. Frequency domain analysis is more beneficial in understanding the system's dynamics as the response can be investigated in terms of its magnitude and phase.

The response of the mass position to ground motion is,

$$\frac{\tilde{x}_m(\omega)}{\tilde{x}_g(\omega)} = \frac{\omega_0^2 + i\omega\omega_0/Q}{\omega_0^2 + i\omega\omega_0/Q - \omega^2}, \tag{2.2}$$

where $\omega_0 = \sqrt{k/m}$ is the resonant frequency of the system in rad/s ($\omega = 2\pi f$, where f is the frequency in Hz), and Q is a dimensionless constant representing the damping of the system. For the definition used here, $Q = m\omega_0/b$. At DC, the response of the mass follows that of the ground motion as $\tilde{x}_m = \tilde{x}_g$. For a high Q system where there is small loss in energy, at the resonant frequency the mass motion is amplified such that $|\tilde{x}_m| \approx Q|\tilde{x}_g|$. Above the resonance the response falls as $1/\omega^2$, and above the corner frequency of $\omega > \omega_0 Q$, the system responds as $1/\omega$. This can be seen in Figure 2.2.

External forces can also cause changes in the mass motion, where

$$\frac{\tilde{x}_m(\omega)}{\tilde{F}_{ext}(\omega)} = \frac{1}{m(\omega_0^2 + i\omega\omega_0/Q - \omega^2)}. \tag{2.3}$$

Note that at frequencies much lower than the resonance ω_0, the system asymptotes to a value of $1/k$, therefore for stiffer systems a larger force is required to change its DC position. The response of the mass to a force is also the same for the sensed displacement Δx, and provides intuition for the actuation applied to a system.

The nature of inertial sensors only allows for the measurement of the differential position Δx. Therefore, the transfer function of ground motion into the differential measurement is required and the resultant transfer function becomes,

$$\frac{\Delta\tilde{x}(\omega)}{\tilde{x}_g(\omega)} = \frac{\omega^2}{\omega_0^2 + i\omega\omega_0/Q - \omega^2}. \tag{2.4}$$

Inertial sensors are inherently used to measure the input motion, x_g, however the output of the sensor is the signal Δx. Therefore the inversion of Equation (2.4) retrieves the ground motion input. A consequence of this inversion shown in Equation (2.5) - which recovers the lack of response of the sensor below its resonance - is that any accompanying sensor noise is also amplified at low frequency,

$$\frac{\tilde{x}_g(\omega)}{\Delta\tilde{x}(\omega)} = \frac{\omega_0^2 + i\omega\omega_0/Q - \omega^2}{-\omega^2}. \tag{2.5}$$

As mentioned above, seismometers usually have an output which is flat to input velocity above its resonance, therefore the response to ground displacement is grows as ω above the resonance. The inverted sensor response for a seismometer to ground displacement is

$$\frac{\tilde{x}_g(\omega)}{\Delta\dot{\tilde{x}}(\omega)} = \frac{\omega_0^2 + i\omega\omega_0/Q - \omega^2}{-i\omega^3}, \tag{2.6}$$

which has a response proportional to $1/f^3$ below its resonance. Therefore noise is amplified at a much faster rate below its inertial response than for a displacement sensor readout scheme as shown in Figure 2.2. More detailed is provided in Section 2.2.2.

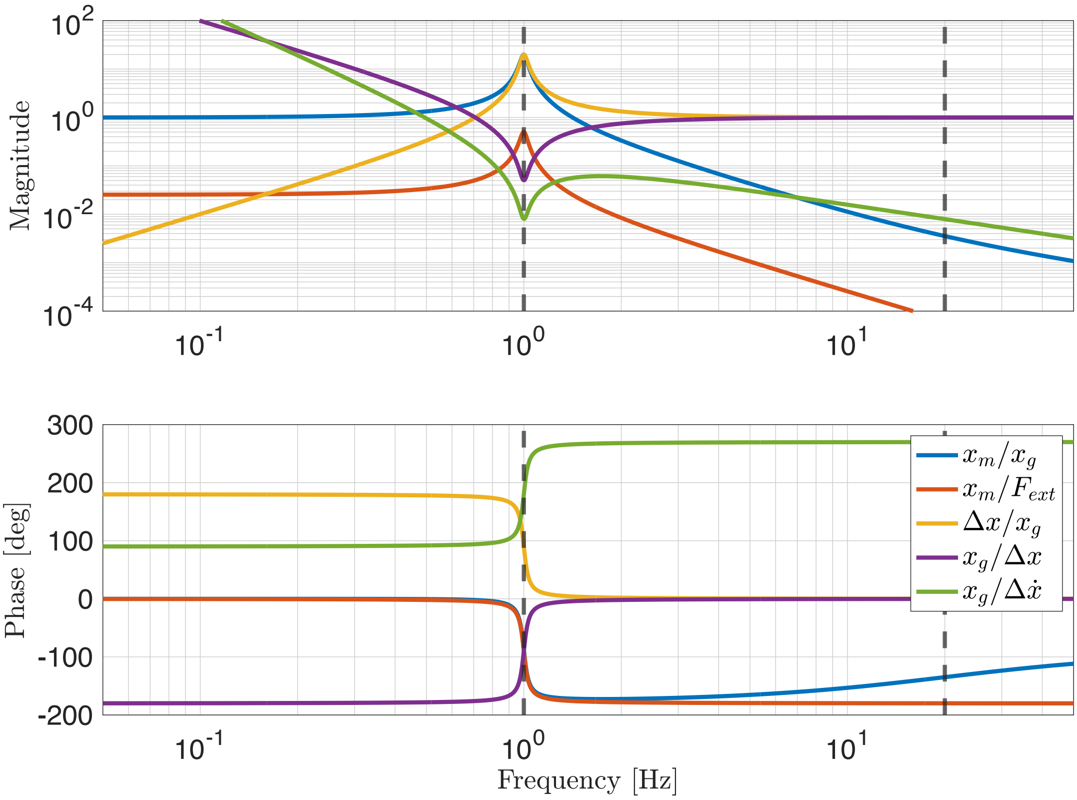

FIGURE 2.2: Transfer function responses for a mass on a spring. The blue curve describes the response of the mass to ground motion. The dashed black line at 20 Hz shows where the response of the mass motion changes from $1/f^2$ to $1/f$. Red indicates the reaction with respect to an external force . The yellow curve shows the differential position of the mass and ground due to input ground motion (the output of the inertial sensor). The purple curve shows the inverted response of the sensor which shows how the sensor response relates to the measured ground motion. The green curve is the inverted displacement response for a seismometer which uses a relative velocity readout scheme.

2.2.1 Tilt Coupling

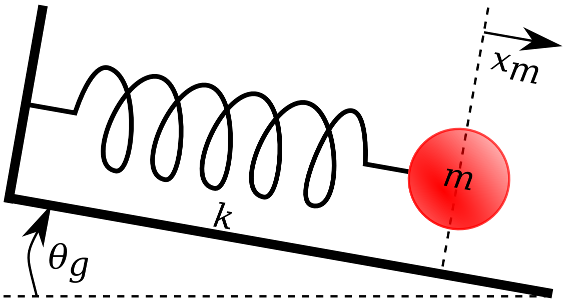

FIGURE 2.3: Schematic of tilt induced translation for a mass on a spring system.

Tilt to horizontal coupling plagues inertial sensor readout towards lower frequencies. Tilt motion of the ground, θ_g, as indicated in Figure 2.3 causes extension of the mass spring system due to the gravitational component of the mass along the axis of measurement. The linear one degree of freedom sensor would therefore measure a change in the displacement sensed. This would be indistinguishable to that of translational motion of the ground.

The transfer function of the sensed motion Δx due to the ground tilt is described as

$$\frac{\Delta\tilde{x}(\omega)}{\tilde{\theta}_g(\omega)} = \frac{g}{\omega_0^2 + i\omega\omega_0/Q - \omega^2}. \tag{2.7}$$

However when the sensed motion is inverted to account for the lack of response at the sensor at lower frequencies, we determine the new tilt induced ground motion transfer function as [3, 62, 63, 64, 65],

$$\frac{\tilde{x}_{\text{inferred}}(\omega)}{\tilde{\theta}_g(\omega)} = \frac{\Delta\tilde{x}(\omega)}{\tilde{\theta}_g(\omega)}\frac{\tilde{x}_g(\omega)}{\Delta\tilde{x}(\omega)} = -\frac{g}{\omega^2}. \tag{2.8}$$

The inferred translational measurement results in an infinite response at DC due to the tilt motion. As previously stated, this is indistinguishable from actual measured translation and cannot be removed. This limits the sensors capabilities when $\omega < \omega_0$. Consequently, using this signal in feedback would result in injection of the sensed ground rotation into the platform rather than minimisation of the translational motion.

2.2.2 Sensor Responses

The mechanics of the inertial mass spring system outlined in Section 2.2 is the basis for nearly all types of seismic sensors. Short period seismometers are passive suspension systems as described above, which use magnet coil readouts to measure the relative velocity between the proof mass and its surroundings. The response to velocity is flat above its resonance, however it is difficult to create passive systems with resonant frequencies below 1 Hz.

Accelerometers are also used as seismic sensors, but have a response to acceleration which is flat below the resonance of the device. This enables them to measure accelerations down to zero frequency, using relative displacement sensors such as capacitive sensing or strain gauges. These devices are primarily used to measure large accelerations, as a result they have relatively low sensitivities compared to seismometers.

Bridging the gap between these devices are broadband seismometers. Broadband seismometers use active control techniques to reduce the effective resonance such that the detection bandwidth of the device can be increased. The measurement signal of the passive seismometer can instead be used as an actuator to feedback to the proof mass inside the device. Therefore rather than using the magnet coil system as a sensor, it is used to feedback a force to the mass. Instead a displacement transducer such as a capacitive sensor is used to readout the relative displacement between the mass and the surroundings and is used for both the measurement and the feedback signal. The active force feedback results in an effective lower resonant frequency.

Figure 2.4 shows the arbitrary velocity and acceleration responses for the three types of sensors discussed. All of the curves have been normalised to the velocity response of the short period seismometer at 100 Hz.

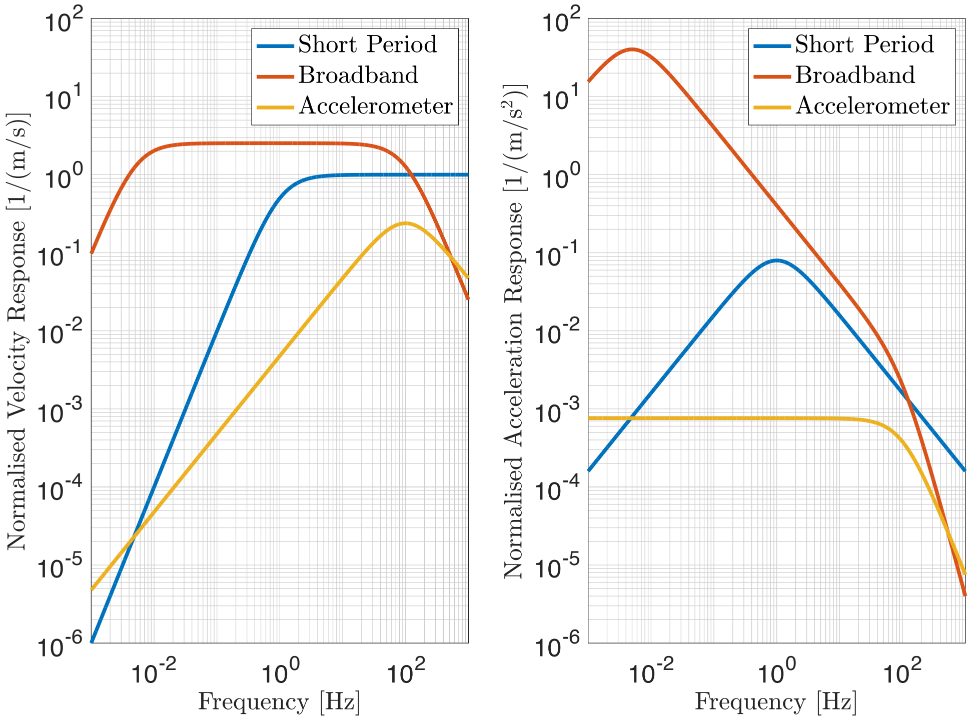

FIGURE 2.4: **Left:** Responses of the various seismic sensors to velocity normalised to the short period seismometer at 100 Hz. **Right:** Acceleration response of the sensors according to the normalisation of the short period seismometer with respect to velocity.

2.3 Passive Isolation

The core optics of GW detectors and the platforms from which they are suspended are partially shielded from ground disturbances using the inertial properties of the mass-spring system discussed in Section 2.2. First we begin with the suspensions of the optics. A pendulum design is implemented which creates the $1/f^2$ isolation above its resonance, where the resonant frequency is given by $\omega_0 = \sqrt{g/L}$. Ideally the pendulum length, L, would be infinitely long such that within the detection bandwidth the residual ground motion of the optics would be zero. Practical constraints such as the size of the vacuum chambers, cost, etc limit the length. LIGO implements a quadruple suspension design, inspired by the GEO 600 triple suspensions [66]. Each suspended mass acts as another low pass filter providing a further factor of $1/f^2$ isolation than the previous suspended mass. For a suspension chain with n stages, above the resonant frequencies, the isolation achieved is

$$\frac{\tilde{x}_{\text{final}}}{\tilde{x}_g} \propto \frac{1}{f^{2n}}, \tag{2.9}$$

where x_{final} is the position of the final mass in the chain. The pendulum modes for the core optics of LIGO are between $0.4 - 4\,\text{Hz}$ [67], resulting in the final test mass obtaining $1/f^8$ isolation in the detection band above $10\,\text{Hz}$. Many of the auxiliary optics within the detector are also suspended to minimise excess motion, however their pendulum lengths are much shorter and contain fewer stages.

The platforms from which the core optics are suspended are known as the ISI which is contained within the BSC. The BSC-ISI is a two stage suspended platform [68, 69] which provides $1/f^4$ isolation above its resonances. The first stage of the platform known as stage 1 is suspended from the rigid stage 0 structure via blade springs and flexures as indicated in Figure 2.5. The stage 2 structure is suspended in a similar fashion from stage 1. Orientation and placements of the blade springs and flexures result in both in phase and out of phase modes for all six degrees of freedom (X, Y, Z, RX, RY, RZ - 3 translational degrees of freedom, and 3 rotational about the respective

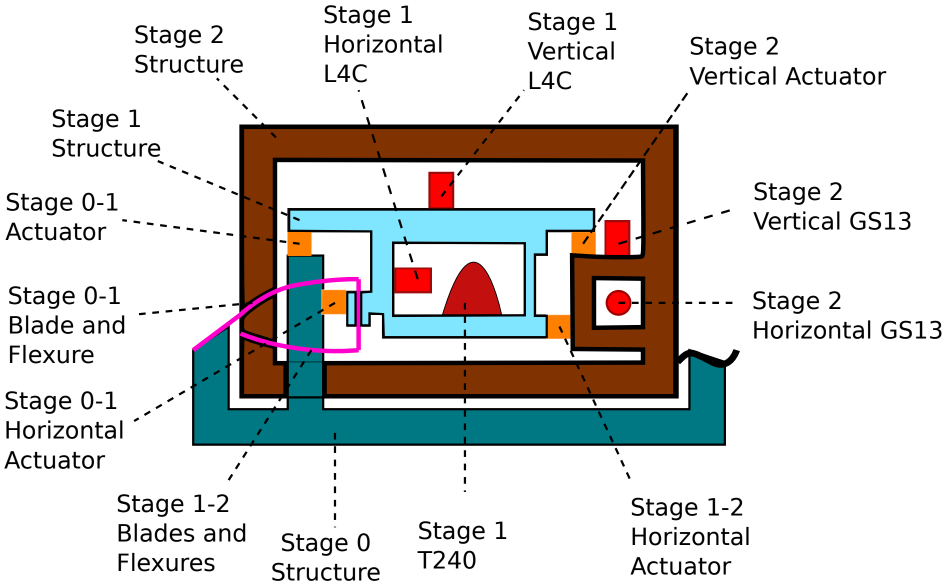
Stage 2
Structure
Stage 1
Horizontal
L4C
Stage 1
Vertical
L4C
Stage 2
Vertical Actuator
Stage 1
Structure
Stage 0-1
Actuator
Stage 2
Vertical GS13
Stage 0-1
Blade and
Flexure
Stage 2
Horizontal GS13
Stage 0-1
Horizontal
Actuator
Stage 1-2
Blades and
Flexures
Stage 0
Structure
Stage 1
T240
Stage 1-2
Horizontal
Actuator

FIGURE 2.5: A schematic of the BSC-ISI illustrating the instruments used to actively control the platform. The figure has been adapted from reference [2].

axes) of the stage 2 structure, where the in phase modes lie between $1-2\,\mathrm{Hz}$ and out of phase modes between $5-7\,\mathrm{Hz}$ [2, 69].

Combing the passive suppression from the BSC-ISI and the quadruple suspension system, a factor of $1/f^{12}$ isolation can potentially be achieved in the detection band. From our previous order of magnitude approximation (see Section 2.1), achieving the required displacement of the final test mass mirrors would require attenuation of the input ground motion by approximately 12 orders of magnitude.

Note that the benches at both the Albert Einstein Institute 10 m Prototype and Virgo use a combination of inverted pendulums and geometric anti-springs [70, 71]. The anti-spring and inverted pendulum system allows for tuning of the resonant frequency of the optical tables to lower frequencies than a typical mass on spring isolation system which is used in LIGO. The advantage of pushing the resonance to lower frequencies is that the $1/f^2$ passive isolation begins at lower frequency, therefore greater isolation is achieved within the detection band, however this design method increases the complexity of the system.

2.4 Active Isolation

Passive isolation is limited to the frequency range above the resonant frequencies of the mass-spring like systems involved. At 10 Hz the detector is still limited by seismic motion as shown in Figure 1.3. Therefore at 10 Hz and below, only the active isolation of the platform can suppress the seismic motion. This, combined with the fact that seismic motion is large in nature results in the differential arm motion of the interferometer being dominated by seismic noise in this frequency regime. Motion is less common between the mirrors at high frequency, however there is larger attenuation due to the passive isolation of the suspended optics. The relevant control theory is detailed in Section 2.5 where the principles of feedback, feedforward, and sensor blending are discussed.

A number of active isolation techniques have been employed to the BSC-ISI system to mitigate the effect of input ground motion on the suspension chain. The BSC is located atop a *Hydraulic External Pre-Isolator* (HEPI) [72]. HEPIs combine an array of components to provide pre-isolation to the BSC-ISI. Active isolation requires sensing and actuation - in the case of the HEPIs sensing is accomplished via inductive position sensors, and geophones, and actuation with hydraulic actuators [2]. This system is no longer used in active feedback as the actuation causes excessive tilt motion of the ISI. Only the DC position of the BSC-ISIs are controlled using the HEPIs.

The BSC-ISI stage 1 is equipped with six CPSs and three 3-axis T240 [73] and six L4C [74] seismometers. Stage 2 has six CPSs and six GS13s geophones. The seismometers and geophones are used to sense the inertial motion of the platforms, while the CPSs measure the relative positions between the current and previous stages.

There are 12 degrees of freedom are present (six for stage 1 and six for stage 2) which are all controlled independently (single input single output feedback) [69]. The T240 sensors on stage 1 are used for feedback on stage 1, and as feedforward sensors for stage 2.

Sensor blending - which is discussed in Section 2.5.3 - is used to combine the different relative displacement and inertial sensors to increase sensitivity of seismic detection over a larger bandwidth, improving the broadband isolation.

As with the majority of translational sensors, tilt-to-horizontal coupling limits the low frequency isolation of the platform. A number of *beam rotation sensor*s (BRSs) [3] have been implemented which measure absolute rotation of the ground above the resonant frequency of the beam balance. However if the motion between the translational seismometers and the rotation sensor are not coherent, the tilt cannot be removed from the translational sensor [53]. Also, the ground tilt that is measured is not the same as the platform tilt which makes correcting the sensor more difficult [75].

2.5 Control Theory

In order to control a system, some form of actuation is required to impart a change to the system. However in order to determine the change that is required, we must also sense the system as discussed in Section 2.4. In this section we will methodology and ideas of control theory which are the basis behind the BSC-ISI control scheme.

2.5.1 Feedback and Stability

Feedback is a method of correction whereby the measurement of the system is used to control the system itself. Consider an actuator A acting on a dynamic system P which is sensed by a sensor S shown in Figure 2.6. Every component of the system is likely to have some frequency dependence, such as the inertial sensors described in Section 2.2.

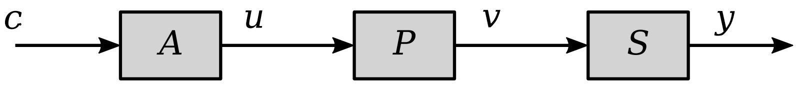

FIGURE 2.6: A block diagram of the signal flow from an input signal c to the measured output y through an actuator A, plant P, and sensor S.

Following the signal path, the corresponding sensed output, y with respect to the input control signal c is given as

$$\begin{aligned} y(\omega) &= S(\omega)P(\omega)A(\omega)c(\omega) \\ &= H(\omega)c(\omega), \end{aligned} \tag{2.10}$$

where $H = SPA$, and is defined as the open loop transfer function of the system. With this configuration, the plant, P, can be moved, however feedback has not been implemented as the sensed signal has not been utilised. Consider that we wish to move the plant to a desired position c, by feeding the measured signal back in with the control signal, we can gain a new more intuitive input to the actuator, e. This new signal is known as the error signal and tells us how far away from the desired position the system is, where $e(\omega) = c(\omega) - y(\omega)$. This new configuration is shown in Figure 2.7.

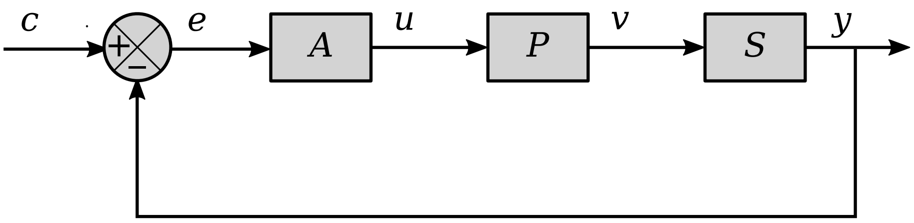

FIGURE 2.7: A block diagram indicating the closed loop operation of a system.

Analysing the signal flow from Figure 2.7, the output signal y becomes,

$$\begin{aligned} y(\omega) &= S(\omega)P(\omega)A(\omega)e(\omega) \\ &= H(\omega)(c(\omega) - y(\omega)) \\ \therefore y(\omega) &= \frac{H(\omega)}{H(\omega)+1}c(\omega). \end{aligned} \tag{2.11}$$

From Equation (2.11), we see that if the open loop has sufficiently large gain, the measured output signal will approximate that of the input control signal.

Unfortunately, in reality a system does not allow for an infinitely large open loop gain across all frequencies. Analysis of Equation (2.11) shows that the transfer function $H/(H+1)$ becomes infinite at the point where $H = -1$, or in other words, when $|H| = 1$ with a phase lag of π or $-\pi$ [76]. This implies that the system will always be unstable if at the unity gain frequency, the open loop gain is greater than second order (system is theoretically stable if $-2 \leq n \leq 2$). Considering the frequency domain - where H is an n^{th} order system represented by polynomials of order $(-i\omega)^n$ - terms of $-i^n$ would result in phase lags for the system corresponding to the order of the polynomial, where the phase lag is $n\frac{\pi}{2}$. Therefore, the open loop gain must cross unity gain with a phase lag within the range of $\pm\pi$, corresponding to a slope with a gradient between f^{-2} and f^{2} [77].

2.5.2 Feedforward

The feedforward method is used to account for the response of a system due to external disturbances. If the external disturbance can be measured, the knowledge of this disturbance can be implemented to the actuation in some fashion to account for this [78]. For the BSC-ISI case, a measurement of the ground induced motion of previous stage is made and is subtracted from the actuation signal. Feedforward is also used in the form of sensor correction. The CPSs used measure the difference between the various stages of the system. However the signal of interest is the inertial motion of the platform in the lab frame rather than the relative displacements. Inertial measurements of the previous stage can be used to correct the CPSs signals such that the new measurement becomes a quasi-inertial measurement of the particular stage of interest [68, 69].

A simplified scheme to indicate the concept is shown in Figure 2.8.

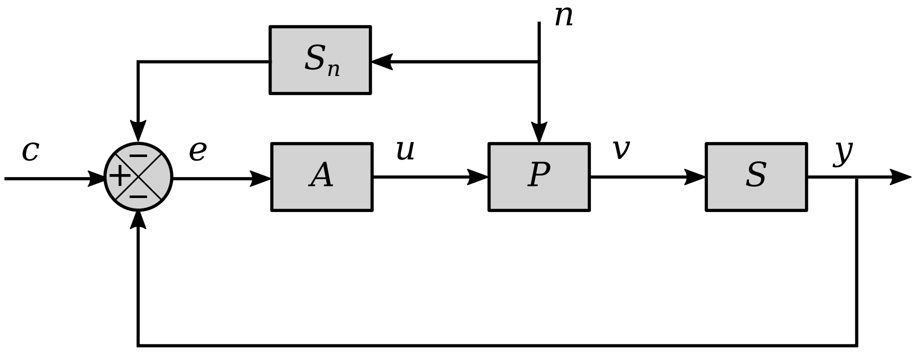

FIGURE 2.8: A block diagram illustrating the implementation of a feedforward signal to minimise the input noise n.

For simplicity we can set the control signal $c = 0$. The purpose of the control is then only to minimise the input noise to the system, n. This is more akin to the isolation concept used for minimising the input ground motion to the BSC-ISI. Assuming no control is implemented, we find that $y(\omega) = S(\omega)P(\omega)n(\omega)$. When control is implemented, the error signal $e(\omega) = -y(\omega) - S_n(\omega)n(\omega)$. Here, S_n is both the sensors response and a correction filter. The resultant output signal becomes,

$$\begin{aligned} y(\omega) &= S(\omega)P(\omega)(n(\omega) + A(\omega)e(\omega)) \\ &= H(\omega)e(\omega) + S(\omega)P(\omega)n(\omega) \\ &= (S(\omega)P(\omega) - H(\omega)S_n(\omega))n(\omega) - H(\omega)y(\omega), \\ \therefore y(\omega) &= \underbrace{\frac{S(\omega)P(\omega)}{H(\omega)+1}}_{\text{feedback}} n(\omega) - \underbrace{\frac{H(\omega)S_n(\omega)}{H(\omega)+1}}_{\text{feedforward}} n(\omega). \end{aligned} \tag{2.12}$$

The feedback term shows that with infinitely high gain the noise can be mitigated, however this is not practically possible due to a combination of stability, limitations on actuator strength, and range. By suitably constructing a filter for the feedforward scheme, the input noise can further be minimised to a better standard than with feedback alone.

2.5.3 Sensor Blending

Filters can be used to alter or combine signals in signal processing and feedback systems. the two basic categories of filters are high pass and low pass, which allow signals of high frequency and low frequency through, respectively.

Sensors are blended when they are combined to improve a systems overall response. A simple example is when two sensors are present which measure one observable, one which is sensitive to low frequency, and the other sensitive to high frequency. Applying a high pass filter to the signal which is sensitive in the high frequency regime, and a low pass filter to the low frequency signal allows us to prevent the injection of excess noise from the sensors back into the control loop. Combining the two filtered signals results in a final signal which is more sensitive than the individual signals on their own across a wide frequency band. However, at the cross over frequency, there will be a slight degradation of the overall sensitivity as a trade-off of gaining an overall improvement. The cross over frequency is defined as the point where the magnitudes of the two filters cross one another. This is a tunable parameter dependent on the characteristics of each filter.

When in feedback it is important to maintain stability of the control loop. This sets limitations of the blending scheme of the filters. Stability is discussed in Section 2.5.1.

The inertial sensors used on the BSC-ISI are frequency dependent, and as shown in Section 2.2, degrade at frequencies below their resonance. To combat the degradation in the signal, we invert the sensors response to boost the lower frequency measurements, however this amplifies the noise of the sensor. A blending scheme can be utilised which combines signals from two or more sensors creating a new signal. In the case of the BSC-ISI, the stage 2 motion is measured using GS13 seismometers and the sensor corrected CPSs measure the difference between stage 2 and stage 1. Above the resonance of the GS13, the noise is superior to that of the CPSs. However due to the amplification of the GS13 noise during the inversion process, the CPS noise surpasses that of the GS13 in the low frequency regime.

When combining the signals, the summation of the two filters must be equal to 1,

$$h(\omega) + l(\omega) = 1, \tag{2.13}$$

where $h(\omega)$ and $l(\omega)$ are the high and low pass filters respectively. A simple way to achieve this is to create a single filter, therefore the second filter would be

$$h(\omega) = 1 - l(\omega). \tag{2.14}$$

A more complex method would be designing each filter, $l(\omega)$ and $h(\omega)$ individually for each signal, and then normalising them to each other such that the filters sum to 1,

$$\begin{aligned} H(\omega) &= \frac{h(\omega)}{h(\omega)+l(\omega)} = \frac{1}{1+\frac{l(\omega)}{h(\omega)}}, \\ L(\omega) &= \frac{l(\omega)}{h(\omega)+l(\omega)} = \frac{1}{1+\frac{h(\omega)}{l(\omega)}}. \end{aligned} \tag{2.15}$$

This property means the filters are complementary and is a requirement in feedback systems. An issue with this normalisation is that it can potentially violate the stability criteria discussed in Section 2.5.1.

A simple way of always constructing a higher order complementary pair of stable filters is to choose an n^{th} order polynomial $(\sigma - i\omega)^n$. The requirement of the filters is that they must sum to 1, therefore two fractions can be constructed which have a denominator which is the polynomial. The numerators are the expanded terms of the polynomial which are separated between the two fractions as shown in reference [70].

2.6 Summary

Control and stabilisation of the platforms from which the core optics are suspended is paramount in the functioning of GW detectors. A combination of sensing, actuation, and control techniques are necessary for robust operation. The current systems employed at the LIGO detectors are mainly limited by the control noises below 30 Hz. Improvements of the sensor noise of the devices used in the low frequency control - such as the inertial sensors - can reduce the bandwidth of these control loops. This in turn would result in a reduction of the noise injection into the detection channel. A number of projects are being investigated to reduce sensing noise, such as compact optical sensors, interferometric inertial sensors, and vacuum compatible tilt sensors.

Chapter 3

The six degree of freedom (6D) inertial sensor

Chapter 3 details original work undertaken by myself, developing on the project discussed in [79].

3.1 Background

As discussed in Section 2.2, tilt-to-horizontal coupling is the main limitation of inertial sensors and isolation systems in their low frequency regime [63]. Vertical seismometers are used as a proxy for the measured tilt motion of the platforms at LIGO, which are then subtracted from the horizontal sensors to reduce the tilt coupling effects. However, the subtraction of the inferred tilt measurement is limited by the coherence between the tilt signals and the translational measurements of the platforms, due in part to the effective tilt resonance which is approximately 0.7 Hz.

A variety of devices have been proposed to improve the sensing scheme of the platforms including interferometric translational inertial sensors [80, 81], and absolute rotation sensors [3, 8, 82, 83]. The primary goal is to reduce the input motion to the suspension chains in order to minimise the bandwidth of the auxiliary length and alignment controls of the optics [84]. This is the dominant noise source for the LIGO detectors below 30 Hz [36].

In this chapter we investigate an alternative sensing device, the 6D seismometer, proposed by Dr. Conor Mow-Lowry and Dr. Denis Martynov [79]. Contrary to custom and commercial translation seismometers, and custom rotation sensors, the project details a three-arm extended reference mass suspended from a single fused silica fibre [49]. This results in a reference mass which is softly suspended in six degrees of freedom which is sensed simultaneously. A low noise compact interferometric readout device known as HoQI was suggested for sensing which has a preferential large dynamic range [85]. The advantage of this design is the need for only a single reference mass to stabilise the LIGO platforms in all degrees of freedom.

The mass is constrained by small forces which are defined by engineering choices, the geometry of the system, and actuation forces. Cross coupling such as tilt-to-horizontal motion as discussed in Section 2.2 plague current sensors, however for 6D, cross couplings are allowed to occur as all degrees of freedom are sensed simultaneously. System identification is paramount in the concept of 6D as it allows for the cross couplings to be diagonalised and mitigate the issues seen in many 1D sensors. Inertial tilt sensing allows for corrections of the translational readouts which improves the low frequency sensing.

The design is inspired by the drag-free approach implemented in the LISA pathfinder mission [86], where a freely falling test mass is used as a reference, and the surrounding housing is actuated on such that it follows the test mass. Above the resonant frequencies of the 6D proof mass, the system behaves inertially, and the platform is controlled to follow its position. Actuation is also used on the reference mass to mitigate any forces which cause excessive motion beyond the seismic induced platform vibrations.

A simplistic design of a single softly suspended mass presents its own challenges. Angular modes with low resonances can be highly susceptible to unwanted input motion and the long periods and Q-factors, which can theoretically be upward of 10^6, result in experimental difficulties. Operating the system in vacuum reduces the susceptibility to some of these noise sources, and is also a necessity for compatibility in the LIGO BSCs. Damping of the resonant modes is required to reduce the RMS motion of the mass and improve stability to the control scheme. Figure 3.1 shows the CAD model of the 6D design atop the ISI style platform inside the vacuum chamber. The sensing and local damping using HoQIs and BOSEMs are highlighted in magenta.

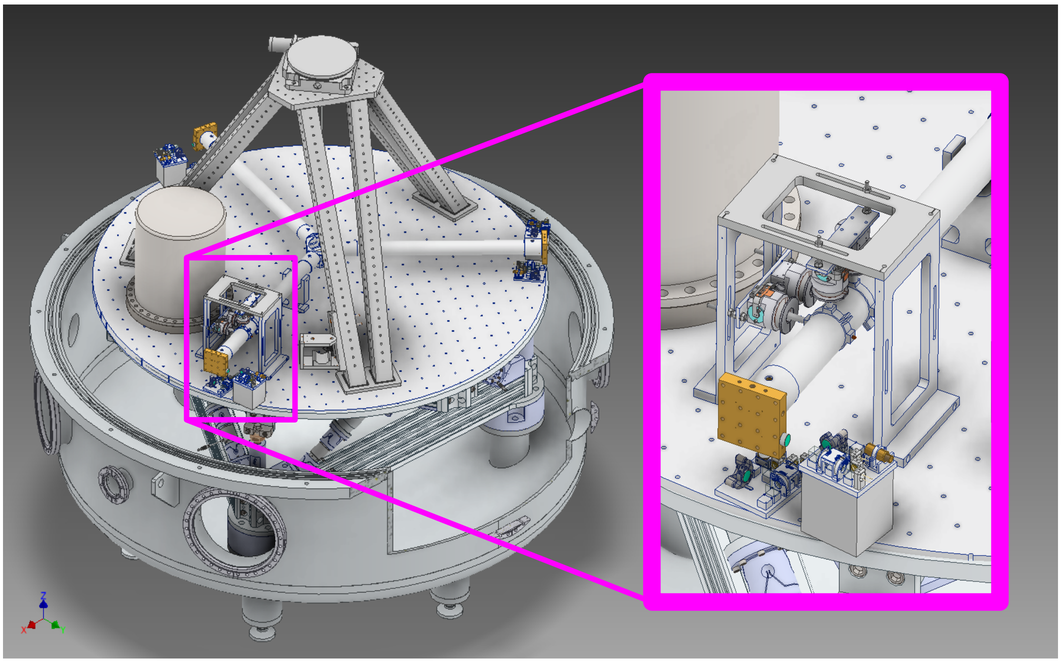

FIGURE 3.1: CAD drawings designed by Dr. Leonid Prokhorov, Dr. Samuel Cooper, and I, of the final 6D experimental setup inside the vacuum chamber. The highlighted magenta region focuses on the readout scheme using HoQIs and the damping control with BOSEMs.

In this chapter, an analysis of the dynamics of the 6D seismometer are presented, where the full Lagrangian is shown for completeness. The system is then simplified into separate cases which can be solved analytically, to provide intuitive understanding of the systems dynamics. Using the results of the model, noise budgets are calculated for the individual degrees of freedom. Finally, a second model is introduced which shows derivation of the actuation matrix for the ISI platform which will be used for stabilisation.

3.2 Design Parameters

Design of the test mass suspension was made by Dr. Leonid Prokhorov. The parameters were chosen to maximise the moments of inertia of the system. Reduction of the tilt modes results in decoupling of tilt to translational motion to lower frequencies due to lower frequency inertial tilt sensing. The desire for a large moment of inertia drives many of the design choices for the system, where the moment of inertia, I, for a point mass, m, at a distance r from the rotation axis is defined as $I = mr^2$. Maximisation of the moment of inertia is achieved by placing the majority of the mass as far as possible from the pivot point. The radius is set to $R_m = 0.5\,\mathrm{m}$ such that it extends across the platform (diameter $= 1.3\,\mathrm{m}$) as much as possible. To maximise the mass contribution at the ends of the arms, 1 kg masses are placed at the ends of cylindrical, hollow aluminium tubes. These tubes are designed with minimal wall thickness to reduce their weight, and the central anchor of the mass is designed as a frame like structure - a combination of these choices results in a maximised moment of inertia, where the contribution from the arms and central anchor are negligible compared to the end masses. To reduce potential magnetic noise couplings, the extended reference mass is constructed of brass, aluminium, and titanium. A CAD drawing of the test mass is shown in Figure 3.2.

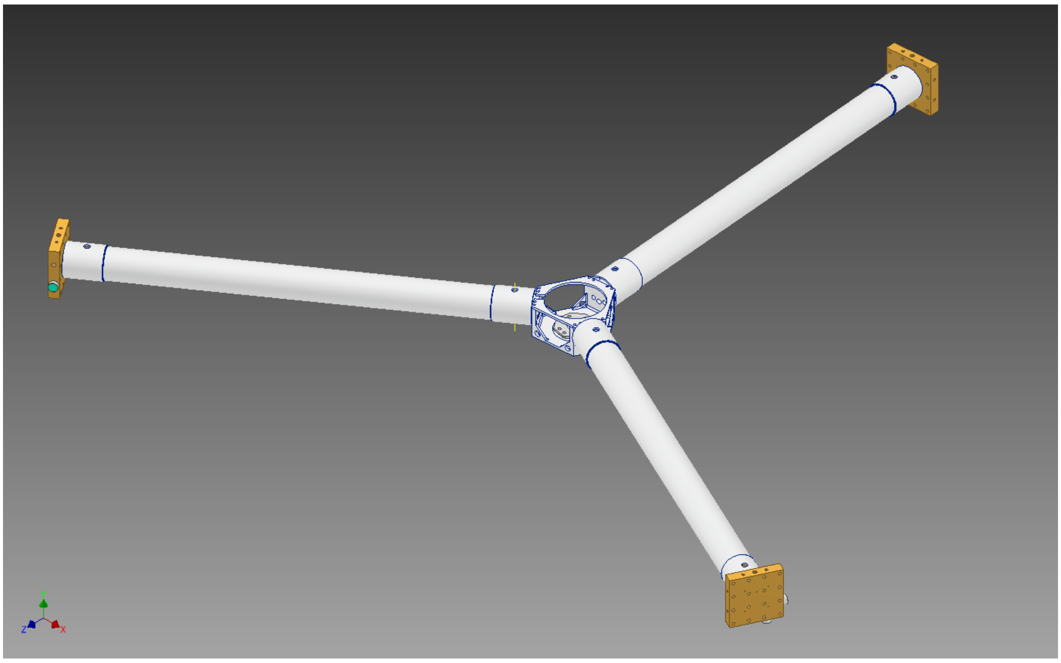

FIGURE 3.2: CAD drawing designed by Dr. Leonid Prokhorov of the 6D test mass.

A fused silica fibre was proposed due to its low thermal noise [50] and high tensile strength. The University of Glasgow have produced and continue to develop fibres for aLIGO, proving their durability and suitability for use in low noise suspensions. A specific fibre radius has been chosen to minimise the thermoelastic noise [49] of the suspension and still remain below its yield stress. The thermoelastic noise is the corresponding thermal noise due to the elastic deformation caused during bending, where compressed areas increase in temperature, and the extended regions reduce in temperature.

A list of the system parameters are shown in Table 3.1 on page 44.

The restoring forces for the degrees of freedom have varying origins. The extension and compression of the fibre behaves as a linear spring for the vertical bounce mode. The linear spring constant of the fibre is

Table 3.1: A list of parameters and nominal values for the final idealised 6D design.

Parameters	Description	Value
M_m	Mass	3.6 kg
R_m	Mass radius	0.5 m
L_w	Wire length	0.64 m
L_{bend}	Wire bending length $= \sqrt{E\pi r_w^4/4M_m g}$	450 μm
L_{offset}	Centre of mass offset	$-664\,\mu$m
d	Centre of mass position relative to bending point	$L_{bend} + L_{offset}$
r_w	Fibre radius at bending points	106 μm
E	Youngs Modulus of fibre [87]	72 GPa
G	Shear Modulus of fibre [88]	31.2 GPa
ϕ	Loss angle of fibre [49]	10^{-6}
I_x, I_y	Moment of inertia about x, y axes	0.375 kgm^2
I_z	Moment of inertia about z axis ($I_z = I_x + I_y$)	0.75 kgm^2
$f_{\mathrm{X,Y}}$	Translational resonance	0.64 Hz
f_{Z}	Vertical resonance	5 Hz
$f_{\mathrm{RX,RY}}$	Tilt resonance	5 mHz
f_{RZ}	Torsional resonance	0.8 mHz

$$k_z = \frac{E(1+i\phi)A_w}{L_w}, \tag{3.1}$$

where A_w is the cross sectional area of the fibre. The spring constant for the torsional mode about the z-axis is

$$k_{tor} = \frac{G(1+i\phi)J}{L_w}, \tag{3.2}$$

with J being the torsional constant. For a fibre with a circular cross section, this is equivalent to the second moment of area about the z-axis, $J = I_a = \pi r_w^4/2$. The final restoring force due to the fibre properties is the elastic bending force,

$$k_{el} = \frac{1}{2}\sqrt{M_m g E(1+i\phi)\pi r_w^4/4}. \tag{3.3}$$

The bending constant, k_{el}, is paramount in determining the resonance for the tilt eigenmodes as the restoring moment, due to the fibre bending, is similar in strength to the gravitational restoring force. Further details of the tilt resonance are discussed in Section 3.4.4.

3.3 Coordinate system

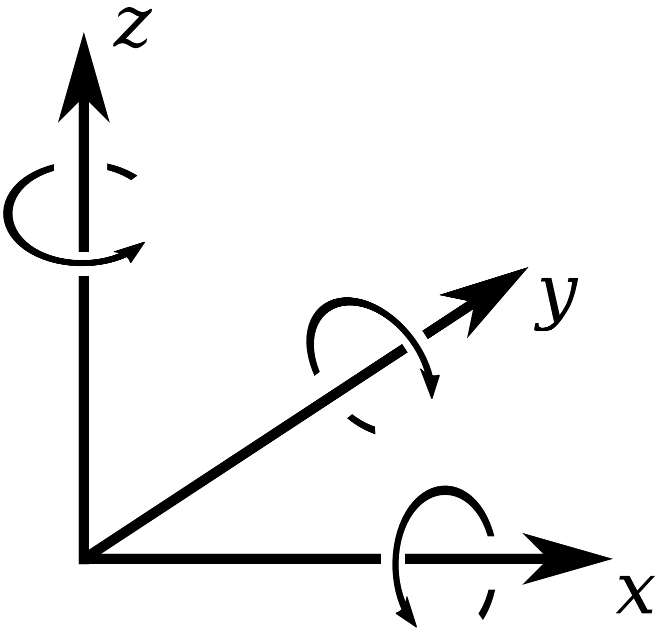

Figure 3.3: Visualisation of the coordinate system used throughout this thesis.

It is crucial to define a suitable coordinate system to describe the dynamics of the proof mass. We chose a right handed Cartesian coordinate system as indicated in Figure 3.3. For the components of interest in the Lagrangian, two vectors can be defined,

$$\vec{X_i} = (x_i, y_i, z_i), \qquad \vec{\theta_i} = (\gamma_i, \beta_i, \alpha_i), \tag{3.4}$$

where $\vec{X_i}$ represents the centre of mass positions, and $\vec{\theta_i}$ being their orientations, where β, γ, α are rotations about the x, y, and z axes respectively. The subscript i denotes the 3 coordinates of interest - $i \in \{m, w, s\}$, where m, w, s correspond to the mass, wire, and suspension point respectively.

Rotations are further defined using the standard Euler rotation matrices, where $\mathbf{R_x}, \mathbf{R_y}$, and $\mathbf{R_z}$ represent the rotation matrices about the corresponding axes,

$$\begin{aligned}
\mathbf{R_x}(\gamma) &= \begin{bmatrix} 1 & 0 & 0 \\ 0 & \cos(\gamma) & -\sin(\gamma) \\ 0 & \sin(\gamma) & \cos(\gamma) \end{bmatrix}, \\
\mathbf{R_y}(\beta) &= \begin{bmatrix} \cos(\beta) & 0 & \sin(\beta) \\ 0 & 1 & 0 \\ -\sin(\beta) & 0 & \cos(\beta) \end{bmatrix}, \\
\mathbf{R_z}(\alpha) &= \begin{bmatrix} \cos(\alpha) & -\sin(\alpha) & 0 \\ \sin(\alpha) & \cos(\alpha) & 0 \\ 0 & 0 & 1 \end{bmatrix},
\end{aligned} \tag{3.5}$$

therefore the complete rotation $\mathbf{R}$ is defined as

$$\mathbf{R} = \mathbf{R_z}(\alpha)\mathbf{R_y}(\beta)\mathbf{R_x}(\gamma) \tag{3.6}$$

3.4 The Lagrangian Model

In this section, the complete Lagrangian of the system is outlined. This is solved using Wolfram Mathematica [89] analytically with some numerical substitutions to improve the calculation speed. Results from the model are transfer functions describing the dynamics of the 6D seismometer, which are then analysed using MATLAB [90]. Analysis is conducted in the frequency domain which provides a more intuitive understanding of the system's behaviour. We can define a conversion from the time domain to the frequency domain, where for every time derivative a factor of $i\omega$ arises such that $\dot{A}(t) \to (i\omega)\tilde{A}(\omega)$ - analogous to the Fourier transform.

The Lagrangian contains input driving terms of the position and orientation of the suspension point, $\vec{X}_s$ and $\vec{\theta}_s$. The system has six generalised coordinates, q which define the position and orientation of the mass relative to the input driving terms: $q \in \{\gamma_m, \beta_m, \alpha_m, \gamma_w, \beta_w, \Delta L_w\}$, where ΔL_w is the extension of the wire.

Although the system dynamics are determined through the generalised coordinates, q, we are interested in the lab coordinates and orientation of the mass, which under the small angle approximation, are related to the generalised coordinates as,

$$\begin{aligned}
x_m &= x_s - L_{bend}\beta_s - L_w\beta_w - d\beta_m, \\
y_m &= y_s - L_{bend}\gamma_s - L_w\gamma_w - d\gamma_m, \\
z_m &= z_s - L_w - \Delta L_w, \\
\gamma_m &= \gamma_m, \\
\beta_m &= \beta_m, \\
\alpha_m &= \alpha_m.
\end{aligned} \tag{3.7}$$

The small angle approximations are defined as,

$$\begin{aligned}
\sin(\theta) &\approx \theta, \\
\cos(\theta) &\approx 1 - \frac{\theta^2}{2}, \\
\tan(\theta) &\approx \theta.
\end{aligned} \tag{3.8}$$

For the complete Lagrangian they are used once the full equations of motions are defined. However for the simplified cases discussed in Section 3.4.2, Section 3.4.3, and Section 3.4.4, the small angle approximations are used when constructing the Lagrangian. It was found that this did not exclude any of the key physics, such that the same key results were returned when simplifications were made for the equations of motion rather than the initial Lagrangian.

A simplified schematic is shown in Figure 3.4 which demonstrates the coordinate system used to describe the system.

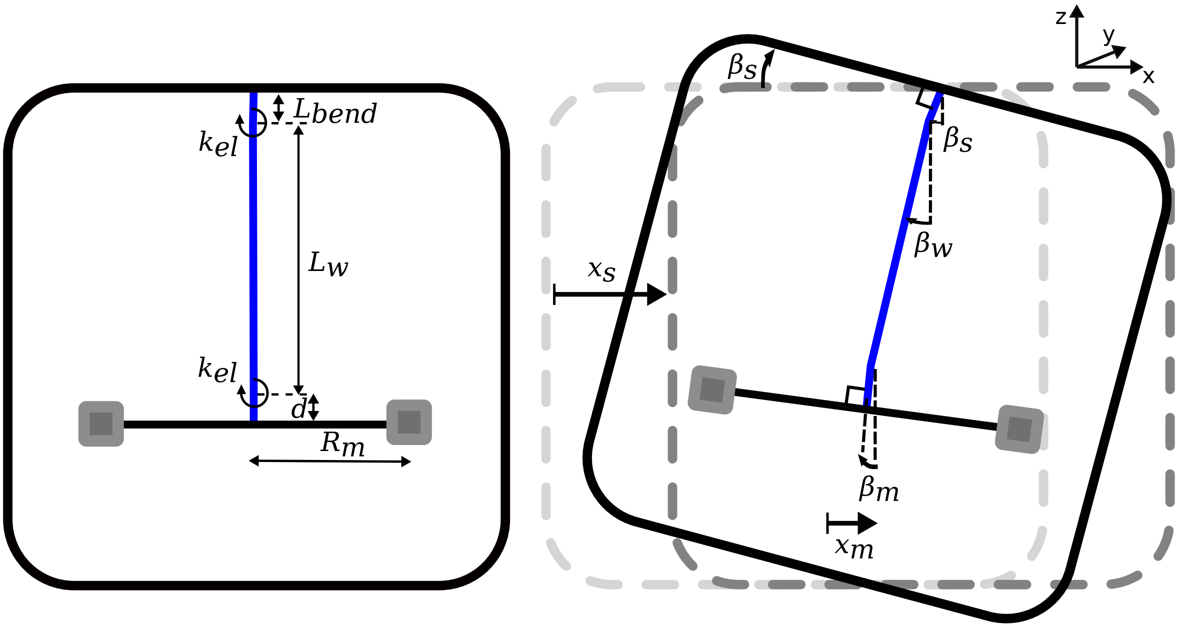

FIGURE 3.4: A simplified schematic of the 6D system showing the main coordinates of interest for the coupled case discussed in Section 3.4.4. Note that the angles have been exaggerated for clarity.

3.4.1 Full Lagrangian

The total Lagrangian, $\mathcal{L}_{\text{tot}}$ is defined as

$$\mathcal{L}_{\text{tot}} = \mathcal{T} - \mathcal{V}, \tag{3.9}$$

where $\mathcal{T}$ is the total kinetic energy and $\mathcal{V}$ is the total potential energy of the system. The kinetic energy consists of the translational and rotational energies of the mass and the suspension wire which can be expressed as

$$\begin{aligned}\mathcal{T} &= \mathcal{L}_{\text{LinearMass}} + \mathcal{L}_{\text{LinearWire}} + \mathcal{L}_{\text{RotationalMass}} + \mathcal{L}_{\text{RotationalWire}} \\ &= \sum_{i}^{m,w} \sum_{j}^{x,y,z} \left[\frac{1}{2} M_i \dot{X}_{ij}^2\right] + \sum_{i}^{m,w} \sum_{j}^{x,y,z} \left[\frac{1}{2} I_{ij} \dot{\theta}_{ij}^2\right],\end{aligned} \tag{3.10}$$

where $\vec{I_{ij}} = (I_{ix}, I_{iy}, I_{iz})$. The subscript i denotes the object of interest, and j cycles through the coordinates (x, y, z). The potential energy of the system consists of the linear spring potential due to the wire extension, the bending potential at the top and bottom of the wire, torsional potential of the wire, and the gravitational potential energy of the mass and wire,

$$\begin{aligned}\mathcal{V} &= \mathcal{L}_{\text{LinearSpring}} + \mathcal{L}_{\text{ElasticBending}} + \mathcal{L}_{\text{Torsion}} + \mathcal{L}_{\text{Gravitaitonal}} \\ &= \frac{1}{2}k_z(\Delta L_w)^2 + \sum_i^{\gamma,\beta}\left[\frac{1}{2}k_{el}\left[(i_s - i_w)^2 + (i_m - i_w)^2\right]\right] \\ &\quad + \frac{1}{2}k_{tor}(\alpha_m - \alpha_s)^2 + \sum_i^{m,w}\left[M_i g z_i\right].\end{aligned} \tag{3.11}$$

Using the Euler-Lagrange equations for each of the dynamic coordinates, q,

$$\frac{\mathrm{d}}{\mathrm{d}t}\left(\frac{\partial\mathcal{L}_{\text{tot}}}{\partial\dot{q}}\right) - \frac{\partial\mathcal{L}_{\text{tot}}}{\partial q} = 0. \tag{3.12}$$

Note that α_w is obsolete, as the torsional change across the length of the wire is constrained by the orientation of the suspension point and test mass, α_s and α_m respectively.

A variety of forces and torques can be applied to the system. We can first consider some generic forces acting through the centre of mass of the system in the three translational coordinates, x, y, and z - F_{mx}, F_{my}, F_{mz} which do work on the system, such that $\delta W_{Fm} = F_{mx}\delta x_m + F_{my}\delta y_m + F_{mz}\delta z_m$, where $\delta x_m, \delta y_m, \delta z_m$ are expressed in terms of the generalised coordinates. Next we can consider the torsional work acting on the system, where a torque on each of the angular generalised coordinates occurs, such that the work done by the torques $\delta W_T = T_{\gamma_m}\delta\gamma_m + T_{\beta_m}\delta\beta_m + T_{\alpha_m}\delta\alpha_m + T_{\gamma_w}\delta\gamma_w + T_{\beta_w}\delta\beta_w$.

Finally, actuation on the test mass is achieved via the Birmingham Optical Sensors and Electromagnetic Motors (BOSEMs), these devices are also used as a secondary sensor. The BOSEMs are paired as one horizontal, H, and one vertical, V, per arm of the reference mass, which are labelled as 1, 2, and 3. Therefore, we can label the magnet/flag position in terms of the dynamic coordinates as $\vec{X}_k = (x_k, y_k, z_k)$ where $k \in \{\mathrm{BV1}, \mathrm{BV2}, \mathrm{BV3}, \mathrm{BH1}, \mathrm{BH2}, \mathrm{BH3}\}$, with the forces from the BOSEMs as $\vec{F}_k = (F_{kx}, F_{ky}, F_{kz})$. The resultant work done by the BOSEMs becomes $\delta W_B = \sum_k \vec{F}_k \cdot \delta \vec{X}_k$.

The total work done by all forces is then $\delta W_{\text{tot}} = \delta W_{Fm} + \delta W_T + \delta W_B$.

These extra driving terms can be included in the equations of motion as external energy provided to the system,

$$\frac{\mathrm{d}}{\mathrm{d}t}\left(\frac{\partial \mathcal{L}_{\text{tot}}}{\partial \dot{q}}\right) - \frac{\partial \mathcal{L}_{\text{tot}}}{\partial q} = \frac{\partial W_{\text{tot}}}{\partial q}. \tag{3.13}$$

A large number of driving terms are included which cross couple to many degrees of freedom. The system is inherently complex and solving such a Lagrangian analytically is challenging. Further assumptions are made to simplify the system: (i) the test mass is suspended directly along the z-axis (aligned with gravity), through the centre of mass when in its equilibrium position, (ii) fibre symmetry is assumed, and (iii) a frequency independent loss angle - i.e damping is only due to frequency independent loss, ϕ.

Due to the above assumptions, the system can be deconstructed into a series of decoupled Lagrangian systems, ignoring the driving terms that are included in Equation (3.13). In the following sections the system is decoupled into the assumed detached Z, and RZ degrees of freedom. The X and RY (and corresponding Y and RX) degrees of freedom are inherently coupled due to the natural pendulum modes of the system. These must be solved simultaneously, however due to the assumed symmetry, the dynamics for X and RY are equivalent to that of Y and RX.

3.4.2 Vertical Degree of Freedom

The Lagrangian for the Z motion of the mass is that of a mass on a spring where the extension of the fibre acts as the spring constant,

$$\mathcal{L}_Z = \frac{1}{2} M_m \dot{z_m}^2 - \left[\frac{1}{2} k_z (z_s - z_m)^2 + M_m g z_m \right], \tag{3.14}$$

where z_m is the position of the mass around its equilibrium point once the wire is under tension, and z_s is the position of the suspension point about its equilibrium position. The spring constant k_z is calculated using the properties of the fibre shown in Section 3.2. Using the Euler-Lagrange equation, the equation of motion for the Z degree of freedom can be obtained.

$$\frac{\mathrm{d}}{\mathrm{d}t} \left(\frac{\partial \mathcal{L}_Z}{\partial \dot{z_m}} \right) - \frac{\partial \mathcal{L}_Z}{\partial z_m} = F_{mz}, \tag{3.15}$$

here, F_{mz} is an arbitrary force acting through the centre of mass of the system. The resulting equation of motion is

$$M_m \ddot{z}_m - k_z z_s + k_z z_m + M_m g = F_{mz}. \tag{3.16}$$

The behaviour of the system can be understood by observing the transfer function for the input driving terms. Converting the system into the frequency domain, Equation (3.16) reads as,

$$-M_m \omega^2 \tilde{z}_m - k_z \tilde{z}_s + k_z \tilde{z}_m + M_m g \delta_\omega(0) = \tilde{F}_{mz}, \tag{3.17}$$

where $\delta_\omega(0)$ is a Dirac delta function at zero frequency. As the frequency dependent motion of the mass is insensitive to a DC offset, this term can be ignored. From this, it is simple to obtain the transfer function of the input drives $\tilde{z}_s$ and $\tilde{F}_{mz}$ into the motion of the mass. However, the measurement that would be made is the difference between the measurement platform and the mass, $\Delta\tilde{z} = \tilde{z}_s - \tilde{z}_m$, therefore,

$$(k_z - M_m\omega^2)\Delta\tilde{z} = -M_m\omega^2\tilde{z}_s + \tilde{F}_{mz}. \tag{3.18}$$

The resulting transfer functions are,

$$\frac{\Delta\tilde{z}}{\tilde{z}_s} = \frac{-M_m\omega^2}{k_z - M_m\omega^2}, \qquad \frac{\Delta\tilde{z}}{\tilde{F}_{mz}} = \frac{1}{k_z - M_m\omega^2}, \tag{3.19}$$

which recovers the inertial sensor response discussed in Section 2.2. Note that the spring constant is complex as defined in Section 3.2, therefore the Q of the system is not infinite and the system has some inherent damping due to the loss angle of the fibre.

The plots for the corresponding transfer functions are shown in Figure 3.5

3.4.3 Torsional Degree of Freedom

The RZ motion of the mass is due to the angular restoring torque of the fibre. Similarly with the case for the vertical mode, this is due to the properties of the fibre, where the restoring force k_{tor} is defined in Equation (3.2). The Lagrangian - under the small angle approximation - for the torsional mode is,

$$\mathcal{L}_{RZ} = \frac{1}{2}I_z\dot{\alpha}_m^2 - \frac{1}{2}k_{tor}(\alpha_s - \alpha_m)^2. \tag{3.20}$$

The Euler-Lagrange equation for the system is

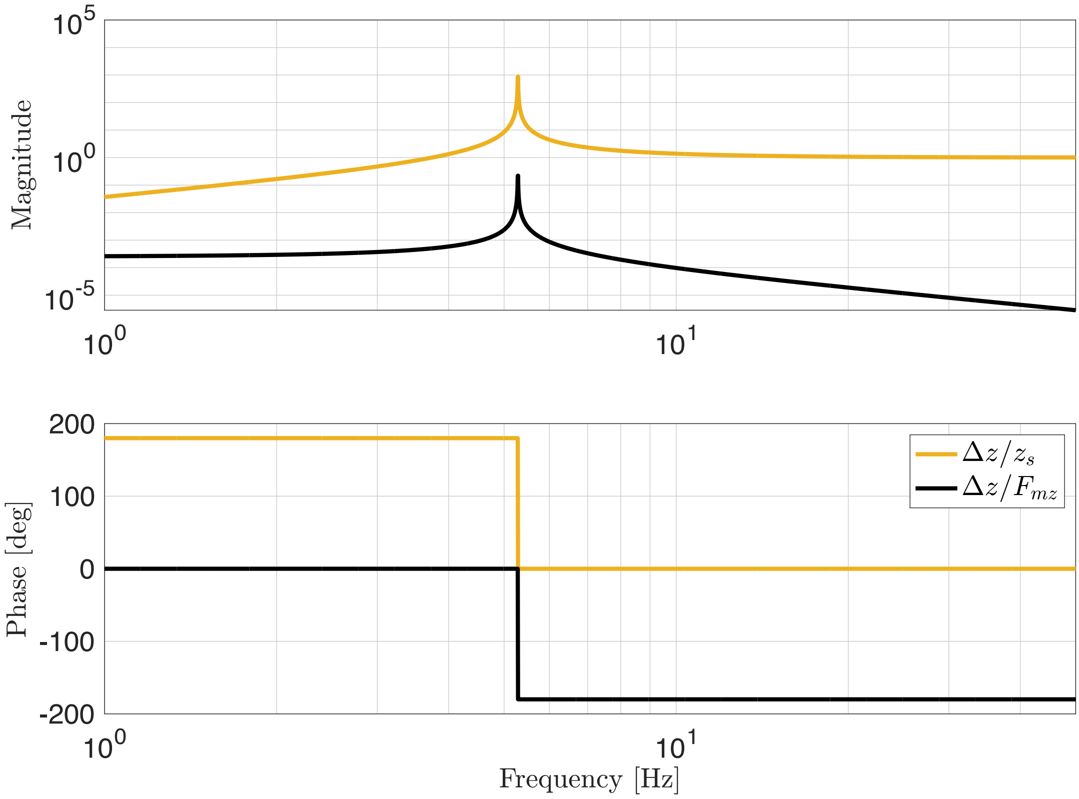

FIGURE 3.5: Transfer functions for the Z degree of freedom showing the sensor response (yellow) and the response to an arbitrary force through the centre of mass (black).

$$\frac{\mathrm{d}}{\mathrm{dt}}\left(\frac{\partial \mathcal{L}_{RZ}}{\partial \dot{\alpha}_m}\right) - \frac{\partial \mathcal{L}_{RZ}}{\partial \alpha_m} = T_{\alpha m}, \tag{3.21}$$

where $T_{\alpha m}$ is the torque acting through the pivot point of the mass resulting in the equation of motion,

$$I_z \ddot{\alpha}_m - k_{tor}\alpha_s + k_{tor}\alpha_m = T_{\alpha m}. \tag{3.22}$$

Following the same method used in Section 3.4.2, the resulting transfer functions for the inputs into the measured signal, $\Delta\tilde{\alpha} = (\tilde{\alpha}_s - \tilde{\alpha}_m)$, are

$$\frac{\Delta\tilde{\alpha}}{\tilde{z}_s} = \frac{-I_z\omega^2}{k_{tor} - I_z\omega^2}, \qquad \frac{\Delta\tilde{\alpha}}{\tilde{T}_{\alpha m}} = \frac{1}{k_{tor} - I_z\omega^2}. \tag{3.23}$$

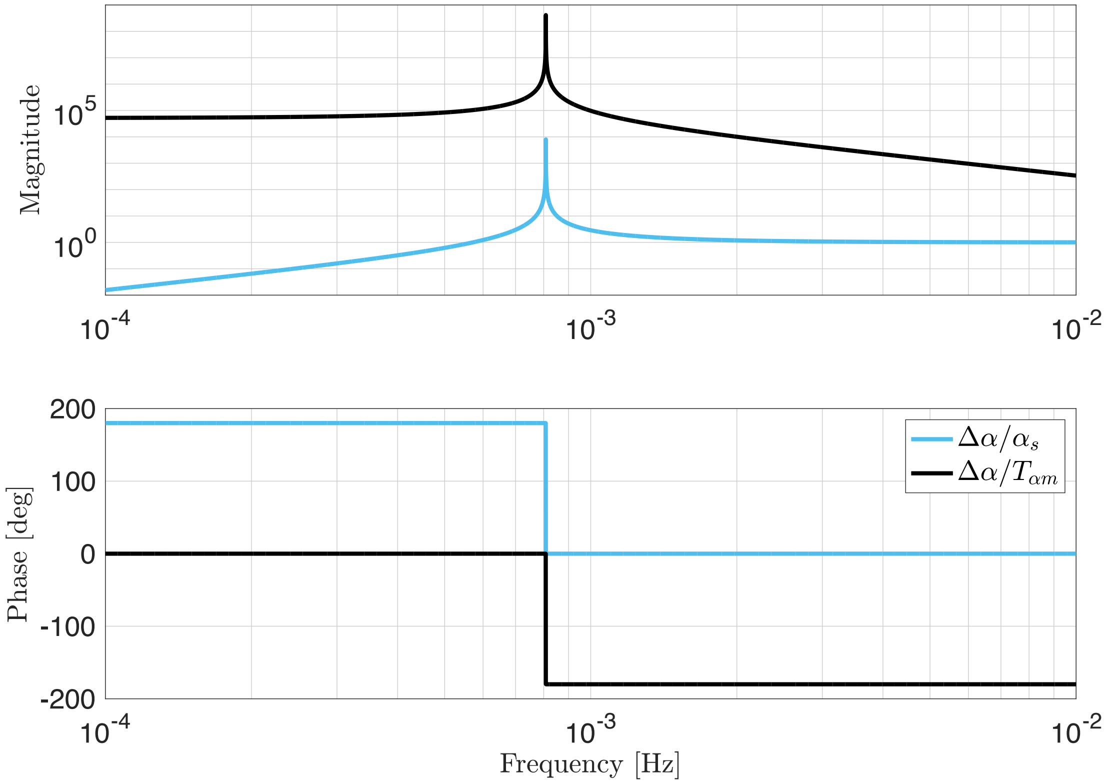

FIGURE 3.6: Transfer functions for the RZ degree of freedom showing the sensor response (cyan) and the response to an arbitrary torque acting on the mass (black). Note that the magnitude at DC for the torque transfer function is large, meaning that the mass is more susceptible to motion from small inputs such as noise sources.

3.4.4 The Coupled Degrees of Freedom

The dynamics for the coupled case are symmetric for the X, RY case and the Y, RX case. The derivation presented here focuses on the X and RY degrees of freedom (i) under the small angle approximation and (ii) neglecting the mass and moment of inertia of the wire. Analysing the schematic in Figure 3.4, the Lagrangian can be determined as,

$$\begin{aligned}\mathcal{L}_{XRY} \approx & \frac{1}{2}M_m L_{bend}^2 \dot{\beta}_s^2 + \frac{1}{2}M_m L_w^2 \dot{\beta}_w^2 + \frac{1}{2}(I_y + M_m d^2)\dot{\beta}_m^2 \\ & + M_m L_{bend} L_w \dot{\beta}_s \dot{\beta}_w + M_m L_{bend} d \dot{\beta}_s \dot{\beta}_m + M_m L_w d \dot{\beta}_w \dot{\beta}_m \\ & - \frac{1}{2}M_m g L_{bend} \beta_s^2 - \frac{1}{2}M_m g L_w \beta_w^2 - \frac{1}{2}M_m g d \beta_m^2 \\ & - \frac{1}{2}k_{el}\beta_s^2 - k_{el}\beta_w^2 - \frac{1}{2}k_{el}\beta_m^2 + k_{el}\beta_s\beta_w + k_{el}\beta_w\beta_m.\end{aligned} \tag{3.24}$$

Equation (3.24) does not include any input translation in the X degree of freedom to the system. This can be included as a work done to the system through a torque applied from the suspension point, $\delta W_x = F_s(L_{bend}\delta\beta_s + L_w\delta\beta_w + d\delta\beta_m)$. Here, $F_s = M_m\ddot{x}_s$, is a force acting in the x direction. The resulting Euler-Lagrange equations are,

$$\begin{aligned}\frac{\mathrm{d}}{\mathrm{dt}}\left(\frac{\partial\mathcal{L}}{\partial\dot{\beta}_w}\right) - \frac{\partial\mathcal{L}}{\partial\beta_w} = \frac{\partial W_x}{\partial\beta_w}, \\ \frac{\mathrm{d}}{\mathrm{dt}}\left(\frac{\partial\mathcal{L}}{\partial\dot{\beta}_m}\right) - \frac{\partial\mathcal{L}}{\partial\beta_m} = \frac{\partial W_x}{\partial\beta_m},\end{aligned} \tag{3.25}$$

yielding the equations of motion,

$$\begin{aligned}& M_m L_{bend} L_w \ddot{\beta}_s + M_m L_w^2 \ddot{\beta}_w + M_m L_w d \ddot{\beta}_m + M_m g L_w \beta_w + 2k_{el}\beta_w - k_{el}\beta_s - k_{el}\beta_m = M_m \ddot{x}_s L_w, \\ & M_m L_{bend} d \ddot{\beta}_s + M_m L_w d \ddot{\beta}_w + (M_m d^2 + I_y)\ddot{\beta}_m + M_m g d \beta_m + k_{el}\beta_m - k_{el}\beta_w = M_m \ddot{x}_s d.\end{aligned} \tag{3.26}$$

In the frequency domain,

$$\tilde{\beta}_w = \frac{(k_{el} + M_m L_w d\omega^2)\tilde{\beta}_m - M_m L_w \omega^2 \tilde{x}_s + (k_{el} + M_m L_{bend} L_w \omega^2)\tilde{\beta}_s}{M_m g L_w + 2k_{el} - M_m \omega^2 L_w^2}, \tag{3.27}$$

$$\tilde{\beta}_m = \frac{(k_{el} + M_m L_w d\omega^2)\tilde{\beta}_w - M_m d\omega^2 \tilde{x}_s + M_m L_{bend} d\omega^2 \tilde{\beta}_s}{M_m g d + k_{el} - (M_m d^2 + I_y)\omega^2}. \tag{3.28}$$

The equations can be solved simultaneously to get independent equations for $\tilde{\beta}_w$ and $\tilde{\beta}_m$ which can be used to determine the transfer functions of the X and RY degrees of freedom.

The key result from this algebraic manipulation is to understand the tunability of the tilt resonance of the system. From Equation (3.27) and Equation (3.28), the resonant frequencies for the translational and tilt modes respectively are,

$$\omega_{\mathrm{X}}^2 \approx \frac{M_m g L_w + 2k_{el}}{M_m L_w^2}, \qquad \omega_{\mathrm{RY}}^2 \approx \frac{M_m g d + k_{el}}{M_m d^2 + I_y}. \tag{3.29}$$

For the translational resonance, the system is in the regime where $mgL_w \gg k_{el}$ such that the resonance is dominated by the gravitational restoring force. This is the case for a simple pendulum supporting a point mass with resonance $\omega_{\mathrm{X}}^2 = g/L_w$. The tilt resonance is more complex and can be tuned by altering the centre of mass position relative to the bending point of the wire, d. In the case of the 6D system, $I_y \gg md^2$, therefore, the tunability of the resonance can be simplified such that $\omega_{\mathrm{RY}}^2 \propto d$. The relationship between the offset, d and the resonant frequency, $f_{\mathrm{RX,RY}}$ is shown in Figure 3.7. Tuning of the centre of mass position would be achieved during the installation and tests of the device, where small masses or screws would be raised or lowered to change the gravitational contribution of the stiffness.

If we consider the case where the centre of mass position is not altered, $d = L_{bend}$,

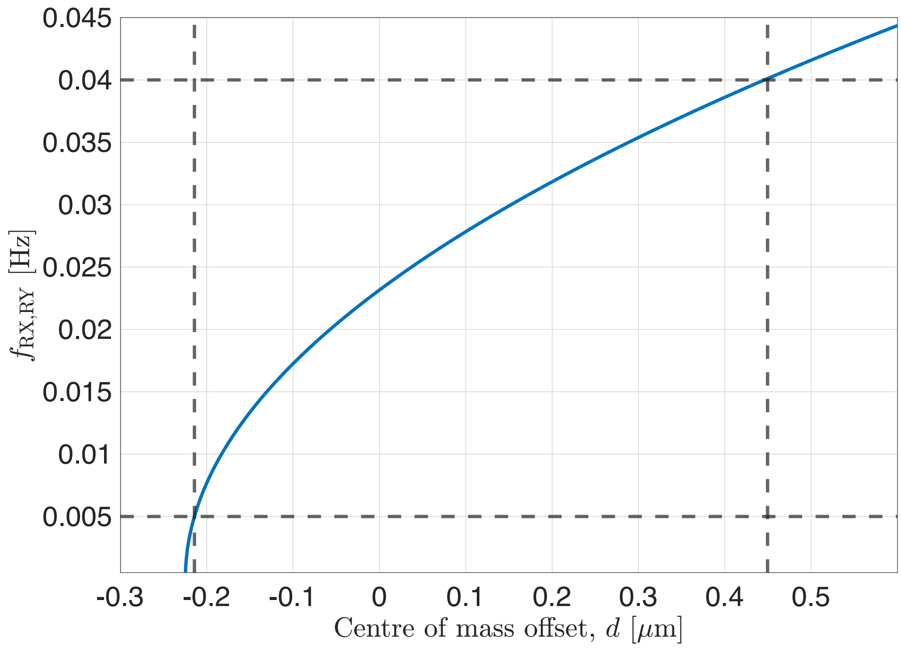

FIGURE 3.7: Plot of the tilt resonant frequency against the centre of mass offset, d. The left vertical line indicates the centre of mass position above the apparent bending point of the wire, creating an inverted pendulum resulting in a lower tilt resonance of 5 mHz. The vertical line on the right hand side shows the natural tilt resonance if no tuning is present.

the tilt resonance of the system would be $f_{\mathrm{RY}} = 40\,\mathrm{mHz}$, however by raising the centre of mass position above the bending point, we find the resonant frequency becomes $f_{\mathrm{RY}} = 5\,\mathrm{mHz}$.

Solving Equation (3.27) and Equation (3.28) for $\tilde{\beta}_w$ and $\tilde{\beta}_m$, we can determine the transfer functions of the system by transforming the coordinate system from the dynamic coordinates back into the lab frame using Equation (3.7). In doing so, we can determine four transfer functions, using two inputs, $\tilde{x}_s$ and $\tilde{\beta}_s$, and two outputs, $\Delta\tilde{x} = \tilde{x}_s - \tilde{x}_m$ and $\Delta\tilde{\beta} = \tilde{\beta}_s - \tilde{\beta}_m$.

Note that the denominator for all four transfer functions (Equation (3.30) to Equation (3.33)) have the same denominator which represent the two resonant frequencies of the system, ω_{X} and ω_{RY}. The extra term on the denominator $(k_{el} + M_m L_w d\omega^2)^2$ is the cross coupling term between the two degrees of freedom. This would cause a shift in the resonant frequencies, however due to the large separation between the translation and tilt resonance, this effect is negligible and does not alter the approximations of the resonances in Equation (3.29).

Below are the transfer functions into the X degree of freedom readout, shown in Figure 3.8 ,

$$\begin{aligned}\frac{\Delta\tilde{x}}{\tilde{x}_s} = T_{xx} &= \frac{-M_m\omega^2[k_{el}(L_w^2+2L_wd+2d^2)+M_mgd(L_w^2+dL_w)-L_w^2I_y\omega^2]}{\left(\begin{array}{r}(M_mgL_w+2k_{el}-M_m\omega^2L_w^2)(M_mgd+k_{el}-(M_md^2+I_y)\omega^2)\\ -(k_{el}+M_mL_wd\omega^2)^2\end{array}\right)}\\ &\approx \frac{-M_mL_w^2I_y(\omega_{\mathrm{RY}}^2-\omega^2)\omega^2}{M_mL_w^2I_y(\omega_{\mathrm{X}}^2-\omega^2)(\omega_{\mathrm{RY}}^2-\omega^2)} \approx \frac{-\omega^2}{(\omega_{\mathrm{X}}^2-\omega^2)}.\end{aligned} \tag{3.30}$$

We can make the assumption that $d \ll L_w$, and can therefore ignore terms of $\mathcal{O}(d^2)$ and higher. As an approximation, the extra cross coupling term in the denominator can also be neglected. This provides some intuitive understanding of the system, and we find that there are two zero terms in the system, the first at zero frequency, and the second at $\omega \approx \omega_{\mathrm{RY}}$ which cancels the resonance in the denominator. We find that we recover the inertial sensor response for a single degree of freedom system in Equation (3.30) which is shown by the approximation made. A similar approach is used for the other transfer functions.

$$\begin{aligned} \frac{\Delta\tilde{x}}{\tilde{\beta}_s} &= T_{\beta x} = (L_w + d) - \frac{\tilde{x}_m}{\tilde{\beta}_s} = (L_w + d) \\ &- \frac{\left(\begin{array}{l} -M_m L_{bend} L_w^2 I_y \omega^4 + k_{el}(M_m g L_w d + k_{el}(L_w + d)) \\ \quad + (k_{el}(M_m L_{bend}(L_w^2 + 2L_w d + 2d^2) - I_y L_w) + M_m^2 g L_{bend} L_w d (L_w + d))\omega^2 \end{array} \right)}{\left(\begin{array}{r} (M_m g L_w + 2k_{el} - M_m \omega^2 L_w^2)(M_m g d + k_{el} - (M_m d^2 + I_y)\omega^2) \\ - (k_{el} + M_m L_w d \omega^2)^2 \end{array} \right)} \\ &\approx (L_w + d) \end{aligned} \tag{3.31}$$

The translational motion of the mass due to the input tilt is minimal, and becomes inertial above the translational resonance. However, at low frequencies, the mass has a flat response to the input motion, which is suppressed by the pendulum length and the minimal elastic restoring forces at the top and bottom of the wire. Translational motion due to the input tilt has a DC magnitude of $\tilde{x}_m/\tilde{\beta}_s \approx \frac{k_{el}}{M_m L_w \omega_{\mathrm{X}}^2} \ll 1$. The transfer function of the tilt to translational sensor is dominated by the change of the sensor position due the rotation. This is given by the extra $(L_w + d)$ term in the transfer function.

The following transfer functions are for the tilt readout which are shown in Figure 3.9. To obtain the sensor displacement measurement, they have to be multiplied by the lever arm over which the measurement is made.

$$\begin{aligned} \frac{\Delta\tilde{\beta}}{\tilde{x}_s} &= \frac{\tilde{\beta}_m}{\tilde{x}_s} = T_{x\beta} \\ &= \frac{M_m \omega^2 [k_{el}(L_w + 2d) + M_m g L_w d]}{\left(\begin{array}{r} (M_m g L_w + 2k_{el} - M_m \omega^2 L_w^2)(M_m g d + k_{el} - (M_m d^2 + I_y)\omega^2) \\ - (k_{el} + M_m L_w d \omega^2)^2 \end{array} \right)} \\ &\approx \frac{M_m L_w I_y \omega_{\mathrm{RY}}^2 \omega^2}{M_m L_w^2 I_y (\omega_{\mathrm{X}}^2 - \omega^2)(\omega_{\mathrm{RY}}^2 - \omega^2)} \approx \frac{\omega_{\mathrm{RY}}^2 \omega^2}{L_w (\omega_{\mathrm{X}}^2 - \omega^2)(\omega_{\mathrm{RY}}^2 - \omega^2)}. \end{aligned} \tag{3.32}$$

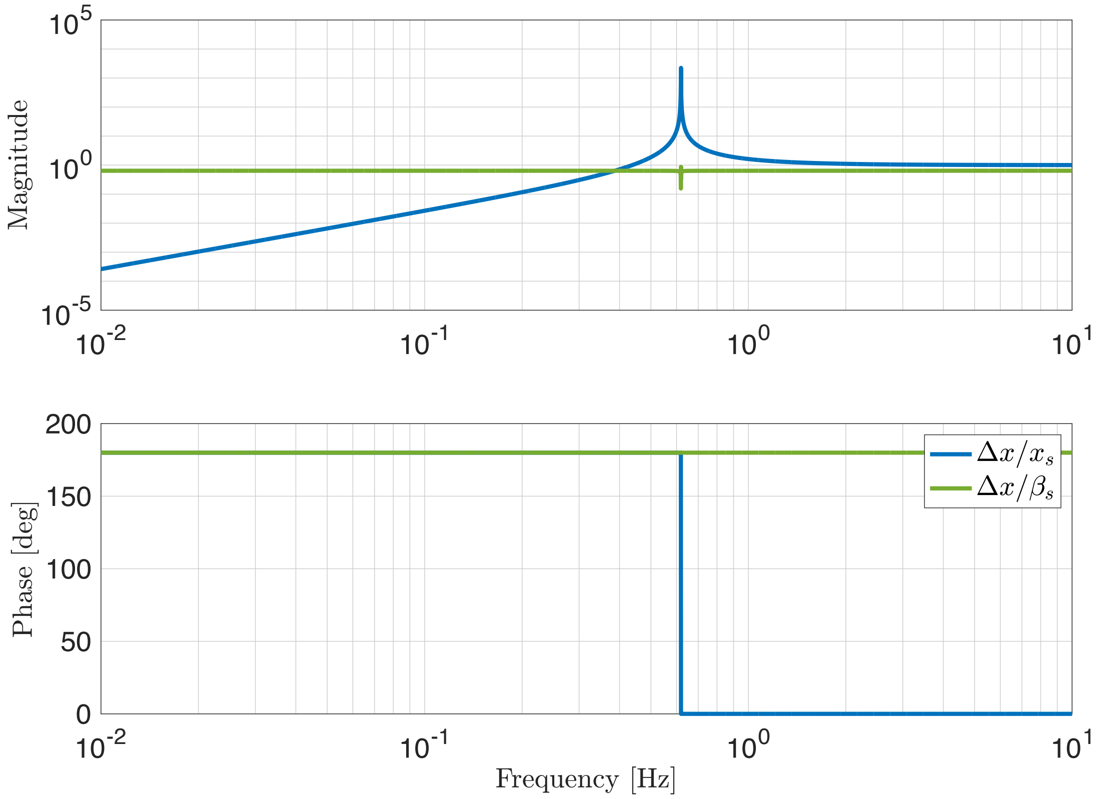

FIGURE 3.8: Transfer functions of the translational and tilt motion into the translational readout. For the input ground translation, we recover the inertial sensor response as expected. The tilt input tilt motion. β_s results in a flat transfer function in the readout scheme due to the geometry of the system, with a magnitude equal to the fibre length.

Equation (3.32) shows the translation to tilt transfer function which contains a null at zero frequency and two resonances for the tilt and translational modes. Suppression of this cross coupling is achieved by the frequency separation of the two eigenmodes, where between the resonances the magnitude can be approximated as $\frac{\omega_{\mathrm{RY}}^2}{L_w \omega_{\mathrm{X}}^2}$.

$$\begin{aligned}\frac{\Delta\tilde{\beta}}{\tilde{\beta}_s} &= 1 - \frac{\tilde{\beta}_m}{\tilde{\beta}_s} = T_{\beta\beta} \\ &= 1 - \frac{k_{el}^2 + [k_{el}(M_m L_w d + M_m L_{bend} L_w + 2M_m L_{bend} d) + M_m^2 g L_{bend} L_w d]\omega^2}{\begin{aligned}(M_m g L_w + 2k_{el} - M_m\omega^2 L_w^2)(M_m g d + k_{el} - (M_m d^2 + I_y)\omega^2) \\ - (k_{el} + M_m L_w d\omega^2)^2\end{aligned}} \\ &\approx 1.\end{aligned} \tag{3.33}$$

Tilt to tilt motion is minimal due to the weak elastic restoring forces of the fibre. Above the tilt resonance the mass becomes inertial to the input tilt motion, however the sensor detects motion which is dominated by the platform tilt, as at DC, the magnitude of $\tilde{\beta}_m/\tilde{\beta}_s \approx \frac{k_{el}^2}{M_m L_w^2 I_y \omega_{\mathrm{X}}^2 \omega_{\mathrm{RY}}^2} \ll 1$.

Figure 3.9 shows the natural decoupling of the translational and tilt dynamics due to the separation of their resonant modes. This is seen through the low magnitude of the $\Delta\tilde{\beta}_s/\tilde{x}_s$ transfer function. Separation of the resonant frequencies causes the tilt of the proof mass to become inertial at lower frequencies than the translational mode.

The translational input motion would cause bending in the wire, and due to the restoring force would cause the mass to tilt. Above the resonance this effect is minimised and is further suppressed by the inertia of the mass above the translational mode.

Unfortunately, as expected, the minimisation of the coupling due to the frequency splitting of the modes is not seen in the translational readout, demonstrated by the $\Delta\tilde{x}/\tilde{\beta}_s$ transfer function in Figure 3.8. The coupling of the tilt motion into the readout is dominated by the geometry of the system, analogous to the tilt-to-horizontal coupling discussed in Section 2.2. The translational motion of the mass is minimal due to the weak restoring forces from the wire bending, k_{el}. However the sensors change position due to the input tilt - this can be visualised from Figure 3.4 - which results in the flat

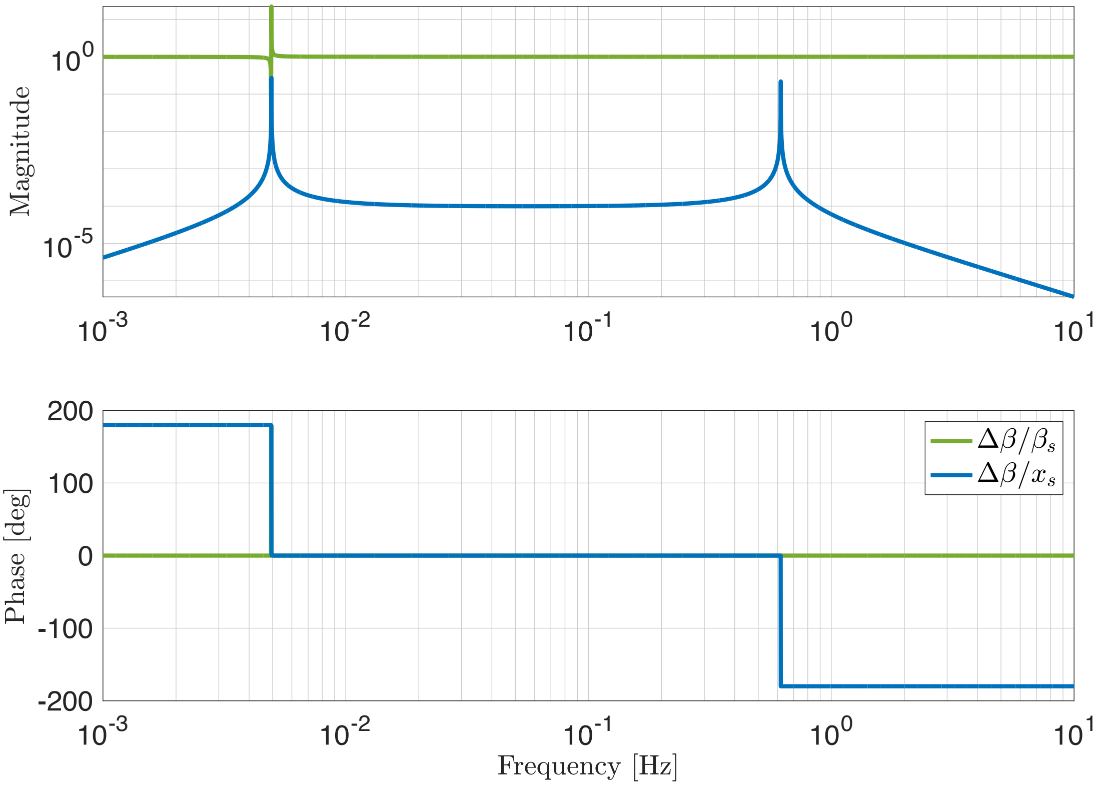

FIGURE 3.9: Transfer functions for the tilt degree of freedom. The tilt to tilt transfer function does not recover the inertial sensor response. The translational induced tilt motion is minimal due to the large separation of the translational and tilt resonances.

frequency response.

The measured motion for the X and RY degrees of freedom can be represented via the 2x2 matrix,

$$\begin{pmatrix} \Delta\tilde{x}_s \\ \Delta\beta_s \end{pmatrix} = \begin{pmatrix} T_{xx} & T_{\beta x} \\ T_{x\beta} & T_{\beta\beta} \end{pmatrix} \begin{pmatrix} x_s \\ \beta_s \end{pmatrix}. \tag{3.34}$$

The transfer functions in Equation (3.34) represent the dynamics of the system assuming no further cross couplings. In order to recover the actual input motion to the system, these transfer functions must be modelled correctly in order to invert the transfer function matrix.

In reality, extra cross couplings from all degrees of freedom are likely to occur, therefore a 6x6 matrix of transfer functions to describe the plant of the system is needed. This would be achieved by measuring the transfer functions of the system, as creating an analytical model of these couplings would be extremely difficult.

3.4.5 Model Predictions

The full Lagrangian model predicts the dynamics, and allows us to budget the noise of the 6D system. As previously mentioned in Section 3.4.1, symmetry assumptions have been made to simplify the system and study the idealised case. The actuation noise from the BOSEMs can be propagated through the model to determine the noise, including the readout noises. Due to the separation of the resonances, the thermal noises from the tilt and translational modes can be treated independently, as if they were decoupled single degree of freedom systems as discussed in [48] using the fluctuation-dissipation theorem [91].

In this section we analyse the theoretical noises of 6D by propagating them through the results of the Lagrangian model. A simplified block diagram shown in Figure 3.10 indicates the points of noise injection, where $\vec{n}_D$ is the noise from the BOSEM damping due to the digital to analogue converter (DAC), and $\vec{n}_r$ is the readout noise, which can be either from the HoQIs or the analogue to digital converter (ADC). Note that the P and D blocks represent all degrees of freedom, where P is the plant of the 6D system which can be represented by a frequency dependent 6x6 matrix using the transfer functions described above, and D encompasses the 6x6 plant inversion which involves decoupling the degrees of freedom, the control filters, and actuation. However for damping of the mass, we can assume that each degree of freedom is independent, thus simplifying the system into six single feedback loops, as damping is only required to reduce the high Q resonances of the system.

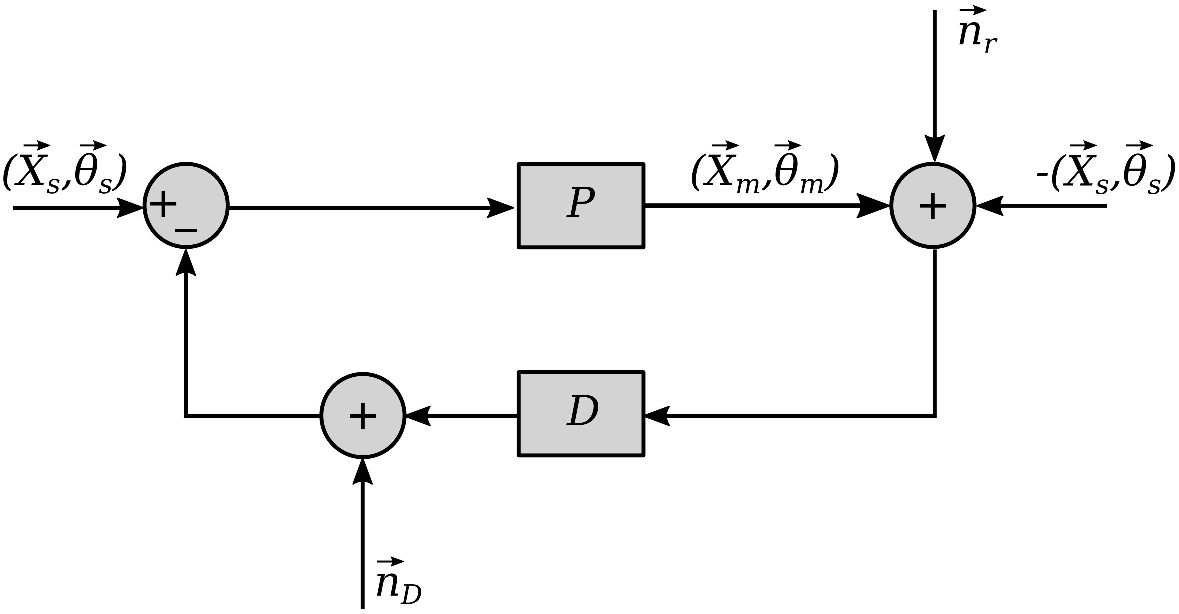
$\vec{n}_r$
$(\vec{X}_s,\vec{\theta}_s)$
+
−
P
$(\vec{X}_m,\vec{\theta}_m)$
+
$-(\vec{X}_s,\vec{\theta}_s)$
+
D
$\vec{n}_D$

FIGURE 3.10: Block diagram showing the damping scheme for the test mass and the points of noise injection. Thermal noise injection has been omitted.

From Figure 3.10, the resultant mass motion can be determined,

$$\begin{aligned}(\vec{X}_m,\vec{\theta}_m) &= P((\vec{X}_s,\vec{\theta}_s)-\vec{n}_D)-PD((\vec{X}_m,\vec{\theta}_m)-(\vec{X}_s,\vec{\theta}_s)+\vec{n}_r)\\ \implies (1+PD)(\vec{X}_m,\vec{\theta}_m) &= P(1+D)(\vec{X}_s,\vec{\theta}_s)-P\vec{n}_D+PD\vec{n}_r \\ \therefore (\vec{X}_m,\vec{\theta}_m) &= \frac{P+PD}{1+PD}(\vec{X}_s,\vec{\theta}_s)+\frac{-P}{1+PD}\vec{n}_D+\frac{PD}{1+PD}\vec{n}_r,\end{aligned} \tag{3.35}$$

To calculate the noise from the actuators, we set $D=0$ such that only the DAC noise $\vec{n}_D$ propagates, and not a control signal. In this case, $(\vec{X}_m,\vec{\theta}_m)\propto P\vec{n}_D$. With no damping, the readout noise does not affect the motion of the mass as it is not injected back through the actuators, however it is always present in the readout. The input motion ($\vec{X}_s, \vec{\theta}_s$) couples to the mass motion and displaces the sensors through the transfer functions described in Section 3.4.1 - this is the noise we wish to suppress.

The BOSEM actuation noise due to the DAC for the vertical and horizontal actuators differ due to the required actuation strength in each degree of freedom. The requirement is dominated by mitigations of drift motion in the angular modes, requiring DC position adjustment of the mass relative to the platform. The DC force required, F_{DC}, is

$$F_{\mathrm{DC}} = \frac{I\omega_0^2}{L_D}\theta_{\mathrm{DC}}, \tag{3.36}$$

where I and ω_0 are the moment of inertia and angular resonant frequency for the degree of freedom of interest, L_D is the distance at which the actuation occurs from the pivot, and θ_{DC} is the DC angle change required. An overestimation of the force is made by assuming that a single actuator can provide the necessary correction to the mass position. Stiffness of the tilt and torsional modes differ, hence the force needed differs for the horizontal actuators (RZ) and the vertical actuators (RX,RY).

A force of $1\,\mu$N would result in a 1 mrad of adjustment in the tilt degrees of freedom, whereas $0.054\,\mu$N is required for the same displacement in RZ. We assume that 1 mrad of position tuning is needed for the tilt modes, and 10 mrad for RZ, which sets the limit on the noise from the DAC. An estimation of the DAC noise is shown in Figure 3.11.

The thermal noise is calculated via the Fluctuation-Dissipation theorem, where the resultant thermal noise displacement power spectrum for a single degree of freedom oscillator can be approximated as [91, 48]

$$x^2 \approx \frac{4k_bT\omega_{\mathrm{X}}^2\phi_{xeff}}{m\omega(\omega_{\mathrm{X}}^2-\omega^2)^2}, \qquad \theta^2 \approx \frac{4k_bT\omega_{\mathrm{RY}}^2\phi_{\theta eff}}{I\omega(\omega_{\mathrm{RY}}^2-\omega^2)^2}, \tag{3.37}$$

where $Q_x = 1/\phi_{xeff} \approx L_w/L_{bend}\phi$. The dilution factor $D_x = L_w/L_{bend}$, increasing

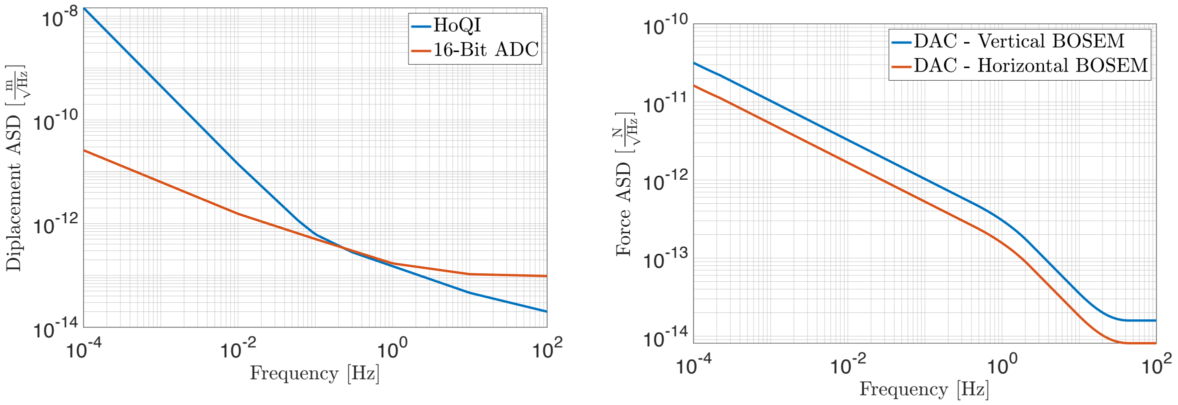

(A) Displacement sensitivity of the HoQI devices and the ADC using the LIGO SWG_sensor_noise.m and SEI_sensor_noise.m scripts respectively.

(B) Amplitude spectra of the BOSEM forces for the vertical and horizontal actuators assuming an 18-Bit DAC.

FIGURE 3.11: Readout and actuation noises.

the Q factor by up to a factor of 1000 resulting in a $Q_x \approx 10^9$. For the tilt modes, the dilution factor is defined as $D_\theta = 2(d + L_{bend})/L_{bend} \approx 0.9$. The approximate Q factor for the tilt modes is then $Q_\theta \approx 10^6$. According to Gonzalez's 2000 paper [48], this approximation for the thermal noise is appropriate for mechanically decoupled systems, and for the 6D case, the main coupling mechanism in the system is due to the sensor motion rather than the mass motion.

Figure 3.12 shows the expected noise budget for all degrees of freedom. The dominant noise in all except vertical (Z) is the BOSEM actuation due to the DAC which quells the low frequency sensitivity below 0.1 Hz. It is also worth noting that during plant inversion, the sensor noise in X and Y below the translational resonance has a $1/f^2$ shape, and below the tilt resonance $1/f^4$. This occurs due to the 2x2 decoupling of the tilt-to-translational sensing. The decouplings are further discussed in Section 4.3.5, Section 4.3.4, and Chapter 5.

We also consider a high noise scenario, requiring $\pi/6$ rad of DC adjustment in RZ, and 10 mrad for RX, RY.

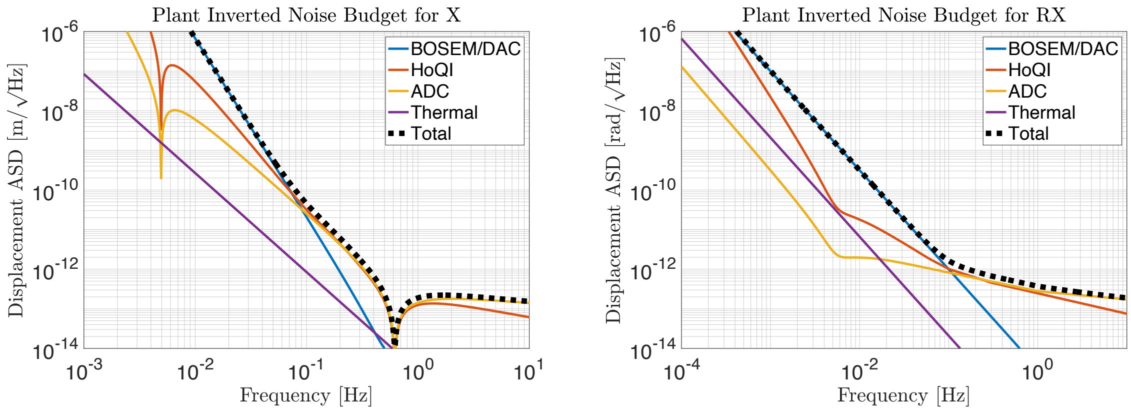

(A) X degree of freedom.

(B) RX degree of freedom.

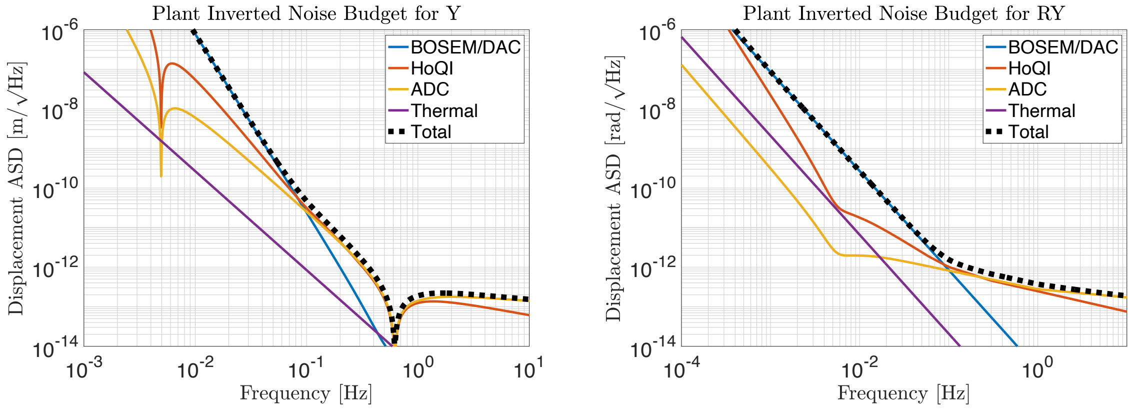

(C) Y degree of freedom.

(D) RY degree of freedom.

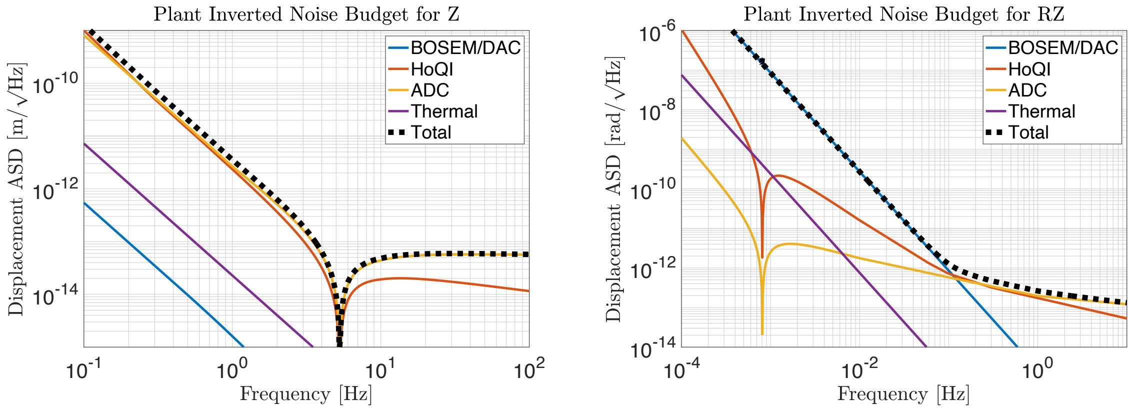

(E) Z degree of freedom.

(F) RZ degree of freedom.

FIGURE 3.12: Estimation of the noise sources for each degree of freedom after plant inversion.

Comparing the theoretical sensitivity of the 6D seismometer with various rotation sensors in the literature [3, 4, 5, 6, 7, 8], we find the broadband sensitivity to be greater than other sensors in both the low noise and high noise regimes.

The tilt decoupled power spectral noise, S_n^x, of two commercial seismometers, the L4C and T240, is described by Equation (3.38),

$$S_n^x = S_n \left(1 + \frac{2g^2}{\omega^4 L^2}\right) \tag{3.38}$$

where S_n is the noise of the seismometer, and L is the separation between two vertical seismometers used for tilt measurement. Again, the low noise and high noise regime of the 6D seismometer has greater broadband sensitivity than the tilt decoupled translational sensors.

The comparisons of the tilt and translational sensitivity of the device is shown in Figure 3.13 and Figure 3.14 respectively.

3.5 ISI model

In this section we derive the actuation matrix required to stabilise the platform from the CAD files of the ISI. The configuration of the actuation is based on the Stewart platform or hexapod, which consists of six actuators, allowing for independent motion of the six degrees of freedom. Such a design is used in an array of applications ranging from machine tools, flight simulators, telescope orientation and more. Unlike the majority of uses, the range of motion for our ISI is on the order of $10\,\mu$m, which results in a linearised system which can be approximated using the small angle approximations shown in Equation (3.8). Linear actuation is usually accomplished with hydraulic actuators due to their large range and strength, with a secondary option of rotary

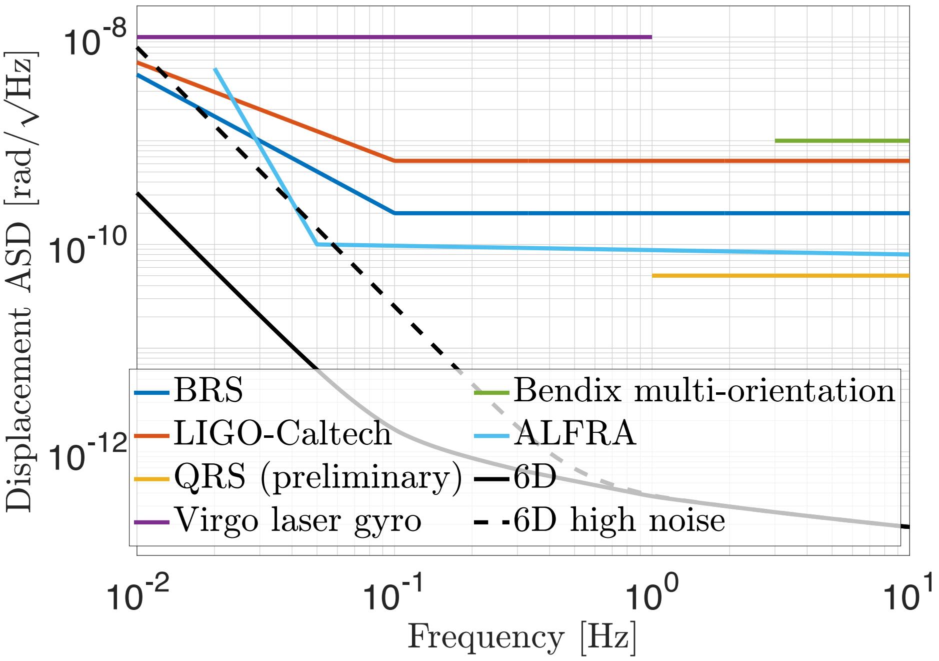

FIGURE 3.13: Comparison of the tilt sensitivity of various rotation sensors [3, 4, 5, 6, 7, 8] and the 6D seismometer.

actuators which are low budget. Actuation was achieved for our ISI using piezoelectric actuators to act as a linear driver. The key degrees of freedoms to be controlled are the tilt modes such that there is minimal coupling to the translational degrees of freedom.

Figure 3.15 shows the representation of the key coordinates required to determine the actuation matrix. There are three planes of interest shown in Figure 3.15a, the first is the base plane, which is considered fixed and never changes (yellow), the second is the upper plane (green) which is connected to the base via the piezo actuators, and finally the ISI platform (blue) which is offset from the upper plane by a fixed distance. We can define the centre of the upper plane with the coordinates, $\vec{U}$ where the home position is given by $\vec{U}(0)$, and the ISI position, $\vec{P}$ with home position $\vec{P}(0)$. As the ISI position and orientation are of interest, we define the end position of the j-th actuator $\vec{e}_j$ relative to the ISI. This can be determined using the vector $\vec{e}_j^{\,U}$, which is relative to

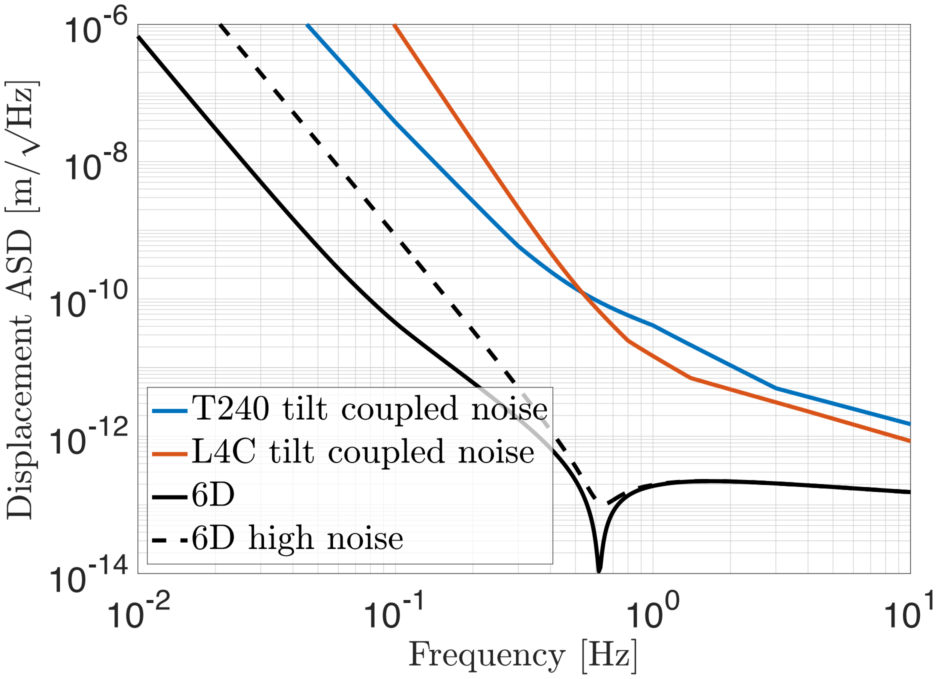

FIGURE 3.14: Comparison of the tilt decoupled translational sensitivity of commercial seismometers and the 6D sensor.

the centre of the upper plane. A visualisation of this can be seen in Figure 3.15b,

$$\vec{e}_j = \vec{P} + \mathbf{R}(\vec{U}(0) - \vec{P}(0)) + \mathbf{R}\vec{e}_j^{\,U} . \tag{3.39}$$

The orientation of the ISI is represented by the rotation matrix $\mathbf{R}$ where the rotation angles are the orientation of the ISI. Each leg length can then be determined as

$$L_j = \left|\vec{l_j}\right| = \left|\vec{e}_j - \vec{b}_j\right| \tag{3.40}$$

where $\vec{b}_j$ is the vector of the bottom of the piezo leg attached to the base plane. Due to the small angle approximations assumed, and the small range of the actuators, all terms of position and angle of the ISI which are of order two and higher can be neglected, resulting in a linear system. The six equations for each leg length can then

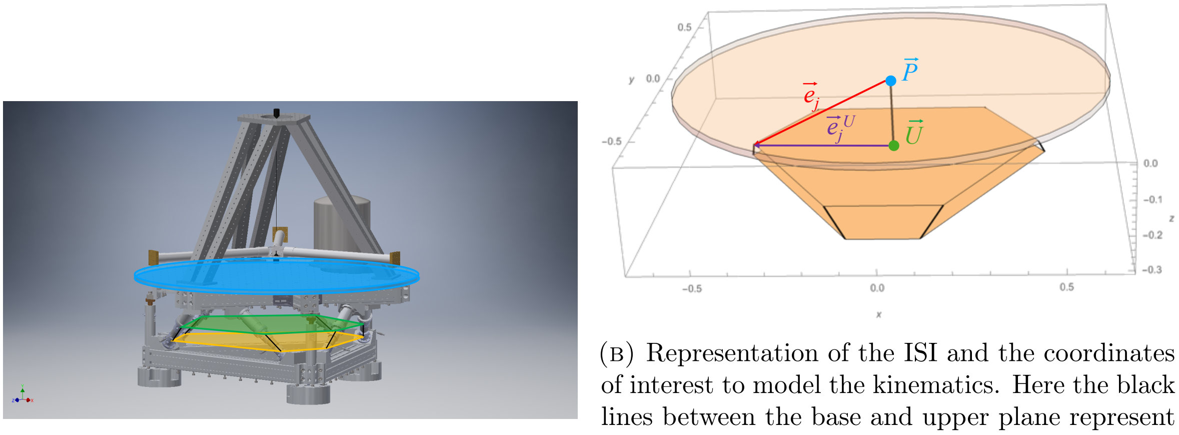

(A) Key points from the CAD file.

(B) Representation of the ISI and the coordinates of interest to model the kinematics. Here the black lines between the base and upper plane represent the piezo legs.

FIGURE 3.15: Illustration of the model used for determining the actuation matrix.

be represented as a matrix such that

$$\vec{L} = \mathbf{A}\vec{P}, \tag{3.41}$$

where $\vec{L}$ is a vector representing the six leg lengths, **A** is a 6x6 actuation matrix, and $\vec{P}$ is the vector of the platform position and orientation.

The piezo drivers used have a flat frequency response across the frequency band of 1 mHz to 100 Hz. For the pizeo actuators, the resolution in displacement is limited by the noise of the amplifiers. The output noise of the amplifier is 1 mV, for a full piezo range of 15 μm corresponding to a 1 kV driving voltage, the resultant displacement noise is 15 pm. This is the theoretical actuation noise floor that can be achieved using the SVR-500 piezo amplifiers [92]. This is approximately an order of magnitude higher than the readout noise floor for the X and Y degrees of freedom at 1 Hz as shown in Figure 3.12. However the SVR 500 can only provide a drive of 500 V, meaning that the displacement actuation range is approximately ±3 μm. This would limit the potential active isolation that can be achieved due to the lack of actuation range when trying to control large microseismic motion.

3.6 Summary

In this chapter we have discussed and analysed the derivations of the 6D seismometer by viewing simplified Lagrangian derivations for the various cases. The system was solved fully using the Wolfram Mathematica software which was analogous to the analytical results for the simplified degrees of freedom. Results from the model enabled the transfer functions to be used to determine noise budgets for the system which found that the noise of the BOSEM actuation was limiting below 0.1 Hz.

A second model was then constructed to determine the necessary actuation matrix required for use in stabilising the platform. Based on the Stewart platform, the actuation of the ISI used was achieved using low range piezo actuators which kept the system within the small angle approximations, simplifying the system into the linear regime. Key coordinates were taken from the CAD files of the ISI to model the system as accurately as possible. The results of this model were implemented to the ISI stabilisation discussed in Chapter 5.

Chapter 4

The Compact 6D sensor

Chapter 4 is an unedited version of the published paper [93] titled "A six degree-of-freedom fused silica seismometer: design and tests of a metal prototype". The author list is as follows: Amit Singh Ubhi, Jiri Smetana, Teng Zhang, Sam Cooper, Leonid Prokhorov, John Bryant, David Hoyland, Haixing Miao, and Denis Martynov. The work carried out for this project was lead by myself under guidance from my supervisor, Dr. Denis Martynov. During this project I constructed the prototype, recorded and analysed data and was the principle author of the paper. Section 4.3.2 and Section 4.4.1 was written by Dr. Denis Martynov. The analysis in Section 4.4.2 was conducted and written by Dr. Teng Zhang.

Section 4.6 is a separate small section regarding a recent update on the acquisition of the fused silica test mass.

4.1 Abstract

Ground vibrations couple to the longitudinal and angular motion of the aLIGO test masses and limit the observatory sensitivity below 30 Hz. Novel inertial sensors have the potential to improve the aLIGO sensitivity in this band and simplify the lock

acquisition of the detectors. In this paper, we experimentally study a compact 6D seismometer that consists of a mass suspended by a single wire. The position of the mass is interferometrically read out relative to the platform that supports the seismometer. We present the experimental results, discuss limitations of our metallic prototype, and show that a compact 6D seismometer made out of fused silica and suspended with a fused silica fibre has the potential to improve the aLIGO low frequency noise.

4.2 Introduction

The network of the Advanced LIGO [41] and Advanced Virgo [94] gravitational-wave (GW) detectors observed tens of signals from compact objects with masses up to 150 $M_\odot$ [12, 95, 96, 17, 97]. Most of the astrophysical sources were categorised as neutron stars and stellar mass black holes, with one event producing an intermediate-mass black hole [19]. The signals were mostly accumulated at frequencies from 30 Hz up to 500 Hz due to the diminished response of the detectors at lower and higher frequencies. Despite the sophistication and successful operation of aLIGO's seismic isolation platforms [2, 69], the sensitivity degrades below 30 Hz due to non-stationary control noise [84, 36, 98].

Improvements of the aLIGO inertial isolation will result in a number of benefits (i-v) for the detectors. Enhanced sensitivity below 30 Hz will lead to (i) routine observations of intermediate-mass black-holes since heavier compact objects merge at lower frequencies. Observing GWs at lower frequencies also increases the measurement time of mergers [84] and provides (ii) an improved localisation of the sources and enables early-warning alerts to search for the electromagnetic counterparts of events like GW170817 [17]. Furthermore, since the aLIGO lock acquisition process is a complex procedure that involves stabilisation of five longitudinal and tens of angular degrees of freedom [99, 100], suppression of the test mass motion will (iii) simplify the lock acquisition process. The coincident duty cycle of the aLIGO Livingston and Hanford detectors has the potential to (iv) increase from the current 62.2% [36] up to ≈ 75% once seismic distortions are further suppressed. Finally, reduced motion of the aLIGO test masses will allow us to increase the beam size in the arm cavities and (v) improve the coating thermal noise [51, 52] that limits the aLIGO sensitivity in its most sensitive frequency band around 100 Hz [36, 101].

A number of inertial sensors has been proposed in the literature [3, 79, 80, 82, 83, 81, 8] that have the potential to reduce the aLIGO platform motion and enhance the detector sensitivity. The key problem comes from the coupling of the aLIGO platform tilt to its horizontal motion. This coupling scales very unfavourably as g/ω^2, where g is the local gravitational acceleration, and ω is the angular frequency of the platform motion [64, 63, 62, 65]. The aLIGO detectors already utilise custom beam rotation sensors [3] developed by the University of Washington to measure the tilt motion of the ground. The next logical step would be to develop new custom sensors for the aLIGO platforms to further suppress their motion.

In this paper, we experimentally investigate a compact 6D seismometer that has the potential to measure the aLIGO platform motion in all six degrees of freedom [79]. The 6D seismometer is similar to drag-free control, which is a technique employed in satellites to keep the spacecraft a constant distance from a free-falling mass [102]. In contrast to the rotation sensors, we avoid mechanical constraints of the inertial mass and allow it to move freely in all degrees of freedom. The mechanical simplicity, however, leads to digital complexity since we need to diagonalise coupled degrees of freedom. In Sec. 4.3, we discuss experimental results, show how to diagonalise the coupled degrees of freedom, and compare the sensitivity of the 6D seismometer with commercial sensors.

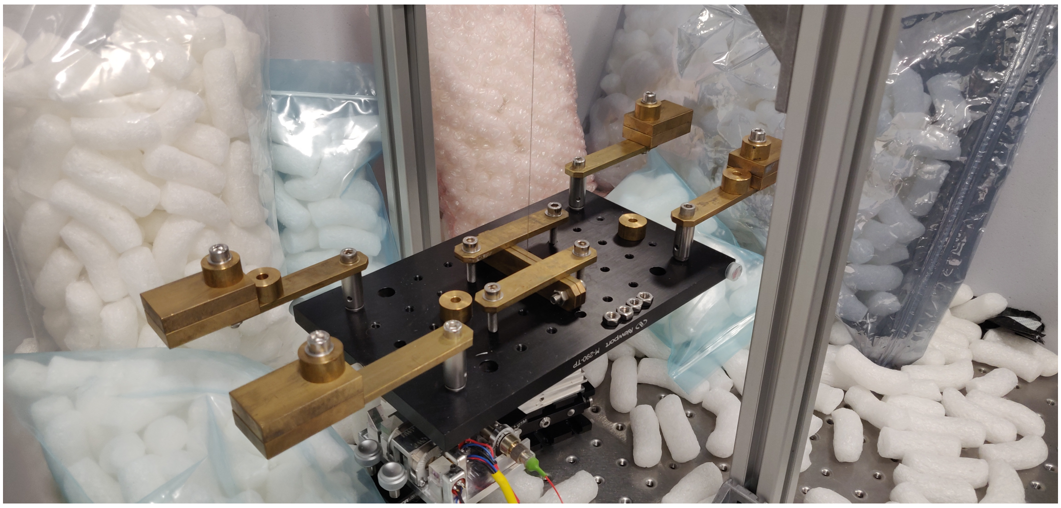

FIGURE 4.1: Picture of the isolated metallic prototype with an interferometric sensor.

In Sec. 4.4, we propose a vacuum-compatible version of the compact 6D seismometer and discuss the impact for the aLIGO detectors.

4.3 Metallic prototype

In this section, we discuss a metallic prototype, shown in Fig. 4.1, that was constructed with the aim of understanding the mechanics and dynamics of the system. The purpose was to provide insight for the fused silica design discussed in Sec. 4.4.

4.3.1 Mechanical design

The prototype used a 21 cm long, $r = 200\,\mu$m radius stainless steel wire to suspend an aluminium breadboard of dimensions $(254 \times 152.4 \times 12.7)$ mm - this was used as the base for the proof mass. We added additional brass masses to extend the proof mass and increase its moment of inertia to $I_{\mathrm{RZ}} \approx 0.076\,\mathrm{kgm}^2$, $I_{\mathrm{RY}} \approx 0.061\,\mathrm{kgm}^2$, $I_{\mathrm{RX}} \approx 0.015\,\mathrm{kgm}^2$, where RX, RY, and RZ implies rotation around the horizontal X- and Y-axes, and the vertical Z-axis. With these parameters, we achieved longitudinal eigenmodes along the

X- and Y-axes of 1.096 Hz. We set the vertical bounce mode of the suspension at 25 Hz. The rigidity of the vertical mode made the system impermeable to vertical motion of the ground below 10 Hz and simplified the measurement of the angular motion of the inertial mass. This can be seen in Fig. 4.4, where above 10 Hz the vertical commercial L4C seismometer [74] (orange) measures the same as the vertical sensor on the proof mass (red), and below this, the vertical motion is not dominant in the sensor. The torsional (RZ) eigenmode was set at 20 mHz.

The tilt (RX and RY) eigenmodes of the suspended mass depend on the vertical centre-of-mass position of the system according to the equation

$$\omega^2_{\mathrm{RX,RY}} = (2\pi f_{\mathrm{RX,RY}})^2 \approx \frac{mg\Delta z + k_{\mathrm{el}}}{I_{\mathrm{RX,RY}}}, \tag{4.1}$$

where Δz is the centre of mass position relative to the bending point of the bottom part of the wire, $k_{\mathrm{el}} = 1/2\sqrt{mgEI_a}$ is the elastic restoring coefficient of the wire, $m = 3.6\,\mathrm{kg}$ is the mass of the seismometer mass, $E = 210\,\mathrm{GPa}$ is the Young's modulus of the steel wire, and $I_a = \pi r^4/4$ is the second area moment of inertia of the wire.

For the configuration used, the tilt modes were $f_{\mathrm{RY}} = 84\,\mathrm{mHz}$ and $f_{\mathrm{RX}} = 167\,\mathrm{mHz}$ respectively. We adjusted Δz to create a gravitational anti-spring and lower the tilt modes. The centre of mass position was above the bending point by $\approx 0.8\,\mathrm{mm}$, creating an inverted pendulum. The resulting response was such that the effective spring constant $k_{\mathrm{eff}} = mg\Delta z + k_{el}$ was smaller than the restoring coefficient of the wire, k_{el}. We ensured that the effective spring constant still had a positive value so that the system remained stable. The key problem with reducing k_{eff} was that balancing the mass became difficult due to the plastic deformation of the steel wire as discussed in Sec. 4.3.2.

The system had quality factors of 2000 for the horizontal modes and 700 for the tilt modes. These quality factors were limited by air damping, and by mechanical losses in the metal fibres and in the clamping mechanisms. The large quality factors for a steel wire suspension led to significant motion of the inertial mass. We reduced the quality factors down to 70 and 3.5 for the longitudinal and tilt modes with eddy current damping. The effect of damping can be seen in Fig. 4.3 as the resonant peaks are broad.

4.3.2 Plastic deformations

The key experimental challenge of balancing the softly suspended mass came from plastic deformations in the steel wire. The wire stress due to the wire tension is given by the equation

$$\sigma_t = \frac{mg}{\pi r^2} = 281\,\mathrm{MPa}. \tag{4.2}$$

The stress, σ_t, was already close to the yield stress of the wire material (350 MPa) during the experiment. In addition to the stress from the tension, σ_t, DC tilts of the mass led to the extra stress near the surface of the wire given by the equation

$$\sigma_{\mathrm{RY}} \approx k_{\mathrm{el}} \frac{\alpha_{\mathrm{RY}}}{r^3} = 500 \frac{\alpha_{\mathrm{RY}}}{0.1\,\mathrm{rad}}\,\mathrm{MPa}, \tag{4.3}$$

where α_{RY} is the DC misalignment of the suspended mass around the RY axis. The total stress inside the wire has exceeded the yield stress for misalignment angles of only $\approx 10^{-2}$ rad. As a result of the plastic deformation, the equilibrium position of the suspended mass continuously changed during the balancing procedure that consisted of adding small masses to either side of the mass. We found that plastic deformations made the balancing procedure ineffective when k_{eff} approached zero.

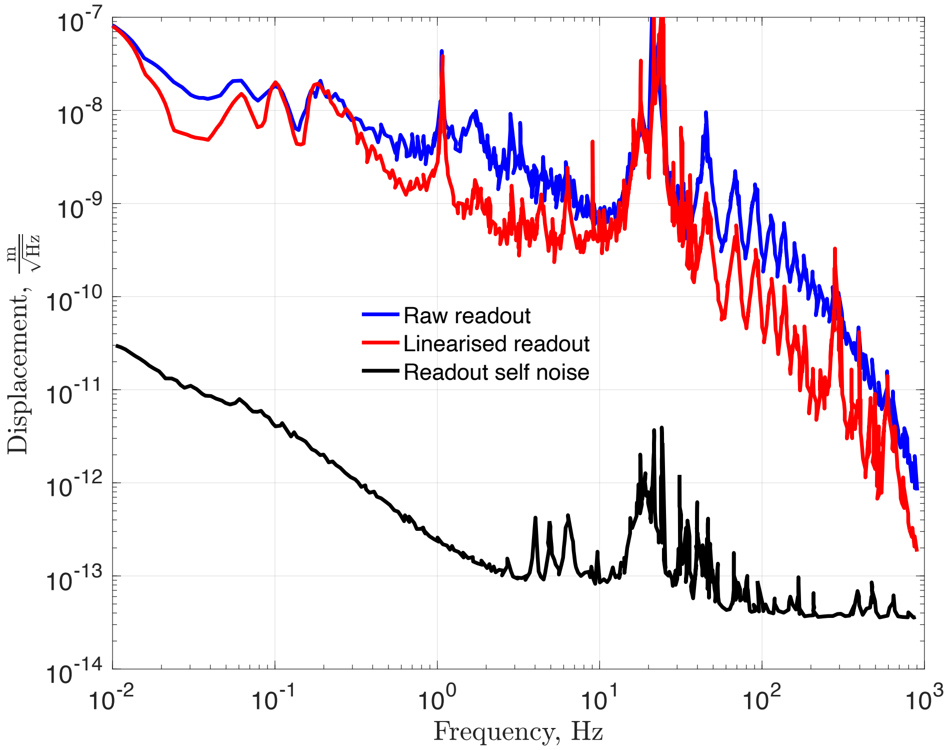

FIGURE 4.2: Example of nonlinearities witnessed in the interferometric readout during the experiment. The nonlinearities are strongly suppressed by fitting the Lissajous figures of the compact interferometers with ellipses. The black curve shows the self noise of the sensor measured with stationary mirrors.

4.3.3 Optical readout

Measurement of the proof mass was accomplished using interferometric readout with two Homodyne Quadrature Interferometers (HoQIs) [85]. We utilised only two sensors since this number is sufficient to understand the key cross-couplings between X and RY, and between Y and RX degrees of freedom as discussed in Sec. 4.3.4. One horizontal HoQI measured the translational motion (X), and another HoQI measured the vertical position at the end of the proof mass. The vertical motion was directly converted to RY motion of the mass below 10 Hz since the vertical mode of the suspension was rigid as discussed in Sec. 4.3.1.

HoQIs are compact Michelson interferometers that measure the position of the test mass relative to the reference mirror. The longitudinal range of the sensors is $> 10\,\mathrm{cm}$ since HoQIs measure the position with two polarisations and count optical fringes of the Lissajous figures [85]. The angular working range of the sensors is 1 mrad, therefore, isolation from environmental disturbances was necessary to keep the test mass within the HoQI working range as discussed in Sec. 4.3.5. Ideally, in order to achieve the best performance of the HoQI sensors, the RMS motion of the mass should be less than one fringe of the interferometer to reduce nonlinear effects in the data. However, the linearisation algorithms [85, 34] improve the broadband noise and up-conversion of large motion in the spectra as shown in Fig. 4.2. The linearisation can be further improved above 30 Hz by a more accurate ellipse fitting of the Lissajous figures [85, 34].

4.3.4 Mechanical cross-couplings

In the analytical study of the system dynamics [79], we found that the vertical (Z) and torsion (RZ) modes are independent from the other degrees of freedom. For a well aligned and balanced system, the cross-couplings only occur for the X and RY degrees of freedom and, similarly, for the Y and RX degrees of freedom. Further cross couplings can occur due to sensor misalignment, which will result in a more complex transfer function matrix. In this paper, we neglect second order cross couplings and experimentally investigate X and RY frequency-dependent coupling and its diagonalisation.

Fig 4.3 shows the couplings between the platform motion in X and RY degrees of freedom and readout of the inertial mass position. The platform motion in X strongly couples to the horizontal readout at and above the suspension resonance in X. Below the resonance, the inertial mass moves in common with the platform and the seismometer response is suppressed. In contrast to the 1D tiltmeters [3], the platform X motion also couples to the RY motion of the mass. Tilt motion of the platform has a minor effect

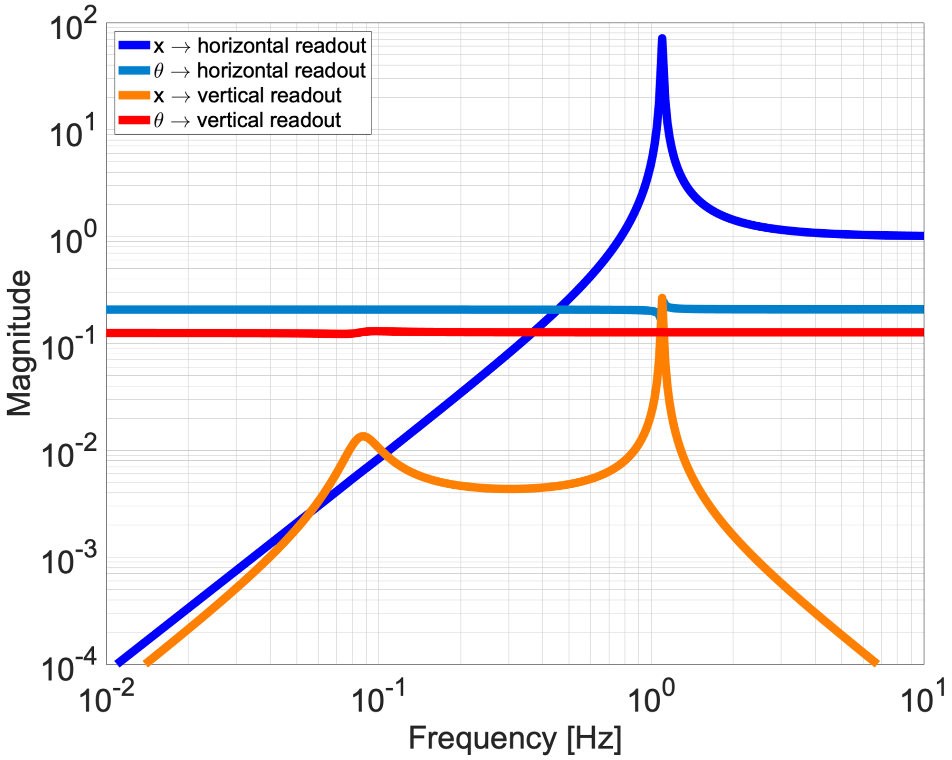

FIGURE 4.3: Transfer functions illustrating the coupling between the horizontal and vertical readouts due to the input platform translation x, and platform tilt θ.

on the mass motion in X and RY but moves the local sensors relative to the inertial mass and strongly couples to the readout.

In the case where we infer the X motion of the platform by looking only at the horizontal readout, we will get the typical tilt-to-horizontal coupling [64, 63, 62, 65]. This coupling is present in all 1D seismometers and is given by the equation

$$\hat{x} = x - \frac{g}{\omega^2}\theta, \tag{4.4}$$

where x is the translational platform motion, θ is its RY motion, and $\hat{x}$ is the inferred motion of the platform. In order to avoid the coupling given by Eq.(4.4), we infer the horizontal motion of the platform from both the horizontal and angular positions of the test mass according to the equation

$$\begin{pmatrix} \hat{x} \\ \hat{\theta} \end{pmatrix} = \begin{pmatrix} T_{\mathrm{x}\to\mathrm{h}} & T_{\theta\to\mathrm{h}} \\ T_{\mathrm{x}\to\mathrm{v}} & T_{\theta\to\mathrm{v}} \end{pmatrix}^{-1} \begin{pmatrix} x_m \\ z_m \end{pmatrix}, \tag{4.5}$$

where x_m and z_m are horizontal and vertical measurements of the HoQI sensors as discussed in Sec. 4.3.3 and the frequency dependent transfer matrix T is analytically derived and shown in Fig. 4.3.

4.3.5 Sensitivity

In the laboratory conditions, apart from ground motion, the soft suspension is susceptible to sources of environmental noise, such as air pressure and density fluctuations. The fluctuations move the test mass and couple to the position readout of the mass. To minimise these effects, we placed the system inside a foam padded box that acted as a shield from the local air currents. The box improved the environmental noise by a factor of 30 at 10 mHz. A further reduction by of factor 100 was achieved by back filling the box with foam pellets seen in Fig. 4.1. Despite this reduction of environmental noises, our tilt measurement was still limited by air currents below 100 mHz. We expect that environmental noises will disappear once we install the seismometer in vacuum.

Apart from the environmental noise sources, our readout signals measured the platform motion since the interferometric readout noise and thermal noises were significantly smaller compared to the ground vibrations in our experiment. We compared the readouts of our seismometer with commercial L4C sensors [74] as shown in Fig. 4.4. The L4Cs were co-located and co-aligned with the 6D seismometer to maximise coherence between the sensors. Fig. 4.4 shows the comparison between measured signals before

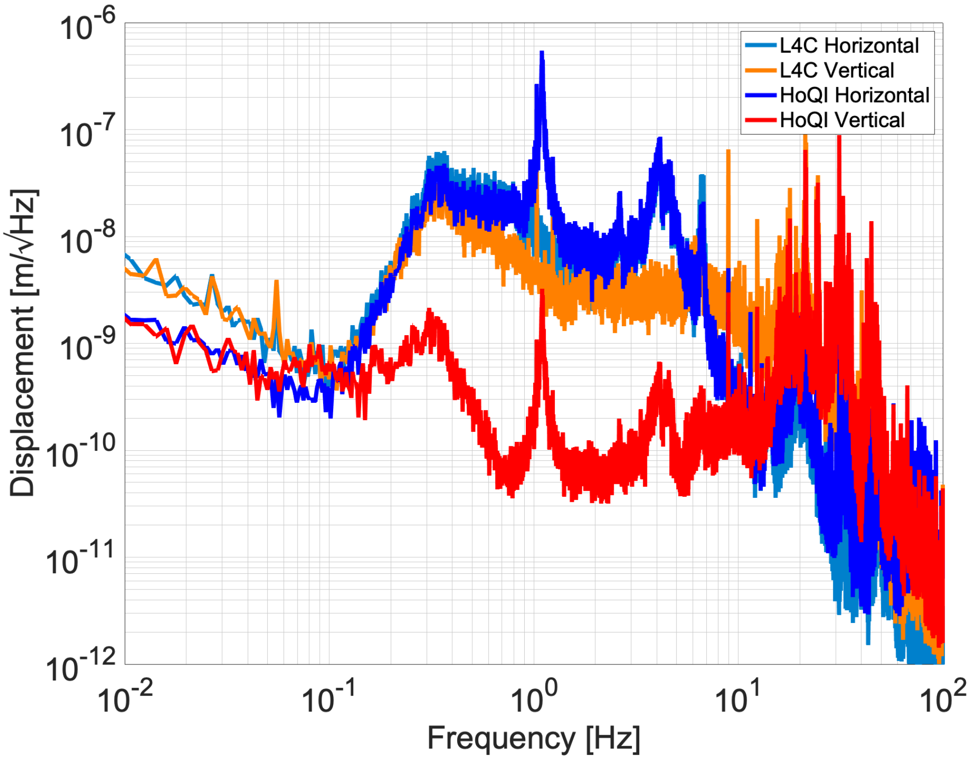

FIGURE 4.4: Comparison of measured motion between the compact 6D seismometer and commercial L4C geophones. The translational readout of the seismometer (blue) is similar to the L4C signal (light blue) above 100 mHz. The vertical readout (red) measures tilt motion of the inertial mass up to 10 Hz and vertical motion of the platform above this frequency. The vertical L4C (orange) measures the same motion as the vertical HoQI above the bounce mode resonance at 25 Hz.

plant inversion. The spectra for the HoQI horizontal and L4C horizontal are comparable because the resonances for both devices are the same (≈ 1 Hz). The Q factor for our seismometer is larger than that of the L4C hence Fig. 4.4 shows the more prominent 1 Hz resonance in the HoQI spectra. From these measurements we find that the compact 6D noise floor in air is already better than that of the L4Cs below 100 mHz.

According to our estimation of the platform translational and tilt motion, the horizontal HoQI sensor measures tilt motion below 100 mHz and translational motion at the other frequencies. The vertical HoQI sensor measures tilt and inertial mass motion

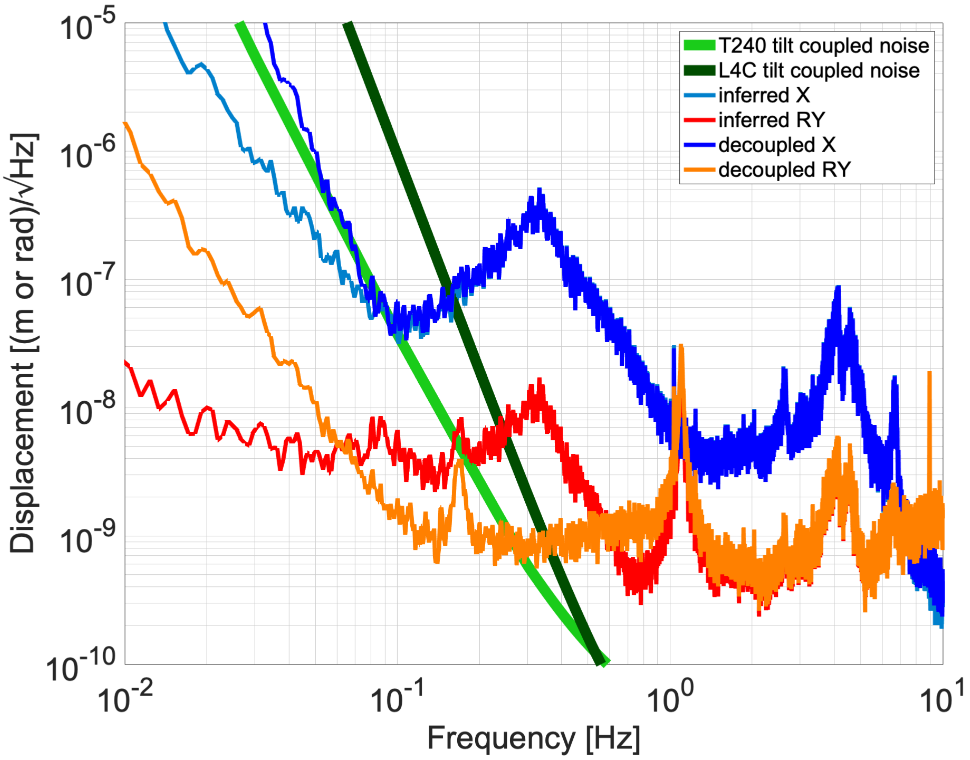

FIGURE 4.5: The figure shows the difference between the plant inversions of the translational and tilt modes with and without taking into account the X and RY cross-couplings. The orange curve shows the translation motion decoupled from the tilt mode such that the microseismic motion is removed. From the current sensitivity of the prototype, we see that the decoupled translational motion has the same noise floor as the tilt coupled T240 noise (green), and has better sensitivity than the L4C (dark green).

due to environmental noise below the tilt resonance at 85 mHz. Translational motion couples to the vertical tilt readout between the tilt and translational resonances of the suspension according to the transfer functions shown in Fig. 4.3. At frequencies from 1.5 Hz to 10 Hz, the vertical sensor measures the platform tilt motion, and vertical platform motion couples to the readout at higher frequencies.

We have diagonalised our readout signals according to Eq. (4.5) as shown in Fig. 4.5. The tilt-decoupled horizontal motion $\hat{x}$ is larger than the inferred horizontal motion without tilt subtraction since our tilt measurement is limited by the environmental noises below 100 mHz. However, the achieved sensitivity is comparable to the tilt-decoupled sensitivity of the Trillium T240 sensors [73] that are currently installed in the aLIGO detectors. We calculated the tilt-decoupled power spectrum of the T240 sensor noise according to the equation

$$S^x_{\mathrm{T240}} = S_{\mathrm{T240}} \left(1 + \frac{2g^2}{\omega^4 \Delta L^2} \right), \tag{4.6}$$

where $\Delta L = 1$m is the separation between two vertical T240 seismometers used for the measurement of the platform tilt motion, S_{T240} is the power spectrum of the T240 own noise, g/ω^2 is the tilt-to-horizontal coupling coefficient, and a factor of 2 in the brackets accounts for two T240 seismometers utilised in the tilt measurement.

Fig. 4.5 also shows the decoupling of the horizontal platform motion from the tilt measurement at frequencies between 85 mHz and 1 Hz. Apart from the platform tilt motion, we can also see coupling from the other degrees of freedom in $\hat{\theta}$. The resonance at 167 mHz corresponds to the RX eigen mode and the peak at 1.09 Hz corresponds to the coupling of the Y motion. We conclude that our sensors were not ideally aligned to measure only X and RY degrees of freedom. We leave this coupling problem for further experimental investigations.

4.4 Fused silica seismometer

From the lessons learned in Sec. 4.3, we propose to build the seismometer for GW detectors from fused silica and suspend the mass using a fused silica fibre, similar to the aLIGO test masses [49]. The design is compact (≈ 0.5 m scale) compared to the larger (≈ 1.2 m) scale 6D seismometer [79] that the authors investigated in collaboration with VU, Amsterdam. The compact design allows us to (i) achieve low drift rates of the

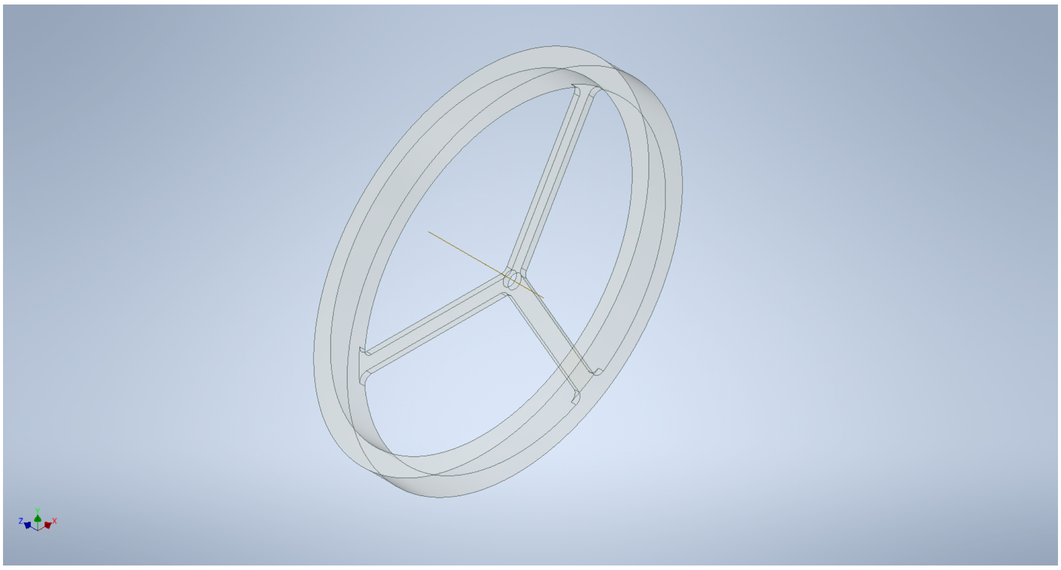

Figure 4.6: Model of the proposed fused silica compact 6D seismometer for the aLIGO active isolation platforms.

suspended mass as discussed in Sec. 4.4.1, (ii) utilise commercially available fused silica masses, and (iii) remove the angular control noise from the aLIGO sensitivity band.

We choose fused silica for the design of the compact 6D seismometer due to its low thermal expansion coefficient and low mechanical dissipation. In this section, we consider two designs of the seismometer with the tilt eigenmode at 50 mHz and 100 mHz, find the own noise of the seismometer, derive the aLIGO platform noise, and estimate the angular motion of the aLIGO test masses. We also compare our results with the performance of the currently installed T240 seismometers.

Fig. 4.6 shows the design of the fused silica suspension and Table 4.1 summarises the key parameters of the design. The customised commercially available fused silica mass [103] is circular in shape with the mass concentrated at the edges, and the three

Table 4.1: A list of parameters and nominal values

Parameters	Description	Value
m	Mass	3.25 kg
R	Mass radius	0.25 m
L	Wire length	0.4 m
r	Fibre radius at bending points	120 μm
$f_{\mathrm{X,Y}}$	Translational resonance	0.8 Hz
$f_{\mathrm{RX,RY}}$	Tilt resonance	50 mHz or 100 mHz

arms are designed to be as minimal as possible to reduce mass near the centre, therefore, maximising the moment of inertia for this configuration. The vertical and horizontal position of the centre of mass will be tuneable via small masses.

4.4.1 Low frequency drifts

Ideally, the angular modes of the suspended inertial mass should be as low as possible to diagonalise the tilt and translational signals of the seismometer. However, soft suspensions tend to drift at low frequencies due to stress relaxations in the fibre [104] and temperature gradients along the suspended mass. Strong drifts have the potential to move the system out of its interferometric sensing range. Experiments with torsion balances conducted in Washington [105], Paris, and Birmingham [106], and at the LISA facilities in Florida [107] and Trento [108] show that the fused silica suspensions drift less than the tungsten ones and that softer RZ eigenmodes lead to larger drifts.

We propose to stiffen RZ by making the fibre cross-section non-uniform: its radius will be $r = 120\,\mu$m near the fibre ends and $r = 500\,\mu$m near the centre of the fibre. The RZ eigenmode is then given by the equation

$$f_{\mathrm{RZ}} = \frac{1}{2\pi}\sqrt{\frac{E_t J}{L_{\mathrm{eff}} I_{\mathrm{RZ}}}}, \tag{4.7}$$

where $E_t = 30\,\mathrm{GPa}$ is the modulus of torsion of fused silica, $J = \pi r^4/2$ is the second moment of area along the axis of the cylindrical fibre, L_{eff} is the length of the fibre section with radius $r = 120\,\mu\mathrm{m}$. To stiffen RZ, the effective fibre length, L_{eff}, must satisfy the following condition

$$2\Delta = 2\sqrt{\frac{EI_a}{mg}} \ll L_{\text{eff}} \ll L, \tag{4.8}$$

where $\Delta = 600\,\mu\mathrm{m}$ is the bending length of the fibre, $L = 40\,\mathrm{cm}$ is the fibre length, and a factor of 2 accounts for two bending locations of the fibre. We choose $L_{\text{eff}} = 1\,\mathrm{cm}$ to satisfy Eq. (4.8) and get $f_{\mathrm{RZ}} = 31\,\mathrm{mHz}$. We expect the drift rate of less than $1\,\mu\mathrm{m/week}$ due to stress relaxation in the fibre.

Apart from the fibre unwinding, we also consider thermal gradients across the inertial mass. The gradients make different parts of the mass expand non-uniformly and cause the suspension to lose its balance. We estimate the angular deviation in RX and RY according to the equation

$$\theta_{\mathrm{rms}} \approx \frac{g\alpha\Delta T_{\mathrm{rms}}}{2R\omega^2_{\mathrm{RX,RY}}} = 1.6 \times \frac{\Delta T_{\mathrm{rms}}}{20\,\mathrm{mK}} \left(\frac{50\,\mathrm{mHz}}{f_{\mathrm{RX,RY}}}\right)^2 \mu\mathrm{rad}, \tag{4.9}$$

where $\alpha = 4 \times 10^{-7}\mathrm{K}^{-1}$ is the thermal expansion coefficient of fused silica [103], and ΔT_{rms} are thermal gradients along the inertial mass. We conclude that the thermal gradients are not significant for the proposed fused silica design.

4.4.2 Projected motion of the aLIGO platforms

The sensitivity of the inertial mass position readout is limited by the own noise of the compact interferometer, thermal noise of the suspension, and the actuation noise. The

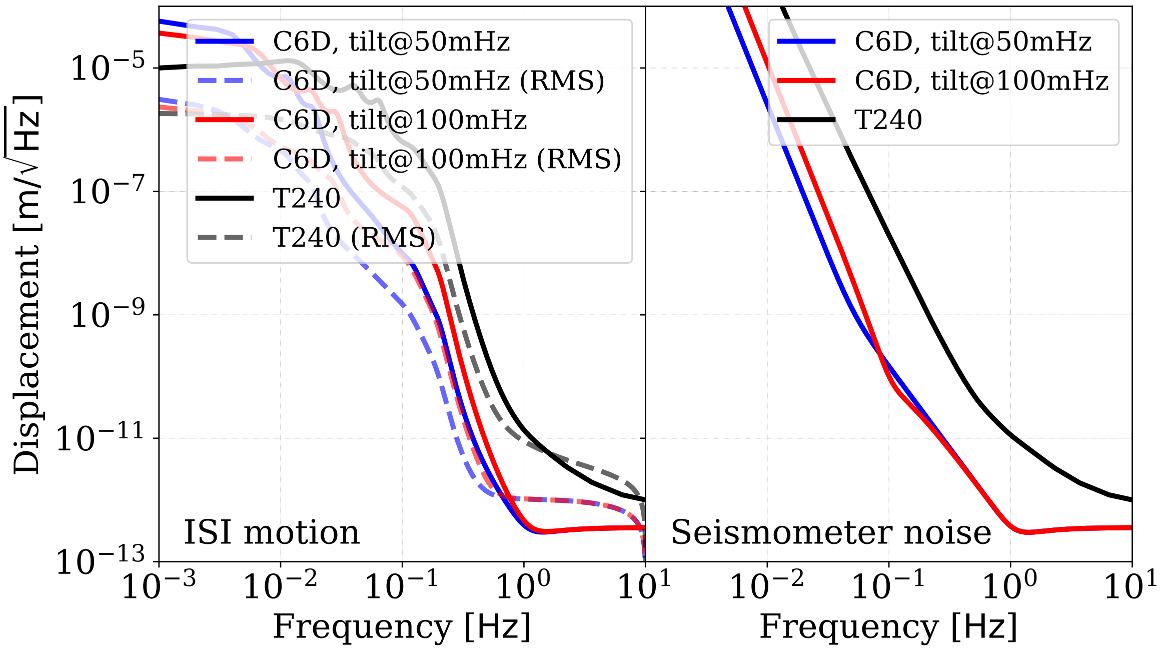

Figure 4.7: Estimated motion of the aLIGO platforms with the 6D seismometers (left). The right panel shows the comparison between the own noises of the 6D seismometers with the tilt eigenmode at 50 mHz and 100 mHz, and with the own noise of the T240 seismometers.

readout noise will be the dominant noise of the seismometer. We set the requirement of

$$S_{\mathrm{ifo}} = \left(3 \times 10^{-13}\right)^2 + \left(\frac{10^{-13}}{f}\right)^2 \frac{\mathrm{m}^2}{\mathrm{Hz}} \tag{4.10}$$

for the local readout of the mass position in the frequency band from 1 mHz up to 10 Hz. This level of sensitivity has been already achieved by the custom compact interferometers [85, 109].

Local readout noise couples to the estimated horizontal motion of the platform, $\hat{x}$. According to the dynamics of the system [79], the readout noise coupling to $\hat{x}$ grows as $1/f^2$ below the longitudinal resonances, $f_{X,Y}$, and as $1/f^4$ below the tilt resonances, $f_{\mathrm{RX,RY}}$ as shown in Fig. 4.7. The $1/f^2$ and $1/f^4$ couplings are similar to the current noise scaling in the aLIGO detectors. For the T240 seismometers, the $1/f^2$ slope starts from 1 Hz and the $1/f^4$ starts from the effective tilt resonance given by the equation

$$f^{\mathrm{T240}}_{\mathrm{RX,RY}} \approx \frac{1}{2\pi}\sqrt{\frac{2g}{\Delta L}} = 0.7\,\mathrm{Hz}. \tag{4.11}$$

Our calculations of the suspension thermal noise of the inertial mass show that it becomes insignificant for the quality factors of the tilt mode $Q_t > 2 \times 10^4$. Since the aLIGO suspensions achieve loss angles of the suspension fibres below 10^{-6} [50], the required quality factors can be achieved with the proposed fused silica suspension. We propose to damp the high quality resonances with magnet-coil actuators similar to the aLIGO suspensions [110]. The damping will allow us to reduce the quality factors of the suspensions down to ~ 10 and simplify the diagonalisation of the readout signals according to Eq. (4.5). Since we need to make the actuator noise insignificant, the actuator range will be 10 μm and will not be able to correct any strong low-frequency drifts. However, as discussed in Sec. 4.4.1, the fused silica design of the suspension will help avoid strong drifts.

The total noise of the seismometers, shown in Fig. 4.7, becomes larger than the ground motion below ≈ 30 mHz. In order to avoid large motions of the aLIGO platforms below 10 mHz, aLIGO utilises a blended control scheme [2, 65]. The aLIGO platforms follow the signals from the inertial sensors only above the blending frequency. At lower frequencies, the aLIGO platforms follow the signals from the positions sensors that measure the relative motion between the aLIGO platforms and the ground. A lower blending frequency provides better seismic isolation above 100 mHz but couples more inertial sensor noise to lower frequencies. In the aLIGO detectors, where T240 seismometers are currently deployed, the blending frequency is set at 45 mHz. The proposed 6D seismometer has the potential to lower the blending frequency by a factor of $2 - 3$ without increasing the RMS motion of the platform as shown in Fig. 4.7. In

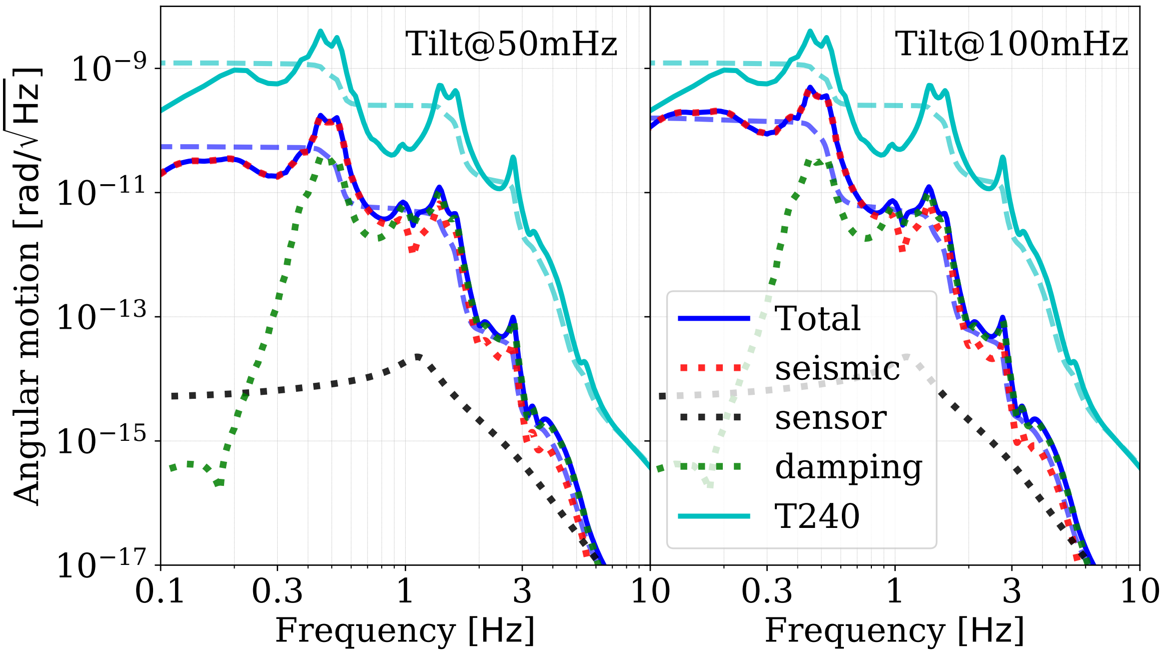

FIGURE 4.8: Comparison of the estimated pitch motion of the aLIGO test masses when the aLIGO platforms are stabilised with the proposed 6D seismometers with a tilt eigenmode of 50 mHz (left panel), 100 mHz (right panel) and the T240 seismometers.

this study, we find that a 6D seismometer with a tilt mode at 50 mHz (100 mHz) can reduce the blending frequency down to 14 mHz (22 mHz).

4.4.3 Projected motion of the aLIGO test masses

The key noise source of the aLIGO detectors at low frequencies (below 30 Hz) is the angular control noise. The motion of the aLIGO platforms causes angular motion of the test masses. The motion is then actively stabilised by wavefront sensors [111, 112]. The control loops keep the relative motion of the aLIGO test masses below ∼ 1 nrad, but couple the wavefront sensor sensing noise to the aLIGO GW channel [113]. The bandwidth of the angular control loops is currently set to be 3 Hz [98]. Since the 6D seismometer has the potential to improve the motion of the aLIGO platforms as shown in Fig. 4.7, the angular controls bandwidth can be reduced by a factor of 3 and remove coupling of the aLIGO angular controls to its sensitivity band above 10 Hz [84].

In this section, we estimate the angular motion of the aLIGO test masses with the 6D seismometer. The dominant angular motion of the aLIGO test masses comes from the longitudinal motion of the aLIGO platforms [84]. We propagate the platform motion through the transfer functions of the aLIGO quadruple suspensions and compute the motion of the test masses. We find that we can achieve residual relative motion of the aLIGO test masses below 1 nrad with a control bandwidth of 1 Hz and a typical wavefront sensor noise of $5 \times 10^{-15}\,\mathrm{rad}/\sqrt{\mathrm{Hz}}$ when the tilt mode of the seismometer inertial mass is either 50 mHz or 100 mHz. The results of mirror angular motion are shown in Fig. 4.8. The damping noise comes from the local sensors that damp the high quality factors of the aLIGO suspensions. In computing the damping noise for Fig. 4.8, we assume that the aLIGO suspensions are equipped with the same interferometeric positions sensors as the 6D seismometers.

We find that both configurations of the 6D seismometer from Table 4.1 have the potential to solve the problem of the aLIGO angular control coupling to the GW channel below 20 Hz. The 100 mHz configuration is easier to implement compared to the 50 mHz one since center-of-mass tuning Δz can be less precise. However, the 50 mHz version provides significantly better inertial isolation in the earthquake band between 30 mHz and 300 mHz, and has the potential to keep the aLIGO detectors operational during small and medium earthquakes (local RMS velocity of the ground below $\sim 1\mu\mathrm{m/s}$) and further improve the aLIGO duty cycle.

4.5 Conclusion

Novel inertial sensors can enhance the sensitivity of the aLIGO detectors below 30 Hz, improve their duty cycle, and open a pathway towards increasing the beam size in the aLIGO arms. In this paper, we presented experimental results from our studies of the compact 6D seismometer with an interferometric readout. We conclude that the seismometer has the potential to improve aLIGO's seismic isolation. Measurement of the horizontal and tilt modes of the metallic prototype resulted in validation of the decoupling capabilities of the readout scheme though decoupling around the horizontal eigen mode requires further investigations. We found that lower tilt eigenmodes of the suspended mass make the balancing procedure complicated due to plastic deformations in the wires.

Using the lessons learned from the metal prototype, we proposed and simulated the performance of a fused silica compact 6D seismometer with the tilt modes at 50 mHz and 100 mHz. We found that both configurations should have low angular drift rates due to the mechanical and thermal properties of fused silica. The seismometers are capable of improving the current aLIGO low frequency noise but the 50 mHz design also provides strong suppression of the the ground motion in the earthquake band. Experimental investigations of the compact fused silica 6D seismometer will be our next step.

4.6 Fused Silica Mass

A design for the fused silica mass was made with the aim of maximising the moment of inertia. Alterations were made from the initial design discussed in Section 4.4 with considerations of fibre mounting and suggestions from the manufacturer, Heraeus [103].

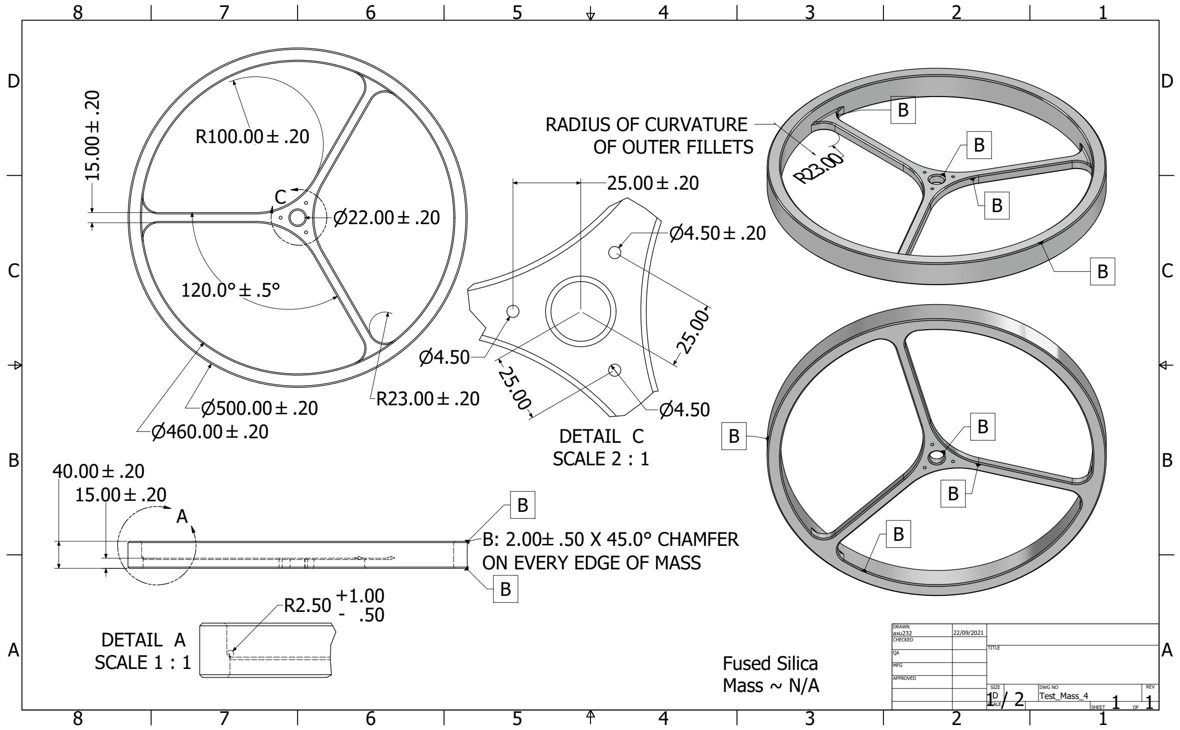
R100.00 ± .20
15.00 ± .20
C
Ø22.00 ± .20
120.0° ± .5°
Ø500.00 ± .20
Ø460.00 ± .20
R23.00 ± .20
RADIUS OF CURVATURE OF OUTER FILLETS
25.00 ± .20
Ø4.50 ± .20
25.00
Ø4.50
25.00
Ø4.50
DETAIL C
SCALE 2 : 1
R23.00
B
40.00 ± .20
15.00 ± .20
A
B: 2.00± .50 X 45.0° CHAMFER ON EVERY EDGE OF MASS
R2.50 +1.00 - .50
DETAIL A
SCALE 1 : 1
Fused Silica
Mass ~ N/A
22/09/2021
Test_Mass_4

FIGURE 4.9: Drawing provided to Heraeus for manufacturing the fused silica compact 6D test mass.

The drawing in Figure 4.9 was provided to the manufacturer who have produced and shipped two test masses.

Table 4.2 on page 97 highlights key parameters of the test mass. The tilt resonances are highly susceptible to the centre of mass position as described in Equation (4.1). Increasing the centre of mass position was a key design consideration, hence the slim profile of the base and the raised outer ring. We have been able to raise the centre of mass position to more than 3 mm above the height of the arms, h. Increasing the moment of inertia was also paramount which led to the majority of the mass placement at the outer perimeter.

Attachment of the fibre is intended to be fixed from the underside of the mass. This would lead to the fibre anchor (thicker mounting area at the fibre end) lying within the

Table 4.2: Properties of the fused silica test mass manufactured by Heraeus.

Parameters	Description	Value
m	Mass	2.995 kg
D	Total diameter	500 ± 0.5 mm
D_{in}	Inner diameter	460 ± 0.5 mm
H	Height of outer ring	40 ± 0.2 mm
h	height and width of arms	15 ± 0.2 mm
D_{centre}	Central hole diameter	22 ± 0.2 mm
I_x	Moment of Inertia about x-axis	$0.079\,\text{kgm}^2$
I_y	Moment of Inertia about y-axis	$0.079\,\text{kgm}^2$
I_z	Moment of Inertia about z-axis	$0.158\,\text{kgm}^2$
d_{CoM}	Centre of mass from bottom face	18.4 mm

central hole. Final design considerations regarding centre of mass tuning are still being investigated. However, a simple idea of using spacers between the end of the fibre and the test mass would enable coarse tuning of the centre of mass, further increasing its position relative to the apparent bending point of the fibre.

Figure 4.10 is a photograph of the fused silica test mass. Using the newly acquired test mass, initial investigations regarding mass balancing will begin by suspending the design from a metal fibre. Current collaborations with Dr. Haixing Miao of Tsinghua University in China are aiding the acquisition of fused silica fibres. This would result in a more monolithic design and potentially reduce the drift motion in the angular degrees of freedom. The readout scheme has been investigated using custom commercial interferometric sensors, with plans to employ this on the newly designed test mass [114].

Figure 4.11 shows an estimate of the noise floor for the proposed fused silica test mass compared to the estimated noise floor of the prototype.

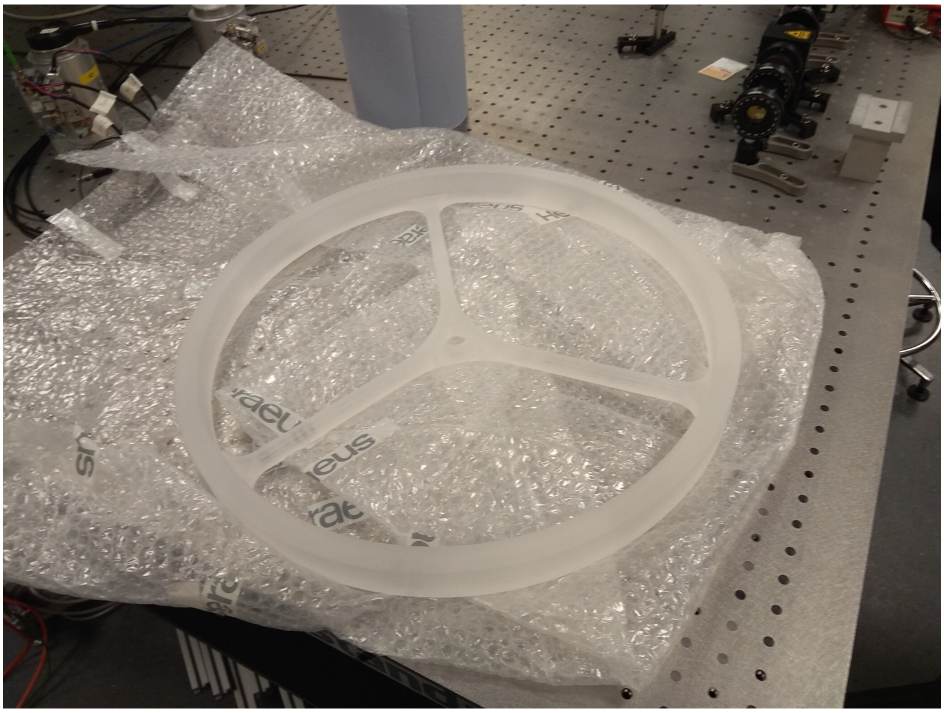

Figure 4.10: Photograph of one of the manufactured fused silica test masses.

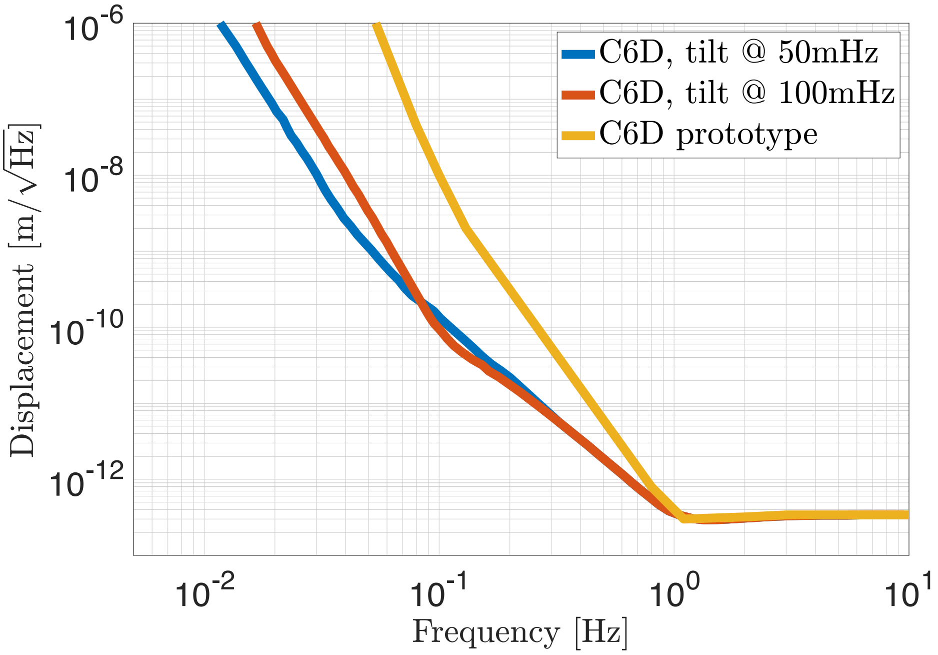

Figure 4.11: Estimated noise floors of the fused silica compact 6D mass and the prototype discussed in Chapter 4.

Chapter 5

Demonstration of the control system for the 6D seismometer

Chapter 5 is a mature draft of the paper titled "Demonstration of the control system for the 6D seismometer". The author list is as follows: Amit Singh Ubhi, Leonid Prokhorov, Sam Cooper, John Bryant, David Hoyland, and Denis Martynov. The work contained within this chapter was a collaborative project on which I took lead in implementing the control system under the supervision of Dr. Denis Martynov. I am the principle author, and Dr. Denis Martynov contributed by writing 5.4. Figures were made by myself and Dr. Denis Martynov.

5.1 Abstract

We demonstrate the viability of a six degree of freedom (6D) seismometer which is sensed using six optical shadow sensors. The seismometer was used in feedback to control a rigid isolation platform and required feedforward techniques to decouple the sensed degrees of freedom. This was imperative for simultaneous stabilisation of all six degrees of freedom and enabled high gain bandwidth control of the platform resulting in

over an order of magnitude suppression for 5 of 6 coordinates. Further suppression was limited by the piezo actuation of the platform due to limited range, hysteresis, and non linearities. In this paper we discuss the control techniques used, and the limitations of the test bed, proposing improvements which will be implemented in the next iteration of testing.

5.2 Introduction

The LIGO [41] and Virgo [94] detectors have made a number of gravitational wave detections from massive compact objects [12, 14, 15, 16]. Sources of these waves range from two recent neutron star black hole systems [20], and binary black holes [95, 96, 19], with one detection of an intermediate mass black hole of mass $\sim 150\,\mathrm{M}_{\odot}$ [19]. A multimessenger event was also observed from a binary neutron star merger which verified localisation and decreased the false alarm rate of the detection [17].

Low frequency sensitivity of the detectors determine the likelihood of observing more massive systems such as intermediate mass black hole binaries between $100 - 1000 M_{\odot}$ as well as providing early warning signals. The merger time of binary systems scale with frequency as $f^{-8/3}$, enabling opportunities for multimessenger detections due to early detections of inspirals. For the LIGO detectors, these signals are cloaked by the non-stationary control noise of the isolation scheme of the core optics [84, 36, 98]. The LIGO isolation scheme consists of a four stage pendulum suspended from state of the art two stage twelve axis platforms for the detectors' core optics [2, 69, 68]. Despite the orders of magnitude suppression achieved, the angular controls for the core optics limit the detectors' sensitivity below 30 Hz [113, 112].

Improved sensing of the isolated platforms would reduce the input motion to the suspension chain, reducing the injection of noise from the local damping on the optics. Suppression of platform tilt is limited by the lack of absolute rotation sensors on the platforms. The platform tilt also plagues the translation readout with an unfavourable coupling of g/ω^2 [62, 65], where g is the local gravitational acceleration and ω the angular frequency. Investigations into improved sensing of the platforms are being investigated by a number of groups who develop novel inertial sensors. The University of Washington have employed the out of vacuum beam rotation sensor (BRS) [3] at LIGO for sensor correction, and are developing an in vacuum cylindrical rotation sensor (CRS). The University of Western Australia have developed the ALFRA rotational accelerometer which has the advantage of multi-orientation such that it can also be mounted vertically [8]. Optical gyroscopes have also been investigated at Caltech and MIT which make use of the Sagnac effect to measure absolute rotation [82, 83]. Further improvements to low noise translational inertial sensing have been demonstrated by the Nikhef and VU groups in Amsterdam [81], and the Belgium China collaboration [80, 115] with custom interferometric inertial sensors.

In this paper we present an initial version of the 6D seismometer detailed in [79]. The basis behind the design is a softly suspended extended reference mass which is readout in six degrees of freedom (6D). Unlike the inertial sensors discussed above, the approach differs by utilising a simple mechanical design which enables cross couplings. Complexity is moved to the signal processing where the degrees of freedom must be untangled.

We demonstrate the viability of the device for use in feedback by stabilising a rigid isolated platform in six degrees of freedom. First we discuss the experimental design, and then move through the control scheme used, indicating the performance achieved and the shortcomings of the test bed used.

5.3 Experimental design

The setup consists of a single extended reference mass suspended from a fused silica fibre [49, 50]. Optical shadow sensors known as Birmingham Optical Sensors and Electromagnetic Motors (BOSEMs) [110] were employed for the readout scheme, which measured the relative displacement between the proof mass and the platform. The test bed was a rigid stabilisation platform which was actuated using six piezo legs in a hexapod style formation. The experimental set up is shown in Fig. 5.1a.

Ideally the eigenmodes of the mass would be as low as possible to enable inertial sensing to lower frequencies. The vertical bounce mode, Z, was limited by the total mass and the fibre properties, where the stiffness coefficient $k_z = EA/L$, where E is the Young's modulus, and A and L are the fibre's cross sectional area and length respectively. This resulted in a stiff mode in Z with a resonant frequency of 10 Hz.

The remaining 5 degrees of freedom were softer, with X and Y being limited by the fibre length - a design constraint due to the height of the vacuum chamber which houses the device.

Resonant frequencies for the tilt modes (RX, RY) were tunable due to the similarities in strength between the elastic restoring coefficient of the fibre, $k_{el} = \frac{1}{2}\sqrt{mgE\pi r^4/4}$ (assuming a circular cross-section), and the gravitational restoring force. The distance between the effective pivot point of the wire and the centre of mass, d enabled tuning of the effective restoring moment as indicated in Eq. (5.1) [93],

$$\omega_{\mathrm{X}}^2 \approx \frac{g}{L}, \qquad \omega_{\mathrm{RY}}^2 \approx \frac{mgd + k_{el}}{I_y}, \tag{5.1}$$

where m mass, and I_y is its moment of inertia about the y-axis.

Table 5.1 contains a list of the design parameters for the experimental setup, highlighting the resonant frequencies of the proof mass.

In the case of a symmetric fibre neck and mass, the circular cross section results in an infinite number of principle axes, resulting in no preferential axes around which the tilt motion occurs. This was initially assumed and an arbitrary direction for the X and Y axes was chosen.

We discovered a discrepancy between the tilt resonances such that $f_{\mathrm{RX}} \neq f_{\mathrm{RY}}$. Investigations determined that asymmetry in the fibre neck, where bending occurs, gave rise to two perpendicular principal axes around which tilting occurred. The asymmetry resulted in non-identical elastic restoring constants, k_{el}, for RX and RY, where the frequency splitting of the modes was further exacerbated by the tunable gravitational restoring torque, mgd.

Measurement of the degrees of freedom were determined using a sensing matrix, $\mathbf{S}$, which converted the six BOSEM signals, $\vec{B}$ into the six degrees of freedom, $\vec{X}$, such that $\vec{X} = \mathbf{S}\vec{B}$. The preferential axes for tilt caused coupling of RX eigenmode into the sensed RY motion (and RY to RX). Analysis of the individual BOSEM signals allowed us to determine the angular misalignment of our original axes compared to the principal axes due to the fibre asymmetry. A rotation matrix, $\mathbf{R}$ was implemented to align the sensing with the eigenmodes of the principal axes, $\vec{X}_{eig}$, such that,

$$\vec{X}_{eig} = \mathbf{R}\vec{X} = \mathbf{R}\mathbf{S}\vec{B}. \tag{5.2}$$

The soft angular modes of the system result in large oscillations which ring down over periods much larger than the resonance. Another characteristic of the soft modes are their susceptibility to external noise sources which can cause large angular displacements of the mass. For this reason, sensing using BOSEMs is not ideal due to their limited linear

TABLE 5.1: A list of parameters and nominal values

Parameters	Description	Value
m	Mass	1 kg
R	Mass radius	0.6 m
L	Wire length	0.64 m
r	Fibre radius	$100 \pm 10\,\mu$m
$f_{\mathrm{X,Y}}$	Translational resonances	0.62 Hz
f_{Z}	Vertical resonance	10 Hz
f_{RX}	RX tilt resonance	100 mHz
f_{RY}	RY tilt resonance	90 mHz
f_{RZ}	Tilt resonance	2 mHz

range of 0.7 mm [116]. Implementation of damping on the resonant modes improved the sensing by reducing the relative motion of the mass to the sensors. However, the requirement of simultaneous alignment of six sensors on a softly suspended proof mass resulted in varying DC positions for each device, reducing the dynamic range to below its nominal value. Future updates will include the use of interferometric sensing which has increased range and improved noise performance [85, 114]

Actuation of the platform is accomplished using the error signal of the damping loops. Ideally the platform would be actuated on in high gain to fix the platform position relative to the proof mass, akin to the drag free control concept implemented in LISA pathfinder [86].

Fig. 5.1b shows the damped signals using the BOSEM actuation with no control of the platform. Large translational motion in X leaks into the other degrees of freedom, which can be seen from the presence of the microseism and resonant peak at 0.62 Hz. Reduction of the X (Y) platform motion diminishes this effect as the platform tracks the motion of the proof mass. Investigations into the BOSEM sensing and actuation noise found that are stiffest mode (Z) was limited by sensor noise below 10 Hz, and that

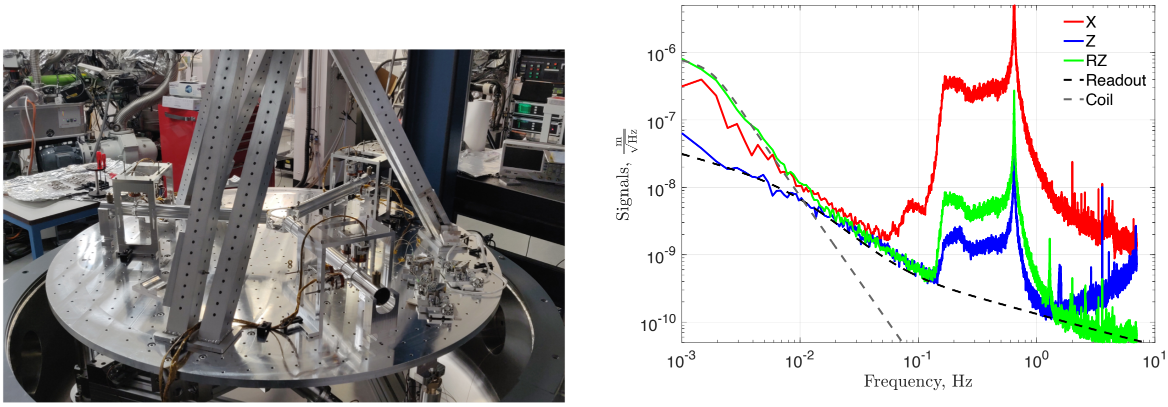

(A) Photo of experimental setup of 6D.

(B) Signals of the various degrees of freedom, note that the Y and RX degrees of freedom are analogous to X and RY.

FIGURE 5.1: (a) Image of the experimental setup and (b) an example of the measured signals with the corresponding noises.

the DAC noise from out control system dominates the RZ motion below 10 mHz.

The following sections discuss the control strategy used to stabilise the actuated platform and the issues faced when controlling a multi degree of freedom system. We then look at the achieved performance and suggest improvements for the system.

5.4 Control strategy

In this section, we discuss the stabilisation technique of the actuated platform relative to the 6D seismometer. First, we present our solution to the control problem. We found that the key element for the successful stabilisation is the feedforward subtraction of the measured longitudinal signals (X and Y) from the tilt signals (RY and RX). Second, we discuss the control problem that is relevant to the class of actuated platforms with cross couplings between different degrees of freedom on the level of ≈ 1%.

5.4.1 ISI stabilisation

The ISI causes movement of the suspension frame and the test mass shown in Fig. 5.1a. However, the test mass is considered to be inertial above the pendulum resonant frequencies. The coupling of ISI motion to the sensor outputs can be written as

$$\begin{aligned} X &= T(f)X_{\mathrm{ISI}} + L \times RY_{\mathrm{ISI}} \qquad , \\ RY &= K(f)X_{\mathrm{ISI}} + RY_{\mathrm{ISI}}. \end{aligned} \tag{5.3}$$

X and RY as well as Y and RX are intrinsically coupled by the pendulum. Transfer functions $T(f)$ and $K(f)$ are determined by the pendulum and pitch resonances and are discussed in details in [93].

According to Eq. (5.3), the coupling of X and RY and, similarly, Y and RX degrees of freedom is frequency dependent. Therefore, we implement a filter to diagonalise the degrees of freedom as shown in Fig. 5.2a. We found that the control system requires the subtraction of X (Y) from RY (RX), hence a 2x2 diagonalisation is necessary for stability.

We determined the feedforward filter by solving Eq. (5.3) relative to X_{ISI} and RY_{ISI}. Since the solutions are given by the equations

$$\begin{aligned} X_{\mathrm{ISI}} &= \frac{1}{T - LK}\left(X - L \times RY\right), \\ RY_{\mathrm{ISI}} &= \frac{T}{T - LK}\left(RY - \frac{K}{T}X\right), \end{aligned} \tag{5.4}$$

the feedforward filter should be given by the equation

$$\frac{K}{T} = \frac{\omega_{\mathrm{RY}}^2}{-\omega^2 + \frac{i\omega\omega_{\mathrm{RY}}}{Q_{\mathrm{RY}}} + \omega_{\mathrm{RY}}^2}\frac{1}{L} \approx -\frac{\omega_{\mathrm{RY}}^2}{\omega^2 L} \tag{5.5}$$

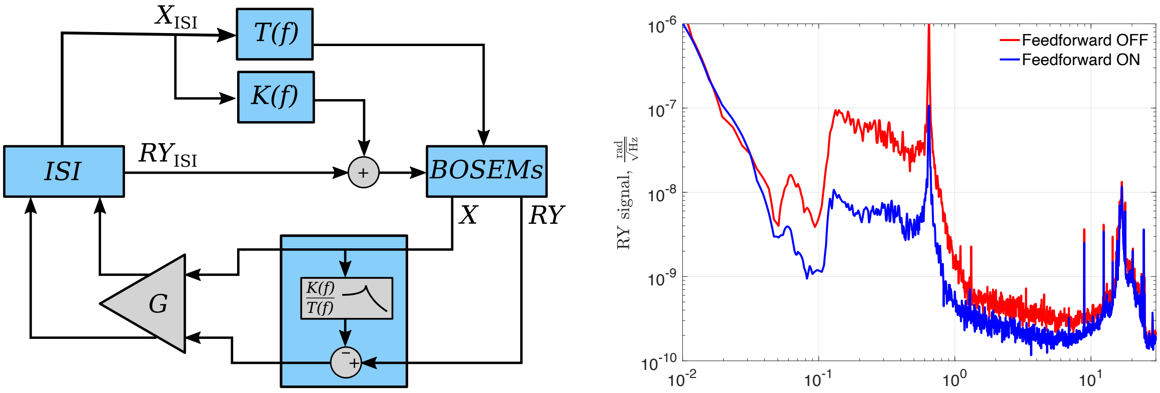

(A) Block diagram showing the feedforward scheme to subtract the translational induced tilt motion from the RY measurement.

(B) Comparision of the RY signal with (blue) and without (red) feedforward of the X signal.

FIGURE 5.2: Feedforward scheme for decoupling tilt translation from tilt.

at $\omega \gg \omega_{\text{RY}}$. However, during our experimental studies we found that $\sim \omega^{-2}$ dependence is only valid up to $\omega \approx 10\omega_{\text{RY}}$. At higher frequencies, the transfer function flattens due to the cross-couplings of signals in our sensors. Therefore, we fitted the feedforward filter to the transfer function $K/T + \alpha$, where α is a small number on the order of 10^{-2}. The result of the feedforward cancellation is shown in Fig. 5.2b.

5.4.2 Control problems from the ISI cross-couplings

Application of the feedforward scheme discussed above enabled successful stabilisation of the platform.

The upper unity gain frequency was constrained to 10 Hz due to the unsuspected mechanical resonances of the ISI platform from 14 Hz and above. These resonances cause instabilities in the control scheme, and due to the number of modes, it was implausible to attempt to digitally remove them from all degrees of freedom.

The bandwidths achieved for the angular modes were 70 mHz-10 Hz for the tilt modes (RX, RY), and 10 mHz-10 Hz for RZ. For the longitudinal degrees of freedom

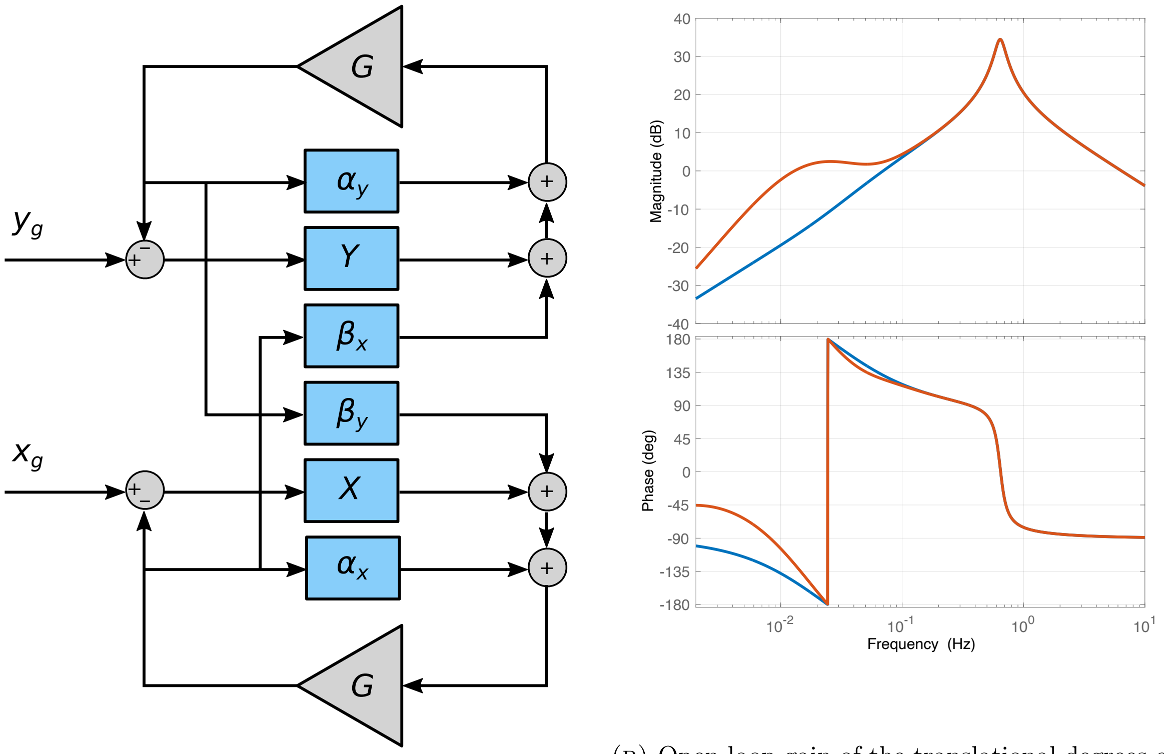
G
α_y
y_g
Y
β_x
β_y
x_g
X
α_x
G
+
−
Magnitude (dB)
40
30
20
10
0
-10
-20
-30
-40
Phase (deg)
180
135
90
45
0
-45
-90
-135
-180
10^{-2}
10^{-1}
10^{0}
10^{1}
Frequency (Hz)

(A) Block diagram representing the cross coupling of the actuation scheme

(B) Open loop gain of the translational degrees of freedom. The blue trace indicates the loop gain with idealised actuators whereas the red trace is the unstable loop gain due to the extra cross coupling factors.

FIGURE 5.3: Control scheme illustrating the actuation cross couplings and its effects.

the bandwidth attained was 250 mHz-10 Hz, where the lower unity gain frequency was limited by cross-couplings of the ISI actuation between the X and Y degrees of freedom as illustrated in Fig. 5.3a.

We discuss the reason for the instabilities of the control loops for X and Y in this section. The key problem of the X and Y cross-coupling is its frequency dependence. We found that above 1 Hz the cross-coupling is on the order of 1%. However, the coupling grows towards the lower frequencies. The response in X and Y to the excitation in X degree of freedom is equal at 40 mHz. The cause of the large cross-coupling occurs due to imperfections in the actuators of the ISI: excitation in X also drives RX, resulting in the unpleasant g/ω^2 tilt coupling into the Y degree of freedom. As a consequence, the open loop transfer function of the X degree of freedom is altered when control of Y is simultaneously in use according to the equation

$$H_{\mathrm{mod}} = H + \frac{\beta_x \beta_y G^2}{1 - H}. \tag{5.6}$$

Here, $H = H_x = H_y$ is the open loop transfer function when stabilisation of only one degree of freedom is active. The additional factor is proportional to the cross-coupling of the X degree of freedom to Y, β_x, and to the similar coefficient from Y to X, β_y. The effect of the cross-couplings is shown in Fig. 5.3b. The additional factor increases the magnitude of the open loop transfer function and makes the closed loop behaviour unstable. We used the parameters $\beta_y = -\beta_x = 10^{-2}$ in the simulation.

We found that we could reduce the actuation cross-coupling coefficients β_x and β_y shown in Fig. 5.3a down to 0.3% by gain matching the piezo actuators. However, the hysteresis of the actuators causes time-dependent changes to the gains of the piezos over time, therefore we can not reduce this actuation cross-coupling to below 1.5% consistently. As a result, we have reduced the control bandwidth in the X and Y degrees of freedom to avoid the instabilities caused by the actuation cross-couplings.

5.5 Performance

Performance of the platform was inhibited due to the control problems discussed in Sec. 5.4.2. However despite these issues, high gain stabilisation of all six degrees of freedom was achieved once correct implementation of the feedforward scheme between

X, RY and Y, RX was performed. For the 5 softer degrees of freedom this resulted in an order of magnitude or higher suppression at 1 Hz shown in Fig. 5.4.

Vertical suppression was limited due to the stiff resonant frequency, reducing the bandwidth over which stabilisation occurred. Below 1 Hz the actuation in Z was negligible due to non-inertial sensing which would result in sensor noise injection. Reduction of the resonant frequency can be achieved by suspending the system from a soft blade spring to reduce the bounce mode, or by increasing the tension on the fibre. The Glasgow group are currently developing higher stress fibres for use in third generation detectors [117].

The majority of the sensed low frequency motion came from the translational modes, X and Y, and were dominated by the microseismic motion between ~ 0.2 Hz and the 0.62 Hz resonant peaks. The large motion leaked into the other degrees of freedom and can be seen by the red reference traces (no stabilisation) in Fig. 5.4. Implementation of the feedforward scheme described in Sec. 5.4.2 suppressed the coupling into the tilt modes by an order of magnitude in this frequency band (Fig. 5.2). This was imperative in enabling the stable control of the six degrees of freedom.

Further complications arising from the ISI actuation cross-couplings resulted in bandwidth reduction of the X and Y degrees of freedom. The non-linearities of the actuators also caused excess low frequency noise. Comparison between the reference traces (red) and the error signals (blue) show upto an order of magnitude increase in the low frequency below 0.1 Hz.

Improvements on the overall suppression can be achieved by utilising the full actuation range of the piezos, currently we are driving at half range from 0-500 V, however acquisition of 0-1 kV drivers would improve our actuation range by a factor of 2 and potentially reduce non-linearities.

The actuation issues discussed are a reflection of the ISI platform rather than the 6D seismometer itself.

Low frequency drift motion of the mass in the angular degrees of freedom occur due to stress relaxations in the fibre [104] and test mass. The first mechanism effects the RZ drift motion which over time stabilises as shown in Fig. 5.5b. After the large induced drift motion due to pressure changes when venting and pumping the chamber, the DC position of the mass appears to return to its nominal position at an increasing rate each time as the creep events in the fibre reduce over time.

Drift in the tilt modes are predicted to arise due to stress relaxations in the test mass. This causes the centre of mass position to alter over time effecting the angular DC position. A secondary cause of tilt drift is temperature gradients across the test mass which are discussed in [93]. However we determine that the timescale of these drifts is much shorter than the observed drifts due to the temperature stability of the environment.

The drift rate from torsion balance experiments [105, 106, 107, 108] indicates the drift rate scales as $1/f_0^2$ where f_0 is the resonant frequency. Further investigation is planned with reduced the tilt eigenmodes. Preliminary data shown in Fig. 5.5a found that where the drift rate of low frequency RY eigenmode increased drastically. The tilt eigenmodes were reduced by increasing the centre of mass position as described in Eq. 5.1. Due to the asymmetry of the fibre neck where bending occurs, further splitting of the tilt modes was observed causing the RY mode to decrease more than RX.

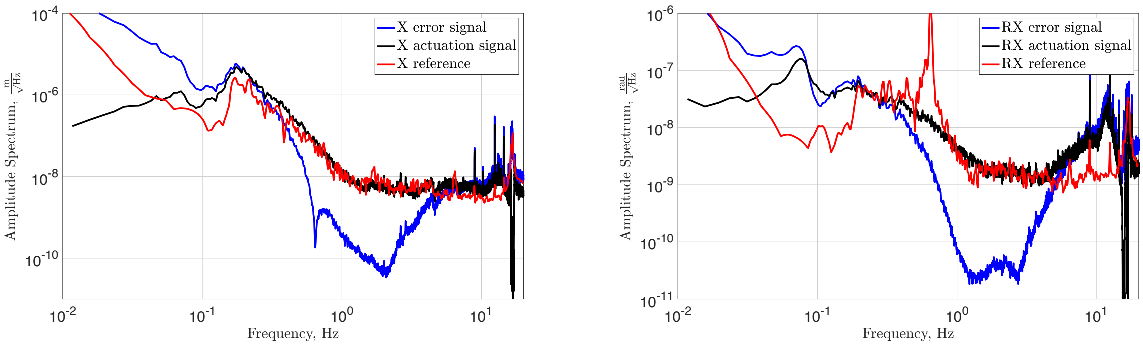

(A) X degree of freedom.

(B) RX degree of freedom.

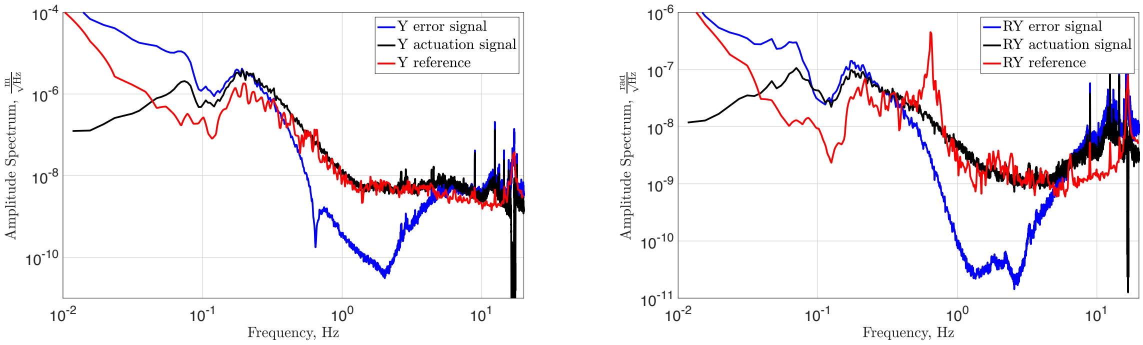

(C) Y degree of freedom.

(D) RY degree of freedom.

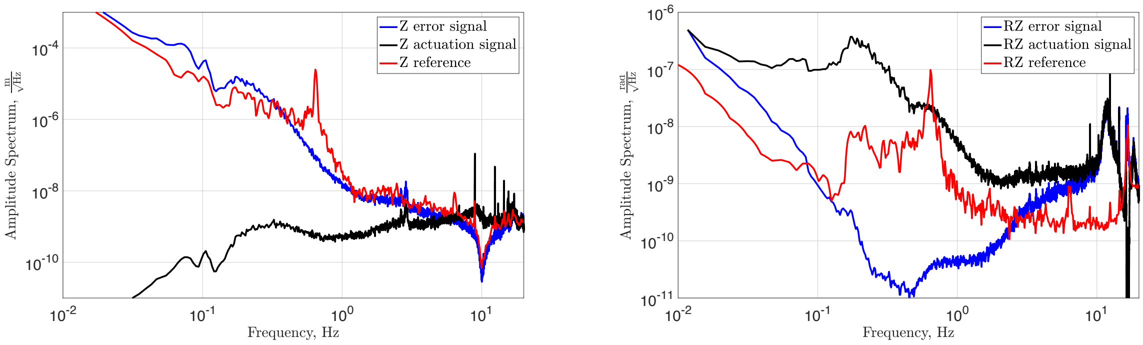

(E) Z degree of freedom.

(F) RZ degree of freedom.

FIGURE 5.4: Performance of the platform stabilisation using the 6D seismometer for simultaneous control of all six degrees of freedom.

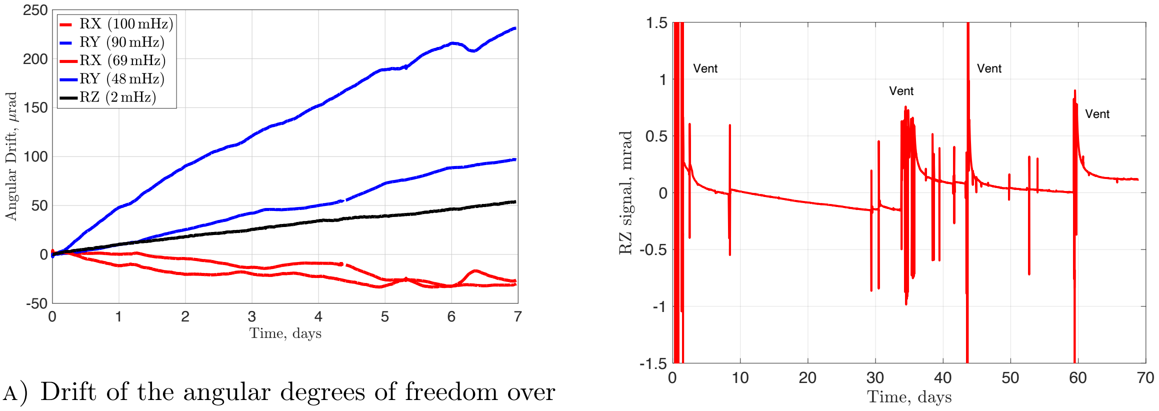

(A) Drift of the angular degrees of freedom over the period of 1 week. The lower eigenmode for RY increased the drift rate due to the increased susceptibility to input noise.

(B)

FIGURE 5.5: Long term drift of the RZ degree of freedom. The stress relaxations in the fibre tend to stabilise after chamber venting and pump down leading to the mass returning to its nominal position.

5.6 Conclusions

We have demonstrated the viability of stabilising a six axis platform using a novel 6D seismometer. The system was operated in high gain with a maximised bandwidth, providing simultaneous control of all six degrees of freedom. We were able to achieve isolation of more than an order of magnitude at 1 Hz for 5 of 6 degrees of freedom.

There are three take home points for the current set up. First is an issue with the sensing. BOSEM noise is higher than expected, however these sensors were used preliminarily while interferometric sensors are prepared for in vacuum use. Interferometric sensors are advantageous due to increased range and lower noise and will be installed in due course.

Secondly the system is susceptible to drift motion for the angular degrees of freedom. There are two possibilities which cause this drift motion. The first is stress relaxations in the fibre, which can not be mitigated. Over timescales much longer than the resonant period we meausure a reduction in the drift rate from this source, and appear to find that the RZ DC position appears to remain constant. A secondary potential source is stress relaxations in the metallic components of the mass, which over time change the balance of centre of mass, resulting in tilt drifts. Changing to a fused silica test mass such as the one suggested in [93] would likely reduce the RMS drift due to the monolithic structure.

Finally, the piezo actuation of the platform limits the stabilisation of the platform to lower frequencies. An important point to note is that the issues with the piezo actuation is a reflection of the test bed used to investigate the 6D seismometer. The actuation drawbacks limit stabilisation to lower frequencies and injects further low frequency noise due to the non-linearities.

Overall, the feasibility of the 6D seismometer has been demonstrated for use in feedback. Control techniques such as feedforward are a necessity in order to recover the degrees of freedom due to the mechanical cross couplings of the simplistic mechanical design and the readout. Further investigations are underway with reduced tilt eigenmodes and short term implementation of interferometric sensing. Increased platform actuation range is also possible with the acquisition of 1 kV piezo drivers which would potentially widen the bandwidth of actuation and increase the open loop gains of the control loops.

Chapter 6

Cryogenic BOSEMs

Chapter 6 is a mature draft of the paper titled "Cryogenic optical shadow sensors for future gravitational wave detectors" submitted to LIGO for review. The author list is as follows: Amit Singh Ubhi, John Bryant, David Hoyland, and Denis Martynov. Experimental work, data collection, and analysis were conducted by myself. I was the principle author for this paper.

6.1 Abstract

Displacement sensors have a variety of applications within gravitational wave detectors. The seismic isolation chain of the LIGO core optics utilises optical shadow sensors for their stabilisation. Future upgrades, such as LIGO Voyager, plan to operate at cryogenic temperatures to reduce their thermal noise and will require cryogenic displacement sensors. We present the results of simulations and experimental tests of the shadow sensors embedded in the Birmingham Optical Sensors and Electromagnetic Motors (BOSEMs). We determine that the devices can reliably operate at 100 K. We also show that the performance of the BOSEM sensors improves at cryogenic temperatures.

6.2 Introduction

Terrestrial gravitational wave detectors such as Advanced LIGO [41] have detected a number of gravitational wave sources since 2015 [12, 14, 15], varying from compact binary sources such as binary black hole mergers [95, 96, 19], binary neutron star inspirals [17], and potential black hole neutron star mergers [97]. Within their most sensitive band, the aLIGO detectors are limited by quantum shot noise and thermal noises of the main optics [101, 36]. To combat the thermal noise, the KAGRA [118, 119] detector cools its core optics. Future upgrades and detectors such as LIGO Voyager [46], the Einstein Telescope [40], and Cosmic Explorer [120, 37] also plan to operate at cryogenic temperatures to reduce their thermal noise [51, 52]. In the case of LIGO Voyager, the core optics will have a silicon substrate. The material exhibits good mechanical properties at cryogenic temperatures and also has a zero thermal expansion coefficient at 123 K [46].

Similar to the current gravitational wave detectors, future observatories will require a comparable or even more sophisticated seismic isolation system [66, 121, 71]. The design of the isolation systems is different in LIGO, Virgo, and KAGRA. However, the detectors share the same isolation principle: suspend the test masses using a multi-stage pendulum suspension to passively filter ground vibrations above the suspension resonances. The resonances are damped using Optical Sensors and Electromagnetic Motors (OSEMs) [110, 122]. The same devices monitor the position of the suspension chain and provide actuation on its stages.

In this paper, we study the Birmingham design of OSEMs (BOSEMs) at cryogenic temperatures to verify their suitability for the cryogenic detectors. The devices as well as another design known as Advanced LIGO OSEMs currently sense and actuate on the LIGO suspensions. BOSEMs are perfect candidates for the next generation observatories because the devices have proven their reliability, large linear range, and ultra high vacuum compatibility. The key question that we address in the paper is whether BOSEMs can operate at cryogenic temperatures. In this paper, we find that the answer to the question is positive. However, the behaviour of optical sensors at cryogenic temperatures is slightly different from their operation at room temperature. We study the discrepancies between the emission of the LED, the photodetector current, and the inherent noise of the device at various temperatures. We also investigate the quantum efficiency of BOSEM LEDs. The efficiency improves at cryogenic temperatures and reduces the overall noise of the sensors. We discuss the potential concerns of cooling down these devices, analyse their sensitivity and propose changes to the electronic design to optimise them for cryogenic usage.

6.3 Finite-element analysis

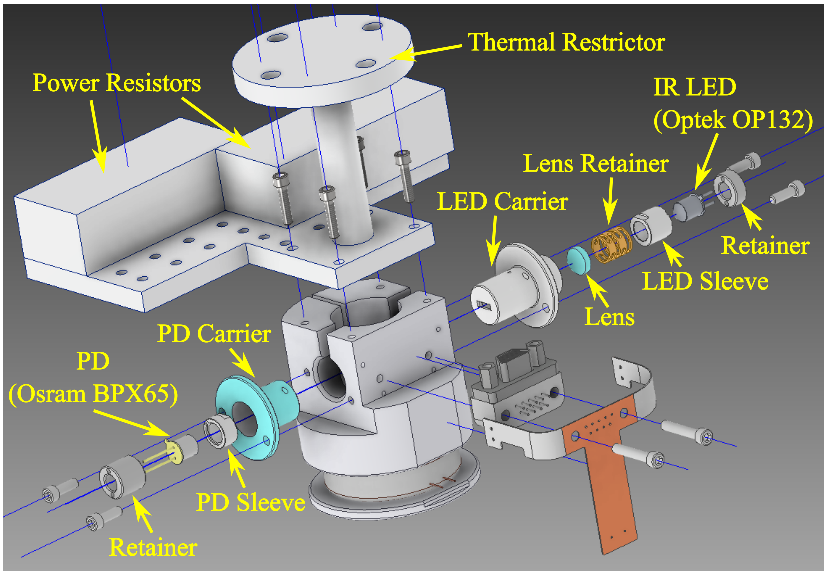
Thermal Restrictor
Power Resistors
IR LED
(Optek OP132)
Lens Retainer
LED Carrier
Retainer
LED Sleeve
Lens
PD Carrier
PD
(Osram BPX65)
PD Sleeve
Retainer

FIGURE 6.1: Exploded view of the BOSEM setup.

Initially, we simulated the cool down procedure of our experimental setup. The setup consists of two main parts: a thermal restrictor and a BOSEM. The restrictor was machined from aluminium and connects the BOSEM to a liquid nitrogen reservoir. The restrictor design was optimised for temperature tuning of the BOSEM with two power resistors located on the restrictor plate as shown in Fig 6.1. The figure also shows an exploded view of the BOSEM. The shadow sensing is achieved by an LED and a photodetector (PD): a measured target blocks part of the LED light to change the PD signal [116]. Both the LED and PD are embedded in the separate assemblies consisting of cylindrical parts for stability and electrical insulation.

The photodetector and LED assemblies are the main concerns during the cool down process because the elements are manufactured from materials with different indices of thermal expansion. Therefore, temperature gradients during the cool down process and uneven contraction of the assembly elements can cause stresses in the device. In particular, the LED and photodetector sleeves are made of MACOR for their electrical insulation while their carriers are made of aluminium to simplify the production process. During cool down, the aluminium carriers would contract more than MACOR, applying a compressive load on the sleeves which may potentially lead to fractures or failure of the component. However, the tolerances of the components allow for the slight excess movement of the sleeve within the carrier. The carrier's inner diameter is, $d_{\text{carrier}} = 0.287^{+0.0006}_{-0.0000}$ in, with the sleeve having outer diameter, $d_{\text{sleeve}} = 0.285^{+0.0000}_{-0.0014}$ in. Assuming a constant coefficient of linear expansion over the temperature range during cooling, the inner diameter of the carrier is always larger than the the maximum diameter of the sleeve which should result in no compressive stress.

We conducted the analyses of the cool down process with the Autodesk Inventor Nastran add-on [123]. We achieved a transient heat transfer model with the constraint that the top of the thermal restrictor is held at 77 K. For the simulation and cool down of the device, two power resistors were used for temperature control. During the simulation they were set with a constant output of 0.2 W of power. The result of the simulation was a temperature map, shown in Fig. 6.2. We then utilised the results of the heat transfer simulation to calculate the stress on the system due to the temperature gradients. Fig. 6.3 is a cross sectional cut of the BOSEM, the highlighted section shows the stress on the MACOR sleeve within the LED carrier. We found that a significant stress comparable to the breaking stress occurs at the interface between the lens retainer and MACOR sleeve. However, the natural length of the lens retainer should reduce when cooled, therefore reducing the axial compressive stress applied against the sleeve. The maximum indicated stress shown in Fig. 6.3 occurs between a screw and the body of the BOSEM. Simulation results confirmed the areas of concern during cooling, and experimental tests were needed to verify the performance of the device at cryogenic temperatures.

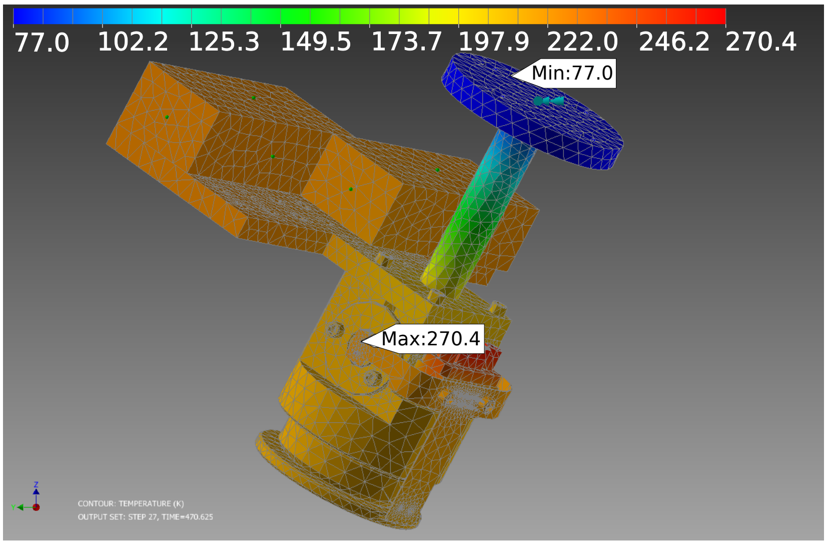

FIGURE 6.2: Temperature (K) map of the BOSEM during the cool down simulation. This time step was chosen as it corresponded to maximum stresses in the BOSEM due to temperature variations.

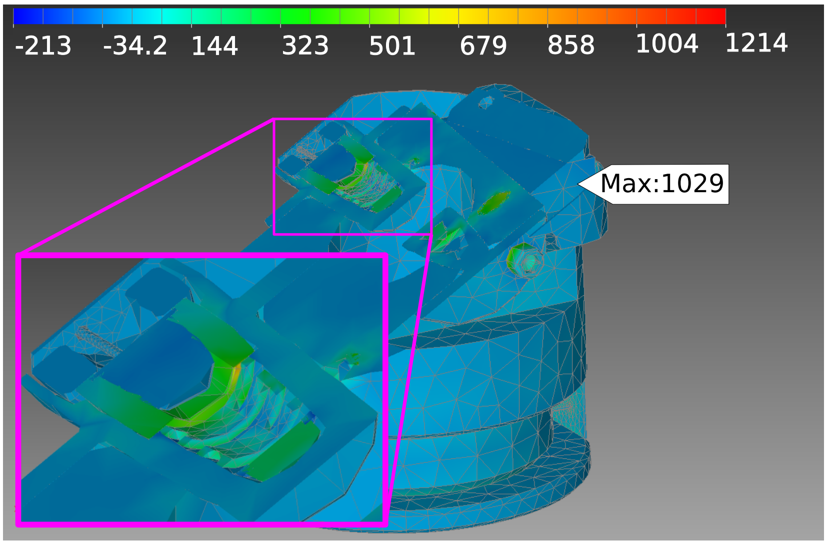

FIGURE 6.3: Stress (MPa) map from temperature map in Fig. 6.2. The highlighted and zoomed section in magenta focuses on a cross section of the LED carrier and its components.

6.4 Experimental results

The shadow sensors have a linear range of $d = 0.7\,\mathrm{mm}$ [116]. The measured displacement corresponds to the changes of the current from the photodetector. This current is then converted to voltage via a satellite amplifier [116] as shown in Fig. 6.4. The observed voltage is then converted to the displacement using the equation

$$K = \frac{V_{\mathrm{max}}}{d}, \tag{6.1}$$

where V_{max} is the maximum voltage on the output of the satellite amplifier. Typical values of the calibration coefficient K are 20-25 kV/m dependent on the parameters of LEDs and photodetectors. In our setup, we measured $K = 20.371\,\mathrm{kV/m}$.

The amplifiers signal is usually fed to the LIGOs control and design system for data processing and requires extra whitening of the signal to overcome the noise of the analog-to-digital converters. In our case, the signal was amplified with an SR560 and then measured with an AC-coupled Agilent 35670a dynamic signal analyzer with low self-noise. In this paper, we tested the shadow sensors without a measured target. Instead, the measurements were taken with the LED either switched on or off, resulting in maximal or zero light from the LED incident on the PD. A baseline measurement was taken in vacuum at 2×10^{-4} mbar to reduce the thermal conductivity between the BOSEM with the environment.

Above 10 Hz, the shadow sensors are limited by their photocurrent shot noise spectrum,

$$\sigma_{\text{shot}}^2 = 2eI_{\text{DC}}. \tag{6.2}$$

where σ_{shot}^2 is the flat white power spectral density of the current, e is the charge of an electron, and I_{DC} is the DC current [124]. We found the shot noise sensitivity to be $6 \times 10^{-11}\text{m}/\sqrt{\text{Hz}}$ above 5 Hz as shown in Fig. 6.7. We note that the value of the shot noise depends on the position on the measured target in the shadow sensor because the I_{DC} changes proportional to the target motion while calibration coefficient K stays the same.

We thermocycled the BOSEM more than 20 times to verify their reliability during and after the cool down process. A number of thermocouples were attached to various parts of the BOSEM to monitor its temperature as shown in Fig. 6.5. During testing the PD temperature was used in feedback, and was stabilised to a temperature of 117.7 K. A temperature below 123 K was used to ensure that any discrepancy in the thermocouple reading at low temperature was accounted for, and that the BOSEM was cycled past its intended operating temperature which could be the case in future operation.

The response of the device is highly sensitive to temperature, during cool down the

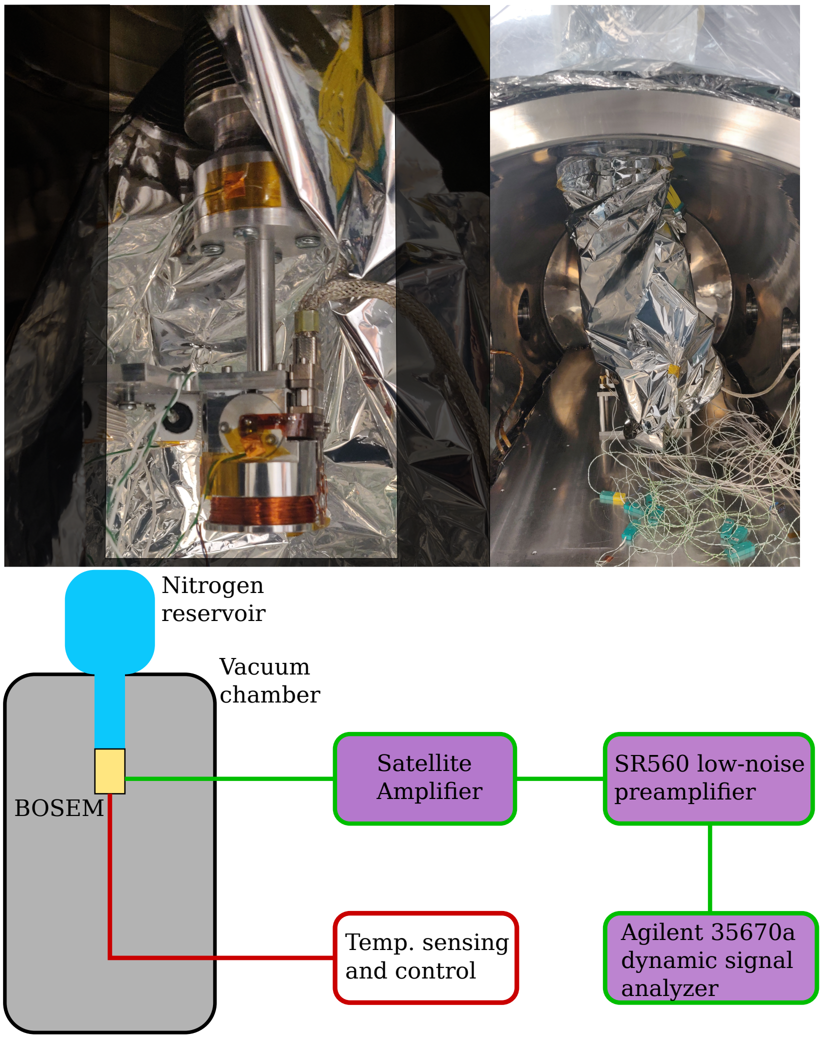
Nitrogen reservoir
Vacuum chamber
BOSEM
Satellite Amplifier
SR560 low-noise preamplifier
Temp. sensing and control
Agilent 35670a dynamic signal analyzer

FIGURE 6.4: **Top left**: Photo of the BOSEM attached inside the vacuum chamber. Above the BOSEM is the thermal restrictor with power resistors connected. Thermocouples are attached to measure its temperature. **Top right**: Image of the BOSEM setup inside the chamber. The set up is encased in mylar to reduce radiative heating from the tank. **Bottom** The Schematic of the experimental set up. The BOSEM satellite amplifier output was converted to a single ended signal, AC coupled at 30 mHz, and high passed at 1 kHz using an SR560 low-noise preamplifier [9]- its output was measured using the Agilent 35670a dynamic signal analyser [10]. Multiple thermocouples were used to measure the BOSEM's temperature, and power resistors were used for temperature stabilisation.

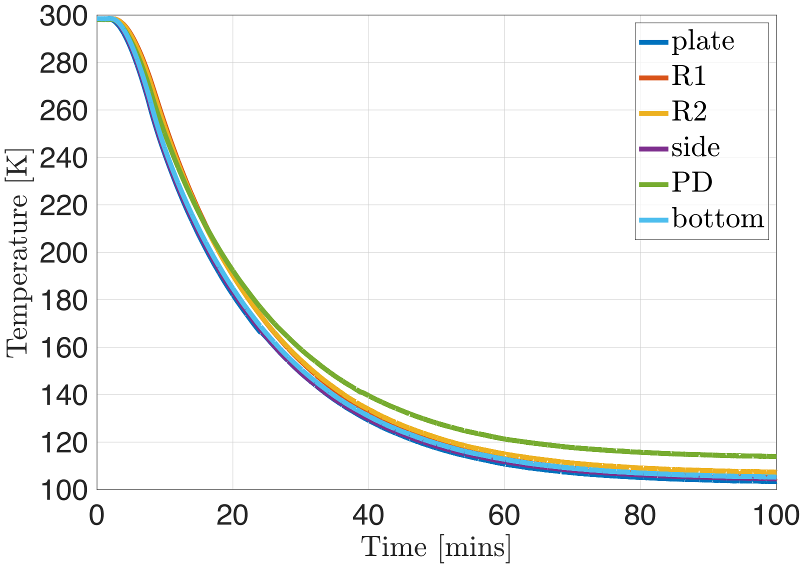

Figure 6.5: Temperatures of BOSEM during cool down. the blue curve represents the thermal restrictor plate, and red and yellow were the power resistors. Purple was the side of the BOSEM housing. The PD outer casing is green, and the bottom of the BOSEM is in cyan. The inital cool down during the first 20 minutes sees the BOSEM change in temperature by over 100° C.

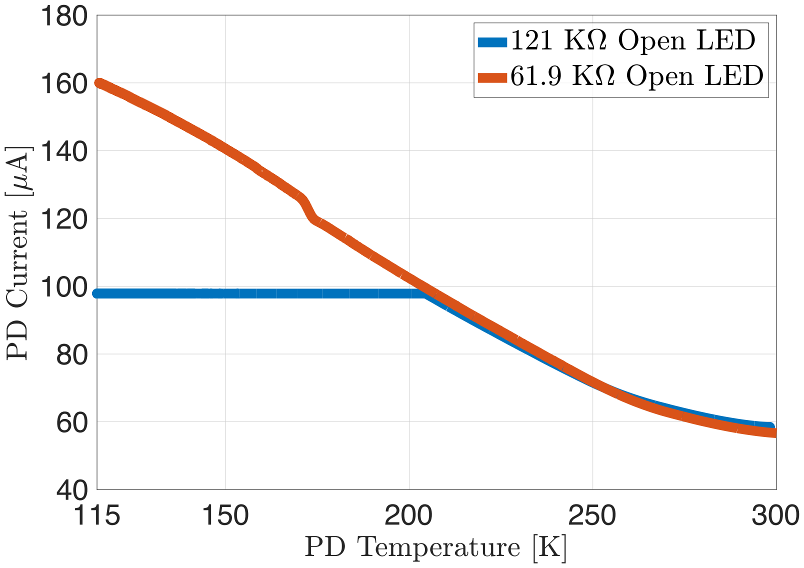

Figure 6.6: Comparison of the PD current during cool down. The 61.9 kΩ transimpedance amplifier did not cause saturation of the satellite amplifier output unlike the 121 kΩ transimpedance amplifier which saturated below 205 K.

PD current increases as shown in Fig. 6.6. A typical satellite amplifier box contains a 121 kΩ transimpedance amplifier, resulting in the output saturating for a 100 μA PD current input. Projection of the PD current enabled us to predict the correct amplifier gain to use such that the satellite box output does saturate. The transimpedance was reduced to 61.9 kΩ while the calibration factor K increased to 27.635 kV/m at 117.7 K. Noise improvements from cooling occur due to the improved quantum efficiency of the LED and photodetector, which results in a stronger signal. Overall, the shot noise of the device improves at cryogenic temperatures as shown in Fig. 6.7.

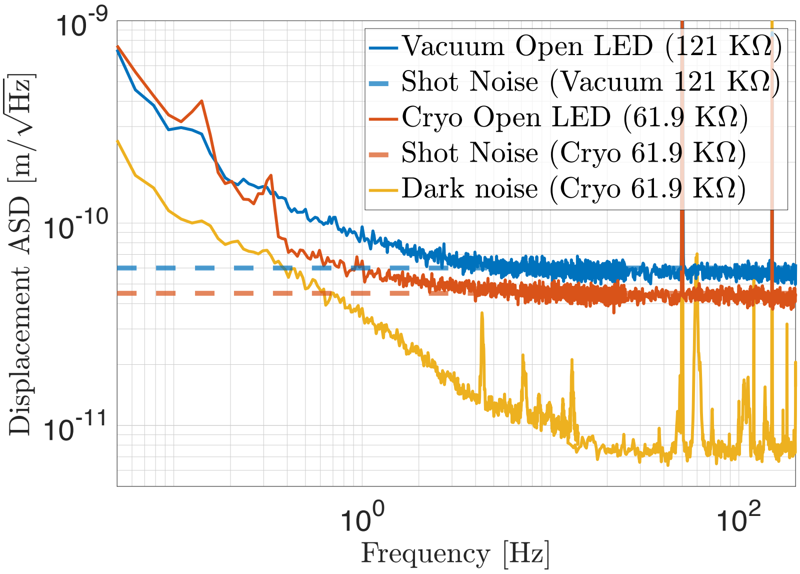

FIGURE 6.7: Comparisons of the measurements made in vacuum and below 123 K. The high frequency shot noise improvements come from the increased PD current. The measurements contain low frequency peaks which occur due to the temperature stabilisation controller. The 61.9 kΩ transimpenance at room temperature coincided with the blue curve at room temperature.

The total efficiency of the optical system is defined according to the equation

$$\eta_{\text{tot}} = \eta_{\text{LED}}\eta_{\text{loss}}\eta_{\text{PD}} = \frac{I_{\text{PD}}}{I_{\text{LED}}}, \tag{6.3}$$

where η_{LED} and η_{PD} are the quantum efficiencies of the LED and photodetector and η_{loss} is the amount of optical power lost between the LED and PD. At room temperature, $\eta_{\mathrm{LED}} \approx 0.058$ and $\eta_{\mathrm{PD}} \approx 0.74$ according to their specifications and $\eta_{\mathrm{tot}} = 60\,\mu\mathrm{A}/35\,\mathrm{mA} = 1.7 \times 10^{-3}$. Therefore, we find $\eta_{\mathrm{loss}} \approx 0.04$. The loss is intentionally introduced by the slit inside the LED carrier (see Fig. 6.1) to collimate the beam.

At 117 K, we measure $\eta_{\mathrm{tot}} = 160\,\mu\mathrm{A}/35\,\mathrm{mA} = 4.6 \times 10^{-3}$. Since our finite element modelling shows no significant deformation of the optical system at cryogenic temperatures as discussed in Sec. 6.3, we expect that the optical loss η_{loss} is temperature independent. Therefore, the improvement in η_{tot} comes from photodetector and LED efficiencies. However, since η_{PD} is already 0.75 at room temperature and the LED central wavelength does not significantly change during the cool down (the spectral shift is 0.3 nm/K), we conclude that the photodetector cannot be responsible for the increase of η_{tot} by the observed factor of 2.7.

The LED efficiency can be written as the product of the internal quantum efficiency of gallium arsenide $\eta_{\mathrm{in}} \approx 0.9$ and the external escape efficiency η_{ex}. The escape efficiency is related to the angle of total internal reflection θ between the LED active layer and vacuum [125]. We note that the formalism in [125] neglects the reflection of light on the interface between the LED substrate and its active layer. Therefore, this can be only used as a guidance to understand the cryogenic performance of our LED. As reported in [126], the index of refraction of gallium arsenide reduces at cryogenic temperatures with $dn/dT \approx 10^{-4}\,K^{-1}$ at room temperature. Therefore, we expect that η_{ex} improves due to the increase of the angle of total internal incidences inside the LED.

6.5 Conclusion

We have demonstrated reliable cryogenic operation of the BOSEMs. The devices have already enabled the control and stabilisation of the LIGO suspensions at room temperature and now have the potential to continue their operation in future gravitational wave detectors. In this paper we have simulated and measured BOSEMs at temperatures below 123 K. We found that the currently used satellite amplifiers saturate below 205 K (Fig. 6.6) due to the enhancement of the LED quantum efficiency at cryogenic temperatures. We have reduced the transimpedance from 121 kΩ down to 61.9 kΩ to avoid the saturation at cryogenic temperatures.

Maximising the output of the satellite amplifier also improves the shot noise limited sensitivity of the shadow sensors. We achieved the shot noise level of $4.5 \times 10^{-11}\mathrm{m}/\sqrt{\mathrm{Hz}}$ with a fully open photodetector compared to the room temperature sensitivity of $6 \times 10^{-11}\mathrm{m}/\sqrt{\mathrm{Hz}}$ in the same optical configuration. The improvement came from increased LED quantum efficiency from 0.045 at room temperature up to 0.12 at 117 K. The spectrum below 5 Hz was limited by the LED current drive and temperature stabilisation feedback loop which caused peaks in the spectrum (Fig. 6.7).

We also found that the first derivative of the LED current over temperature is significantly larger below 200 K compared to the 300 K case. Therefore, temperature fluctuations of BOSEMs should be suppressed in the future gravitational wave detectors for the best sensing noise of the shadow sensors. The cryogenic system of future gravitational wave detectors should also take into account heating from BOSEM LEDs. Even though the quantum efficiency of the LED improves at cryogenic temperatures, approximately 88% of power is still radiated as heat around 100 K. We estimate that each shadow sensor dissipates 61 mW with a current drive of 35 mA.

Chapter 7

Conclusions and Prospects

Chapter 7 draws conclusions to the works discussed in this thesis. No further original work is presented.

7.1 Conclusions

Within the thesis we have introduced the basic understanding of GW production and the primary and potential sources of these waves. We have discussed the principle behind the detection method used for ground based observatories and highlighted the key noise sources plaguing detectors.

The focus of this thesis is improvement to the seismic isolation strategies focusing on the LIGO sites. A description of LIGO's BSC-ISIs control scheme is covered, explaining the ideas behind inertial sensing of the suspension platforms. Low noise sensing is required for stabilisation of the platform to reduce the input motion of the suspension chains. An introduction into control theory is provided with worked explanations of control ideas such as feedback, feedforward, and sensor blending, and stability.

We continue by describing a key area for improvement for the isolation schemes of the ISI platforms. Rotation of the platform affects the controllability of the longitudinal degrees of freedom due to tilt-to-horizontal coupling, directly affecting the GW channel at low frequencies. In vacuum rotation sensors to reduce platform tilt are investigated by a number of groups, and here we present our solution using a novel 6D seismometer. An description of the device and derivations of its dynamics are presented showing the inherent noise of the device which is limited by its local damping controls below 0.1 Hz.

A compact metallic prototype was designed to test the use if interferometric readout and the decoupling scheme - this proved to be a successful endeavour. The lessons learned from the metallic design prompted a new iteration to the design, varying from the original 6D seismometer. A smaller design made of fused silica has been produced by Heraeus [103], resulting in a monolithic structure which should be less susceptible to stress induced drifts.

Using the lessons learned from the compact design, construction and tests of the original 6D seismometer were investigated using less suspended mass. We demonstrated the feasibility of using a six degree of freedom highly coupled device to stabilise a rigid six axis platform. System identification was paramount in decoupling the degrees of freedom, where a feedforward scheme was necessary in providing simultaneous isolation of all degrees of freedom. A key concern was also highlighted which was the long term drift of the metallic proof mass. Further investigations into the causes and mitigations of the drifts are key when moving to lower frequency tilt modes.

Finally, a separate study into auxiliary sensors used in the LIGO suspension chains was explored. The current suspensions use optical shadow sensors to measure residual motion of the optics, future upgrades such as LIGO Voyager would require a similar scheme, however, the end masses would operate at cryogenic temperatures to reduce thermal noise. Simulations and tests of the these shadow sensors were conducted at cryogenic temperatures to test their viability for use on the cold suspensions. We determined that minor changes to the electronics would not only enable their operation at cryogenic temperatures but also potentially improve their sensitivity.

Bibliography

[1] The LIGO Collaboration. Gwinc.

[2] F Matichard et al. Seismic isolation of advanced LIGO: Review of strategy, instrumentation and performance. *Classical and Quantum Gravity*, 32(18):185003, aug 2015.

[3] Krishna Venkateswara, Charles Hagedorn, Matthew Turner, Trevor Arp, and Jens Gundlach. A high-precision mechanical absolute-rotation sensor. *The Review of scientific instruments*, 85:015005, 02 2014.

[4] V. Dergachev, R. DeSalvo, M. Asadoor, A. Bhawal, P. Gong, C. Kim, A. Lottarini, Y. Minenkov, C. Murphy, A. O'Toole, F. E. Peña Arellano, A. V. Rodionov, M. Shaner, and E. Sobacchi. A high precision, compact electromechanical ground rotation sensor. *Review of Scientific Instruments*, 85(5):054502, 2014.

[5] K. Venkateswara and Paroscientific. Quartz rotation sensor: Update, 2021.

[6] J. Belfi, N. Beverini, F. Bosi, G. Carelli, A. Di Virgilio, E. Maccioni, A. Ortolan, and F. Stefani. A 1.82 m2 ring laser gyroscope for nano-rotational motion sensing. *Applied Physics B*, 106(2):271–281, 2012.

[7] C. C. Speake and D. B. Newell. The design and application of a novel high-frequency tiltmeter. *Review of Scientific Instruments*, 61(5):1500–1503, 1990.

[8] J. J. McCann, J. Winterflood, L. Ju, and C. Zhao. A multi-orientation low-frequency rotational accelerometer. *Review of Scientific Instruments*, 92(6):064503, 2021.

[9] Stanford Research Systems. Srs sr560 low-noise preamplifier.

[10] Keysight Technologies. 35670a dynamic signal analyzer, Dec 2017.

[11] Albert Einstein. The meaning of relativity, 2014. Description based on print version record.

[12] Benjamin P Abbott, Richard Abbott, TD Abbott, MR Abernathy, Fausto Acernese, Kendall Ackley, Carl Adams, Thomas Adams, Paolo Addesso, RX Adhikari, et al. Observation of gravitational waves from a binary black hole merger. *Physical review letters*, 116(6):061102, 2016.

[13] R. A. Hulse and J. H. Taylor. Discovery of a pulsar in a binary system. 195:L51, 1975.

[14] B. P. Abbott et al. Gwtc-1: A gravitational-wave transient catalog of compact binary mergers observed by ligo and virgo during the first and second observing runs. *Phys. Rev. X*, 9:031040, Sep 2019.

[15] R. Abbott et al. Gwtc-2: Compact binary coalescences observed by ligo and virgo during the first half of the third observing run. *Phys. Rev. X*, 11:021053, Jun 2021.

[16] Alexander H. Nitz, Collin D. Capano, Sumit Kumar, Yi-Fan Wang, Shilpa Kastha, Marlin Schäfer, Rahul Dhurkunde, and Miriam Cabero. 3-OGC: Catalog of gravitational waves from compact-binary mergers. *The Astrophysical Journal*, 922(1):76, nov 2021.

[17] The LIGO Scientific Collaboration and The Virgo Collaboration. Gw170817: Observation of gravitational waves from a binary neutron star inspiral. *Phys. Rev. Lett. 119 161101 (2017)*, October 2017.

[18] B. P. Abbott et al. Multi-messenger observations of a binary neutron star merger. *The Astrophysical Journal*, 848(2):L12, oct 2017.

[19] R. Abbott et al. GW190521: A binary black hole merger with a total mass of 150 m. *Phys. Rev. Lett.*, 125(10):101102, sep 2020.

[20] R. Abbott et al. Observation of gravitational waves from two neutron star–black hole coalescences. *Astrophys. J. Lett.*, 915(1):L5, 2021.

[21] Peter R. Saulson. Fundamentals of interferometric gravitational wave detectors, 1994.

[22] Luc Blanchet. Quadrupole-quadrupole gravitational waves. *Classical and Quantum Gravity*, 15(1):89, 1998.

[23] Ignazio Ciufolini and Francesco Fidecaro. Gravitational waves: Sources and detectors, 1997.

[24] Gerard Auger and Eric Plagnol. An overview of gravitational waves, 2017.

[25] Bernard Schutz. A first course in general relativity, 2009.

[26] Luc Blanchet. Gravitational radiation from post-newtonian sources and inspiralling compact binaries. *Living Reviews in Relativity*, 17(1), feb 2014.

[27] Christian D. Ott, Adam Burrows, Eli Livne, and Rolf Walder. Gravitational waves from axisymmetric, rotating stellar core collapse. 600:834–864, 2004.

[28] Ewald Muller, Markus Rampp, Robert Buras, H.-Thomas Janka, and David H. Shoemaker. Toward gravitational wave signals from realistic core-collapse supernova models. 603:221–230, 2004.

[29] P. Haensel and J. L. Zdunik. Maximum pulsar mass, equation of state and structure of neutron-star cores. 665:012061, 2016.

[30] I. H. Stairs, A. G. Lyne, and S. L. Shemar. Evidence for free precession in a pulsar. 406:484–486, 2000.

[31] Wen-Cong Chen. Ultra-compact binary pulsars as continuous dual-line gravitational wave sources. *Physical Review D 103, 103004 (2021)*, April 2021.

[32] Chiara Caprini and Daniel G. Figueroa. Cosmological backgrounds of gravitational waves. 35:163001, 2018.

[33] Norna A Robertson. Laser interferometric gravitational wave detectors. *Classical and Quantum Gravity*, 17(15):R19–R40, jul 2000.

[34] Jennifer Watchi, Sam Cooper, Binlei Ding, Conor M. Mow-Lowry, and Christophe Collette. Contributed review: A review of compact interferometers. *Review of Scientific Instruments*, 89(12):121501, 2018.

[35] Alan Weinstein. Advanced ligo optical configuration and prototyping effort. 19:1575–1584, 2002.

[36] Aaron Buikema et al. Sensitivity and performance of the advanced ligo detectors in the third observing run. *Phys. Rev. D*, 102(6):062003, 2020.

[37] David Reitze et al. Cosmic explorer: The u.s. contribution to gravitational-wave astronomy beyond ligo. *2019 BAAS 51(7) 035*, July 2019.

[38] David Reitze et al. The us program in ground-based gravitational wave science: Contribution from the ligo laboratory. *2019 BAAS 51(3) 141*, March 2019.

[39] B. Sathyaprakash. Corrigendum: Scientific objectives of einstein telescope. 30:079501, 2013.

[40] Michele Maggiore et al. Science case for the einstein telescope. *Journal of Cosmology and Astroparticle Physics*, 2020(03):050–050, mar 2020.

[41] J Aasi, B P Abbott, R Abbott, T Abbott, M R Abernathy, K Ackley, C Adams, T Adams, P Addesso, and et al. Advanced ligo. *Classical and Quantum Gravity*, 32(7):074001, Mar 2015.

[42] Matthew Pitkin, Stuart Reid, Sheila Rowan, and Jim Hough. Gravitational wave detection by interferometry (ground and space). *Living Reviews in Relativity*, 14(1):1, July 2011.

[43] Carlton M. Caves. Quantum-mechanical radiation-pressure fluctuations in an interferometer. *Phys. Rev. Lett.*, 45:75–79, Jul 1980.

[44] Haixing Miao. *Quantum Theory of Gravitational-Wave Detectors*, pages 13–49. Springer Berlin Heidelberg, Berlin, Heidelberg, 2012.

[45] Carlton M. Caves. Quantum-mechanical noise in an interferometer. *Phys. Rev. D*, 23:1693–1708, Apr 1981.

[46] R X Adhikari et al. A cryogenic silicon interferometer for gravitational-wave detection. *Classical and Quantum Gravity*, 37(16):165003, jul 2020.

[47] T. Akutsu et al. The status of kagra underground cryogenic gravitational wave telescope. *J. Phys. Conf. Ser.*, 1342(1):012014, 2020.

[48] Gabriela Gonzalez. Suspensions thermal noise in the ligo gravitational wave detector. *Class. Quant. Grav.*, 17:4409–4436, 2000.

[49] AV Cumming, AS Bell, L Barsotti, MA Barton, G Cagnoli, D Cook, L Cunningham, M Evans, GD Hammond, GM Harry, et al. Design and development of the advanced ligo monolithic fused silica suspension. *Classical and Quantum Gravity*, 29(3):035003, 2012.

[50] A. V. Cumming, B. Sorazu, E. Daw, G. D. Hammond, J. Hough, R. Jones, I. W. Martin, S. Rowan, K. A. Strain, and D. Williams. Lowest observed surface and weld losses in fused silica fibres for gravitational wave detectors. *Class. Quant. Grav.*, 37(19):195019, 2020.

[51] G. Harry, T.P. Bodiya, and R. DeSalvo. *Optical Coatings and Thermal Noise in Precision Measurement.* Cambridge University Press, 2012.

[52] S. Gras, H. Yu, W. Yam, D. Martynov, and M. Evans. Audio-band coating thermal noise measurement for advanced ligo with a multimode optical resonator. *Phys. Rev. D*, 95:022001, Jan 2017.

[53] Michael P. Ross et al. Towards windproofing ligo: reducing the effect of wind-driven floor tilt by using rotation sensors in active seismic isolation. 37:185018, 2020.

[54] E. J. Daw, J. A. Giaime, D. Lormand, M. Lubinski, and J. Zweizig. Long term study of the seismic environment at ligo. *Class. Quant. Grav.*, 21:2255–2273, 2004.

[55] E. Schwartz et al. Improving the robustness of the advanced ligo detectors to earthquakes. *Class. Quant. Grav.*, 37(23):235007, 2020.

[56] Craig Cahillane and Georgia Mansell. Review of the advanced ligo gravitational wave observatories leading to observing run four. February 2022.

[57] B. N. Shapiro, R. Adhikari, J. Driggers, J. Kissel, B. Lantz, J. Rollins, and K. Youcef-Toumi. Noise and control decoupling of advanced ligo suspensions. *Class. Quant. Grav.*, 32(1):015004, 2015.

[58] Yoshinori Fujii et al. Active damping performance of the KAGRA seismic attenuation system prototype. *Journal of Physics: Conference Series*, 716:012022, may 2016.

[59] D. M. MacLeod, S. Fairhurst, B. Hughey, A. P. Lundgren, L. Pekowsky, J. Rollins, and J. R. Smith. Reducing the effect of seismic noise in ligo searches by targeted veto generation. *Class. Quant. Grav.*, 29:055006, 2012.

[60] T. A. Callister, J. B. Kanner, T. J. Massinger, S. Dhurandhar, and A. J. Weinstein. Observing gravitational waves with a single detector. *Class. Quant. Grav.*, 34(15):155007, 2017.

[61] Geotech. Short-period seismometer model s-13/gs-13.

[62] Fabrice Matichard and Matthew Evans. Review: Tilt-free low-noise seismometry. *Bulletin of the Seismological Society of America*, 105:497–510, 03 2015.

[63] B Lantz, R Schofield, B reilly, D. Clark, and Dan Debra. Review: Requirements for a ground rotation sensor to improve advanced ligo. *Bulletin of The Seismological Society of America - BULL SEISMOL SOC AMER*, 99, 05 2009.

[64] Brian Lantz. Tilt-horizontal coupling for a simple inverted pendulum, 2006.

[65] F. Matichard, M. Evans, R. Mittleman, M. MacInnis, S. Biscans, K. L. Dooley, H. Sohier, A. Lauriero, H. Paris, J. Koch, P. Knothe, A. Carbajo, and C. Dufort. Modeling and experiment of the suspended seismometer concept for attenuating the contribution of tilt motion in horizontal measurements. *Review of Scientific Instruments*, 87(6):065002, 2016.

[66] MV Plissi, CI Torrie, ME Husman, NA Robertson, KA Strain, H Ward, H Lück, and J Hough. Geo 600 triple pendulum suspension system: Seismic isolation and control. *Review of scientific instruments*, 71(6):2539–2545, 2000.

[67] Gregory M Harry and. Advanced LIGO: the next generation of gravitational wave detectors. *Classical and Quantum Gravity*, 27(8):084006, apr 2010.

[68] F. Matichard et al. Advanced ligo two-stage twelve-axis vibration isolation and positioning platform. part 1: Design and production overview. *Precision Engineering*, 40:273–286, 2015.

[69] F. Matichard et al. Advanced ligo two-stage twelve-axis vibration isolation and positioning platform. part 2: Experimental investigation and tests results. *Precision Engineering*, 40:287 – 297, 2015.

[70] R. Kirchhoff, C. M. Mow-Lowry, et al. Local active isolation of the aei-sas for the aei 10 m prototype facility. 37:115004, 2020.

[71] M.G. Beker, M. Blom, J.F.J. van den Brand, H.J. Bulten, E. Hennes, and D.S. Rabeling. Seismic attenuation technology for the advanced virgo gravitational wave detector. *Physics Procedia*, 37:1389 – 1397, 2012. Proceedings of the 2nd International Conference on Technology and Instrumentation in Particle Physics (TIPP 2011).

[72] S. Wen et al. Hydraulic external pre-isolator system for ligo. *Class. Quant. Grav.*, 31(23):235001, 2014.

[73] PASSCAL. Nanometrics trillium 240 broadband sensor. `https://www.passcal.nmt.edu/content/instrumentation/sensors/broadband-sensors/t240-bb-sensor`. (accessed: 14.09.2021).

[74] Sercel. Seismometers: Analog seismic sensors. `https://www.sercel.com/products/Pages/seismometers.aspx`. (accessed: 14.09.2021).

[75] Jonathan J. Carter et al. Particle swarming of sensor correction filters. 37:205009, 2020.

[76] S.A. Frank. *Control Theory Tutorial: Basic Concepts Illustrated by Software Examples*. SpringerBriefs in Applied Sciences and Technology. Springer International Publishing, 2018.

[77] John Bechhoefer. Feedback for physicists: A tutorial essay on control. *Rev. Mod. Phys.*, 77:783–836, Aug 2005.

[78] M Gopal. *CONTROL SYSTEMS*. McGraw-Hill Education (India) Pvt Limited, 2008.

[79] C. M. Mow-Lowry and D. Martynov. A 6d interferometric inertial isolation system. *Classical and Quantum Gravity*, 36(24):245006, December 2019.

[80] C. Collette, F. Nassif, J. Amar, C. Depouhon, and S.-P. Gorza. Prototype of interferometric absolute motion sensor. *Sensors and Actuators, A: Physical*, 224:72–77, 2015.

[81] J. V. van Heijningen, A. Bertolini, and J. F. J. van den Brand. A novel interferometrically read out inertial sensor for future gravitational wave detectors. In *2018 IEEE Sensors Applications Symposium (SAS)*, pages 1–5, 2018.

[82] W Z Korth, A Heptonstall, E D Hall, K Arai, E K Gustafson, and R X Adhikari. Passive, free-space heterodyne laser gyroscope. *Classical and Quantum Gravity*, 33(3):035004, jan 2016.

[83] Denis Martynov, Nicolas Brown, Eber Nolasco-Martinez, and Matthew Evans. Passive optical gyroscope with double homodyne readout. *Opt. Lett.*, 44(7):1584–1587, Apr 2019.

[84] Hang Yu, Denis Martynov, et al. Prospects for detecting gravitational waves at 5 hz with ground-based detectors. *Phys. Rev. Lett.*, 120:141102, Apr 2018.

[85] S J Cooper, C J Collins, A C Green, D Hoyland, C C Speake, A Freise, and C M Mow-Lowry. A compact, large-range interferometer for precision measurement and inertial sensing. *Classical and Quantum Gravity*, 35(9):095007, mar 2018.

[86] Walter Fichter, Peter Gath, Stefano Vitale, and Daniele Bortoluzzi. LISA pathfinder drag-free control and system implications. *Classical and Quantum Gravity*, 22(10):S139–S148, apr 2005.

[87] Morse-T.F. Méndez, Alexis. 24.2.3.1 silicates, 2007.

[88] AZo Materials. Silica - fused silica (silicon dioxide). `https://www.azom.com/properties.aspx?ArticleID=1387`. (accessed: 14.09.2021).

[89] Wolfram Research, Inc. Mathematica, Version 13.0.0. Champaign, IL, 2021.

[90] MATLAB. *(R2021a)*. The MathWorks Inc., Natick, Massachusetts, 2021.

[91] Peter R. Saulson. Thermal noise in mechanical experiments. *Phys. Rev. D*, 42:2437–2445, Oct 1990.

[92] Piezosystem Jena. Svr 500.

[93] Amit Singh Ubhi, Jiri Smetana, Teng Zhang, Sam Cooper, Leo Prokhorov, Leonid Prokhorov, John Bryant, David Hoyland, Haixing Miao, and Denis Martynov. A six degree-of-freedom fused silica seismometer: design and tests of a metal prototype. *Class. Quant. Grav.*, 39(1):015006, 2022.

[94] F. Acernese et al. Advanced virgo: a 2nd generation interferometric gravitational wave detector. *Class. Quantum Grav. 32 (2015) 024001*, August 2014.

[95] The LIGO Scientific Collaboration and the Virgo Collaboration. Gw151226: Observation of gravitational waves from a 22-solar-mass binary black hole coalescence. *Phys. Rev. Lett. 116, 241103 (2016)*, June 2016.

[96] The LIGO Scientific Collaboration and The Virgo Collaboration. Gw170814: A three-detector observation of gravitational waves from a binary black hole coalescence. *Phys. Rev. Lett. 119, 141101 (2017)*, September 2017.

[97] R. Abbott et al. GW190814: Gravitational waves from the coalescence of a 23 solar mass black hole with a 2.6 solar mass compact object. *ApJL 896 L44*, 896(2):L44, jun 2020.

[98] D. V. Martynov et al. Sensitivity of the advanced ligo detectors at the beginning of gravitational wave astronomy. *Phys. Rev. D*, 93(11):112004, Jun 2016.

[99] A Staley, D Martynov, et al. Achieving resonance in the Advanced LIGO gravitational-wave interferometer. *Classical and Quantum Gravity*, 31(24):245010, 2014.

[100] D. Martynov. *Lock Acquisition and Sensitivity Analysis of Advanced LIGO Interferometers.* PhD thesis, Caltech, 2015.

[101] D. V. Martynov et al. Quantum correlation measurements in interferometric gravitational-wave detectors. *Phys. Rev. A*, 95:043831, Apr 2017.

[102] Stephan Theil. Drag-free satellite control. *Lasers, Clocks and Drag-Free Control*, January 2008.

[103] Heraeus. Heraeus. `https://www.heraeus.com/`. (accessed: 14.09.2021).

[104] Yuri Levin. Creep events and creep noise in gravitational-wave interferometers: Basic formalism and stationary limit. *Phys. Rev. D*, 86:122004, Dec 2012.

[105] E. G. Adelberger, C. W. Stubbs, Blayne R. Heckel, Y. Su, H. E. Swanson, G. Smith, J. H. Gundlach, and W. F. Rogers. Testing the equivalence principle in the field of the earth: Particle physics at masses below 1-microev? *Phys. Rev. D*, 42:3267–3292, 1990.

[106] Terry Quinn, Harold Parks, Clive Speake, and Richard Davis. Improved determination of g using two methods. *Phys. Rev. Lett.*, 111:101102, Sep 2013.

[107] Giacomo Ciani, Andrew Chilton, Stephen Apple, Taiwo Olatunde, Michael Aitken, Guido Mueller, and John W. Conklin. A new torsion pendulum for gravitational reference sensor technology development. *Review of Scientific Instruments*, 88:064502, 2017.

[108] Giuliana Russano. A torsion pendulum ground test of the lisa pathfinder free-fall mode. *arXiv e-prints*, page arXiv:1609.00002, August 2016.

[109] Katharina-Sophie Isleif, Gerhard Heinzel, Moritz Mehmet, and Oliver Gerberding. Compact multifringe interferometry with subpicometer precision. *Phys. Rev. Applied*, 12:034025, Sep 2019.

[110] K. A. Strain and B. N. Shapiro. Damping and local control of mirror suspensions for laser interferometric gravitational wave detectors. *Rev. Sci. Instrum.*, 83:044501, 2012.

[111] N. Mavalvala, D. Sigg, and D. Shoemaker. Experimental Test of an Alignment-Sensing Scheme for a Gravitational-Wave Interferometer. *Applied optics*, 37:7743–7746, November 1998.

[112] L Barsotti, M Evans, and P Fritschel. Alignment sensing and control in Advanced LIGO. *Classical and Quantum Gravity*, 27(8):084026, 2010.

[113] Katherine L. Dooley, Lisa Barsotti, Rana X. Adhikari, Matthew Evans, Tobin T. Fricke, Peter Fritschel, Valera Frolov, Keita Kawabe, and Nicolás Smith-Lefebvre. Angular control of optical cavities in a radiation-pressure-dominated regime: the enhanced ligo case. *J. Opt. Soc. Am. A*, 30(12):2618–2626, Dec 2013.

[114] Jiri Smetana, Rebecca Walters, Sophie Bauchinger, Amit Singh Ubhi, Sam Cooper, David Hoyland, Richard Abbott, Christoph Baune, Peter Fritchel, Oliver Gerberding, Semjon Köhnke, Haixing Miao, Sebastian Rode, and Denis Martynov. Compact michelson interferometers with subpicometer sensitivity, 2022.

[115] Binlei Ding, Guoying Zhao, Jennifer Watchi, Ameer Sider, and Christophe Collette. An interferometric inertial sensor for low-frequency seismic isolation. *Sensors and Actuators A: Physical*, 335:113398, 2022.

[116] L. Carbone et al. Sensors and actuators for the advanced ligo mirror suspensions. *Class. Quant. Grav.*, 29:115005, 2012.

[117] A. V. Cumming, R. Jones, G. D. Hammond, J. Hough, I. W. Martin, and S. Rowan. Large-scale monolithic fused-silica mirror suspension for third-generation gravitational-wave detectors. *Phys. Rev. Applied*, 17:024044, Feb 2022.

[118] Kentaro Somiya. Detector configuration of KAGRA–the japanese cryogenic gravitational-wave detector. *Class. Quantum Grav. 29 124007*, 29(12):124007, jun 2012.

[119] Yoichi Aso, Yuta Michimura, Kentaro Somiya, Masaki Ando, Osamu Miyakawa, Takanori Sekiguchi, Daisuke Tatsumi, and Hiroaki Yamamoto. Interferometer design of the kagra gravitational wave detector. *Phys. Rev. D*, 88:043007, Aug 2013.

[120] B. P. Abbott et al. Exploring the sensitivity of next generation gravitational wave detectors. *Classical and Quantum Gravity*, 34(4):044001, February 2017.

[121] The VIRGO Collaboration (presented Braccini). The VIRGO suspensions. *Classical and Quantum Gravity*, 19(7):1623–1629, mar 2002.

[122] Tomotada Akutsu et al. Compact integrated optical sensors and electromagnetic actuators for vibration isolation systems in the gravitational-wave detector KAGRA. *Review of Scientific Instruments*, 91(11):115001, nov 2020.

[123] Autodesk. Autodesk empowers innovators everywhere to make the new possible, Oct 2021.

[124] Steven G. Bramsiepe, David Loomes, Richard P. Middlemiss, Douglas J. Paul, and Giles D. Hammond. A high stability optical shadow sensor with applications for precision accelerometers. *IEEE Sensors Journal*, 18(10):4108–4116, May 2018.

[125] Rongqing Hui. Chapter 3 - light sources for optical communications. In Rongqing Hui, editor, *Introduction to Fiber-Optic Communications*, pages 77–124. Academic Press, 2020.

[126] J. A. McCaulley, V. M. Donnelly, M. Vernon, and I. Taha. Temperature dependence of the near-infrared refractive index of silicon, gallium arsenide, and indium phosphide. *Phys. Rev. B*, 49:7408–7417, Mar 1994.